Doctoral Dissertation

Bonding Mechanism and Corrosion Behavior of Directly Bonded Ti and Mg-Al Alloys Materials

Patchara Pripanapong

January 2017

Graduate School of Engineering

Osaka University

ABSTRACT

The objective of this research is to fabricate a light weight bonding component between pure Ti and Mg alloys without an inserted sheet with high strength and good corrosion resistance. Many researchers studied on bonding between Ti and Al alloys, but with this successful bonding between pure Ti and Mg alloys, the weight of bonded component could be further decreased. Dissimilar metal joining between titanium and magnesium alloys was performed by spark plasma sintering. Metallurgical bonding between pure titanium and magnesium alloys such as AZ31B, AZ61, AZ80 and AZ91 was achieved by diffusion of Al atoms from a magnesium alloy side to a titanium side and formed a Ti_3Al intermetallic layer at the interface. A solution treatment of magnesium alloys before bonding resulted in an increase of Al content in the Mg matrix, which facilitate a formation of continuous Ti_3Al layer and improve bonding strength of bonded materials. Bonding pressure of 10 MPa was sufficient to provide a perfect contact between titanium and magnesium alloys surface. A good bonding strength was obtained when applying bonding time over 0.5 h. The increase of bonding temperature facilitates formation of a Ti_3Al intermetallic layer by increasing the diffusion rate of Al atoms, which results in an improvement of bonding strength. The highest bonding strength of 194 MPa was obtained for Ti/AZ91 (ST) bonded at 475 ºC for 1 h, which represents 96.3% of bonding efficiency. The improvement of corrosion resistance of bonded material is as important as bonding strength since it increases a life span of this light weight dissimilar material joint. For a sample immersed in 5 wt% NaCl solution, a Ti bonded to a solution treated Mg alloy or Mg alloy (ST) shows an improvement of galvanic corrosion resistance according to the disappearance of a $Mg(OH)_2$ layer at the bonding interface when Al content in a Mg alloy increases. The increase in bonding temperature also has an effect on the improvement of galvanic corrosion resistance by facilitating the formation of Ti_3Al that decreases the surface potential difference (SPD) and potential gradient between pure Ti and Mg alloys. The sample immersed in Kroll's etchant exhibits a similar corrosion behavior to sample immersed in 5 wt% NaCl solution. The increase of Al content in a Mg alloy decreases a galvanic depth (G.D.) and galvanic width (G.W.) which appear after a

corrosion test. Ti/AZ91 (ST) bonded material shows the best galvanic corrosion resistance among all dissimilar bonded materials with the lowest G.D. and G.W.

TABLE OF CONTENTS

LIST OF FIGURES

LIST OF TABLES

CHAPTER 1: INTRODUCTION

1.1 Background and objectives

Titanium and titanium alloys are well-known structural materials that possess a high strength to weight ratio (high specific strength), high fracture toughness and excellent corrosion resistance. These materials are widely used in automobile (mostly in racing car) and aerospace industries because of their light weight, which effectively reduce fuel consumption in vehicles and CO_2 pollution gas emitting to the environment [1, 2]. Titanium and its alloys are also used in the medical field such as prosthesis bone or joint because they possess a good biocompatibility [3-5]. The factor that limits an application of titanium and its alloys is its high cost relative to other structural materials such as aluminum, steel and magnesium due to the difficulty in extraction and production process. Magnesium and its alloys are light materials which possess the lowest density (1.74 g/cm^3) among structural materials, and their attraction in research field has gradually increased nowadays. Similar to titanium, magnesium and its alloys possess high specific strength that makes them suitable for use in automobile and aerospace components [6, 7]. The disadvantage of magnesium is its poor corrosion resistance and biocompatibility, which limit its application as biomaterials in human body and as structural components under a harsh environment. Fortunately, some methods such as coating can be applied to magnesium surface to improve these properties, and then it can be used as a biomaterial [8]. Many researchers interested in bonding titanium and aluminum alloys or steel, where such bonded materials exhibited a high tensile and shear strength [9, 10]. The main objective of their works was to reduce the weight of structural component that was generally made of titanium or steel. Bonding titanium to magnesium instead of aluminum is the new effective method to fabricate advanced light dissimilar materials, because magnesium (1.74 g/cm^3) has a much lower density comparing to aluminum (2.70 g/cm^3). Furthermore, the maximum working temperature of Ti/Mg and Ti/Al dissimilar materials is similar according to the close melting temperatures between magnesium and aluminum at 650 and 660 ^{o}C, respectively.

The development of joining between Ti and Mg alloys will improve its potential application in future structures, where light weight is required to reduce fuel consumption, and greenhouse gas emission, as well as to improve an efficiency of energy converting system. However, joining Ti with Mg is a challenge work and difficult, as no intermetallic compound can be formed between Ti and Mg referring to their binary phase diagram. This is different from bonding between Ti and Al, for which many intermetallic compounds such as $TiAl_3$, TiAl and Ti_3Al can be formed at the bonding interface, and contribute to bonding. The significant difference in physical and mechanical properties between Ti and Mg or Mg alloy is also the obstacles to joining these two materials. A great difference in physical property between Ti and Mg such as melting point (T_m of Ti = 1668 ºC, T_m of Mg = 650 ºC) and a low eutectic temperature of Mg alloy may result in melting of Mg alloy before the alloying elements in it react with Ti to form a chemical bond. The differences in mechanical property between them may also result in large residual stress after joining, which may induce failure at the bonding interface during usage as a structural component. Therefore, the joining method has to be carefully selected in order to obtain fine bonding interfaces and high bonding strength in dissimilar materials. The conventional joining methods such as adhesive bonding, brazing, soldering or solid state bonding have been considered to join Ti and Mg alloys. However, adhesive bonding is not suitable to apply in this case, because the bonded components may be used at high temperatures (exceed 150 ºC) and exposed to corrosion substance that may damage the adhesive material. Brazing and soldering require a suitable filler metal to join two or more metal components without melting parent metals. However, the significant difference in physical properties between Ti and Mg or Mg alloys causes a difficulty in joining and obtaining a high bonding strength between these two materials.

Advanced joining methods such as solid state bonding and transient liquid phase bonding (TLP bonding), which have been well reported in many research papers, show a potential in joining dissimilar materials. The solid state bonding usually requires a high temperature and pressure during the bonding process. This process has an advantage in comparison to the other joining methods, owing to the high applied pressure that provides a perfect contact between two bonding parts, and simultaneously destroys the oxide

film existing on the initial surfaces. At the same time, the high temperature contributes to the diffusion of alloying elements, and formation of reaction layer at the bonding interface. Therefore, a high bonding strength joining material can be obtained by this process. On the other hand, TLP bonding requires an inserted metal sheet to be melted at a high temperature during bonding, and then accomplishes bonding by eutectic reaction with the parent metals. The eutectic liquid phase solidified at constant temperature and an intermetallic compound (IMC) layer between the inserted sheet and parent metals is formed. However, the IMC layer that formed by a solidification of liquid phase in TLP process is thick (in the order of several μm), and causes brittleness at the bonding interface, which results in a degradation of the bonding strength. From the mentioning fundamental knowledge, a solid state bonding is considered as a suitable method to bond pure Ti to Mg alloys.

The corrosion resistance is another important property that has to be considered for bonded materials. The bonded materials are usually used in an active environment that may contact with moisture, acidic solution or gas. For the dissimilar materials, the galvanic corrosion might occur due to the difference in surface potentials of parent metals. The material that possesses a lower surface potential will corrode at the contact area when contacting with the material that possesses a higher surface potential. The galvanic corrosion resistance of bonded materials can be improved by the formation of IMCs layer which possesses low surface potential. The improvement of galvanic corrosion resistance can sustain the bonding strength of joining materials during application and increase its life span.

This research aims to study the bonding mechanism between pure Ti and Mg alloys by applying spark plasma sintering (SPS) to fabricate the samples. Bonding parameters are varied in order to improve the bonding strength of bonded materials. The SPS method is usually applied to metal powders for sintering and densification where high density and precise dimension are required. In this research, SPS is adapted for the bonding process because of many advantages. For example, very high temperatures can be imposed to samples simultaneously with an applied pressure. Besides, a high vacuum atmosphere can be achieved in the chamber and higher heating rate compare to conventional hot pressing can be applied to shorten the processing time. Some researchers mentioned that applying a

high pressure during SPS can destroy the original oxide film on the parent metals surfaces, resulting in a good bonding surface condition [11]. The bonding parameters such as temperature, pressure and time are varied so as to investigate the effect of different bonding parameters on the bonding strength of dissimilar materials by a change in characteristic at the bonding interface. The type of Mg alloy also has an effect on the bonding strength because of different content of Al in different Mg alloys, where high Al content facilitates the formation of IMC layer. The bonding temperature is a very important factor that contributes to the diffusion of Al atoms in Mg alloy towards Ti. The high bonding temperature such as 475 ºC results in the formation of a small amount of Mg (Al) liquid phase from Mg alloy side by eutectic reaction between Mg and Al which facilitates the reaction between Ti and Al.

Regarding to bonding process, the solid state bonding method is the most suitable way to bond pure Ti to Mg alloys. In this case, hot pressing and spark plasma sintering are available because both methods have an advantage that the pressure can be introduced to sample during bonding. However, heating rate that can be applied in SPS is higher than hot pressing due to the direct contact between graphite container and electrode which generates the electrical current. According to this reason, the SPS is applied in this research.

The applied bonding pressure during SPS causes plastic deformation at the bonding interface, leading to a perfect contact between pure Ti and Mg alloy surfaces. However, an excessive bonding pressure can damage the graphite container and bonded samples. The bonding time is another considerable factor because it also influences the bonding strength of the bonded material. Fabrication time (or bonding time) is a very important factor for industry production line because high production rate gives high profit. Therefore, a suitable bonding time should be considered. The advantages of SPS method are not only providing a high temperature and pressure simultaneously, but also providing high heating rate where pure Ti and Mg alloys can be successfully joined within one hour. Another objective of this research is to study the corrosion behavior of the bonded materials fabricated by different bonding conditions. The effect of IMC layer on the galvanic corrosion resistance of dissimilar materials, which has been reported in the literature [12], is also studied and clarified. The galvanic

corrosion easily occurs between pure Ti and Mg alloys due to the large difference of their standard electrode potentials (Ti = -1.6 V and Mg = -2.7 V: relative to the standard hydrogen electrode). To evaluate the galvanic corrosion in dissimilar materials, a surface potential difference between pure Ti and Mg alloys is measured at the bonding interface. Moreover, the surface profiles after the corrosion test are investigated. The corrosion resistance of Mg alloys matrices are also evaluated by surface potential measurement and the results are corresponding well to the corroded damage on a matrix after corrosion test. Eventually, bonded materials between pure Ti and Mg alloys with high bonding strength and good galvanic corrosion resistance are successfully fabricated by SPS method.

1.2 Thesis structure

Chapter 2 describes pure Ti and Mg alloys which are the structural materials that are applied in this research. The fundamental knowledge and their applications will be given in this chapter. Various bonding techniques applied to these materials are also discussed and compared in regard to the advantages and disadvantages of each method. The solid state bonding method is described in detail and many examples of various alloys bonding through this method by other researchers are discussed. The effects of bonding parameters on the characteristic of bonding interface, strength and corrosion behavior of the bonded materials are also discussed.

Chapter 3 explains the details of materials used in this research, and also the sample preparation before and after bonding for microstructure observation. The bonding conditions and methods for bonding strength and corrosion resistance evaluation are explained in this chapter. The detail of SPS machine and components arrangement inside SPS chamber for solid state bonding are described. The metallographic analysis is described for the bonding interface via optical microscope (OM), scanning electron microscope (SEM) and transmission electron microscope (TEM). The mechanical evaluation of bonded materials by tensile testing machine is described. The surface potential measurement by scanning kelvin probe force microscope (SKPFM) for studying the corrosion behavior of bonded materials is described. The surface profile analysis after corrosion test are also described in this chapter.

In chapter 4, the microstructure evolution at the bonding interface and bonding strength of Ti/Mg alloys and Ti/Mg alloys (ST) dissimilar materials are shown in detail when Mg alloy (ST) is referring to solution treated Mg alloy. The effects of solution treatment of a Mg alloy on microstructure evolution at the bonding interface and on bonding strength are discussed. Furthermore, the effects of bonding parameters such as bonding temperature, time and pressure on microstructure evolution and bonding strength are also discussed in this chapter.

Chapter 5 describes the corrosion behavior of Ti/Mg alloy (ST) dissimilar materials which are bonded at low and high temperatures. The effect of an IMC layer on galvanic corrosion resistance of dissimilar materials is discussed. Moreover, the surface profile of bonded materials after corrosion test and galvanic parameters are measured and discussed.

Finally, a summary of this work is presented in chapter 6, where the possible future work is also recommended.

CHAPTER 2: LITERATURE REVIEW

2.1 Introduction

Ti alloys and Mg alloys are widely used in many industrial fields because of many advantages in their physical and mechanical properties. In particular, both materials have a significant advantage in weight reduction effect. These materials are mainly used for automobile components (mostly in racing car in which light weight components are required) and aerospace components. Ti and its alloys possess good biocompatibility then they can use for biomedical tools and prosthesis that implanted in human body [13-15]. Fabrication of bonded components between pure Ti and Mg alloys will improve a potential in further applications because of decreasing in weight of the component and also in material cost. However, a development of the bonding process between pure Ti and Mg alloys is a great challenge since these materials possess a large difference in physical and mechanical properties. Furthermore, the Ti-Mg binary phase diagram shows no phase or intermetallic compound between Ti and Mg [16], and then an alloying element in Mg is required in order to obtain a successful bonding between them. This chapter discusses about the properties of Ti and its alloys, Mg and its alloys, and also various bonding methods used for dissimilar materials bonding. The corrosion behavior of Ti and its alloys, Mg and its alloys and bonded materials are also discussed in the last section.

2.2 Titanium and its alloys

2.2.1 Titanium overview

Ti was discovered by William Gregor in 1791 and named by Martin Heinrich Klaproth after the Titans in 1795. Ti is widely distributed in the earth's crust. It can be extracted from its mineral ores through Kroll's process (eq. 2.1) or Hunter's process (eq. 2.2) that were developed by William J Kroll and Matthew A Hunter, respectively [17].

$$TiCl_4 + 4Mg \rightarrow 4MgCl + Ti \quad \text{(eq. 2.1)}$$

$$TiCl_4 + 4Na \rightarrow 4NaCl + Ti \quad \text{(eq. 2.2)}$$

Ti and its alloys possess many advantages such as light weight (55% density of steel) and high specific strength, which make it grow rapidly in industry. From the view point of light weight and high specific strength, Ti is very attractive to use for highly loaded aerospace components that operate at moderately elevated temperatures, including air frame and jet components [18, 19]. Good corrosion resistance of Ti is due to the stable protective oxide film. The passivation behavior of Ti makes it useful in range of applications from chemical processing equipment to prosthesis implanted in human body.

Titanium can be present in two crystallographic forms. At room temperature, an unalloyed Ti has a hexagonal close-packed (hcp) crystal structure refer to as alpha (α) phase (Fig. 2.1a). The α phase Ti change at a temperature of 883 ºC to a beta (ß) phase Ti that has a body-centered cubic (bcc) crystal structure (Fig. 2.1b).

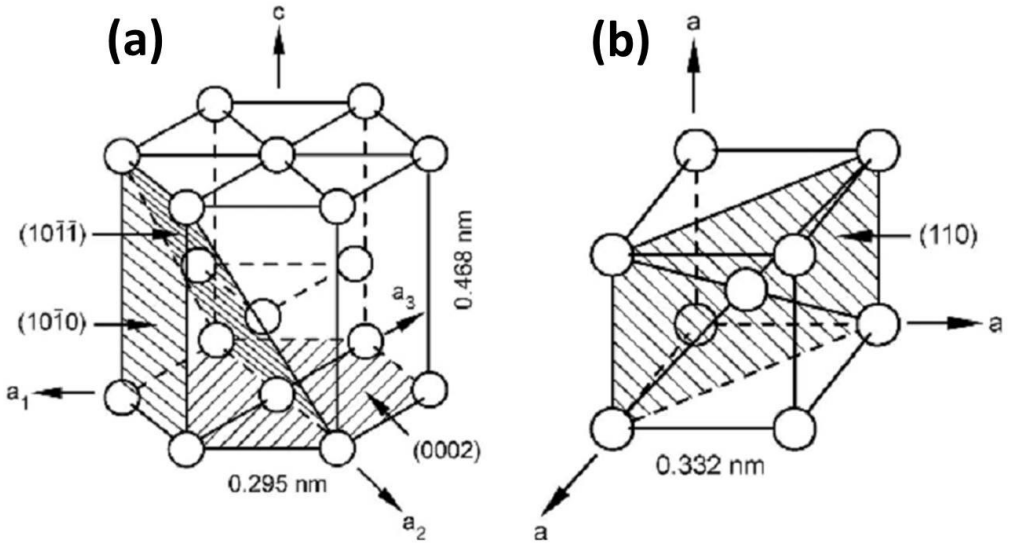

Fig. 2.1 Two types of titanium crystal structures (a) hcp structure and (b) bcc structure.

The crystal structure of Ti or its alloys is controlled by alloying elements and the thermo-mechanical process. Thus, alloys with a wide range of properties can be developed. These phases can be used to categorize

Ti alloys into four types, Alpha alloys, Near-alpha alloys, Alpha+Beta alloys and Beta alloys.

Alpha alloys contain an element such as Al, C, O, N and Sn, which can then be referred as α-stabilizers. These elements work by increasing the phase transformation temperature (α transus) or inhibit a change of the microstructure. Comparing to ß alloys, α alloys have a superior creep resistance and are more suitable to be uses at elevated temperatures. Moreover, the absence of ductile-to-brittle transition of α alloy makes them suitable for cryogenic applications. Alpha alloys are characterized to be satisfactory for strength, toughness and weldability, but with poorer forgeability comparing to ß alloys. Alpha alloys are often used after annealing or recrystallization condition to eliminate residual stress from work, and never strengthened by heat-treatment. The examples of α alloys include Ti-5Al-2Sn-ELI and Ti-8Al-1Mo-1V.

Near-alpha alloys contain 1-2% of ß stabilizers such as Mo, V and Si. The microstructures of these alloys contain a small amount of ß phase. Similar to α alloy, near-alpha alloys have a good creep resistance, toughness and weldability with a moderate mechanical strength. The existence of the small amount of ß phase makes them capable to be heat-treated or forged at high temperatures.

Alpha+Beta alloys have a composition of the alloying elements that maintain α and ß phase mixtures at room temperature, and may contain 10-50% of ß phase in the microstructure. The most well-known α+ß alloy is Ti-6Al-4V, which has been used mostly among Ti alloys because of its high strength comparing to the commercially grade pure Ti that has a comparable stiffness. This alloy was an excellent combination of strength, corrosion resistance and weldability. In particular, a fine mixture of α phase and transformed or retained ß phase can be obtained through solution heat treatment followed by aging at 480-650 ºC.

Beta alloys contain ß stabilization elements such as Mo, Nb, V and Cr that cause a decrease of the ß transus temperature (the temperature there all of α phase transforms to ß phase). These alloys have a good forgeability over a wide range of forging temperatures, and a ß alloy sheet is cold formable in the solution treated condition. Beta alloys have a good hardenability and respond readily to heat-treatment. A general heat-treatment process for these alloys involves solution treatment followed by aging at a temperature

range of 450-650 ºC. This results in a formation of a finely disperse α particle in a retain β phase.

The product life cycle of Titanium has been used to analyze an increase or decrease of demand for various materials, as shown in Fig. 2.2. A typical product life cycle begins with product's introduction into marketplace. Many of product's stages are well-defined in the schematic such as rapid growth, maturity or ultimately decline as replacement product enter marketplace. From the schematic, it concludes that, despite an introduction of new alloys or product forms, titanium is moving rapidly through its product life cycle to maturity in an aircraft industry. The metal is still in a growth stage where corrosion resistance is important. Applications in the automotive industry and architecture are only in a development stage. These applications should be strengthened to stabilize the demand of titanium. This diversification can accelerate as an industry coming to mature and a demand of titanium will move from the technology product to commodity one.

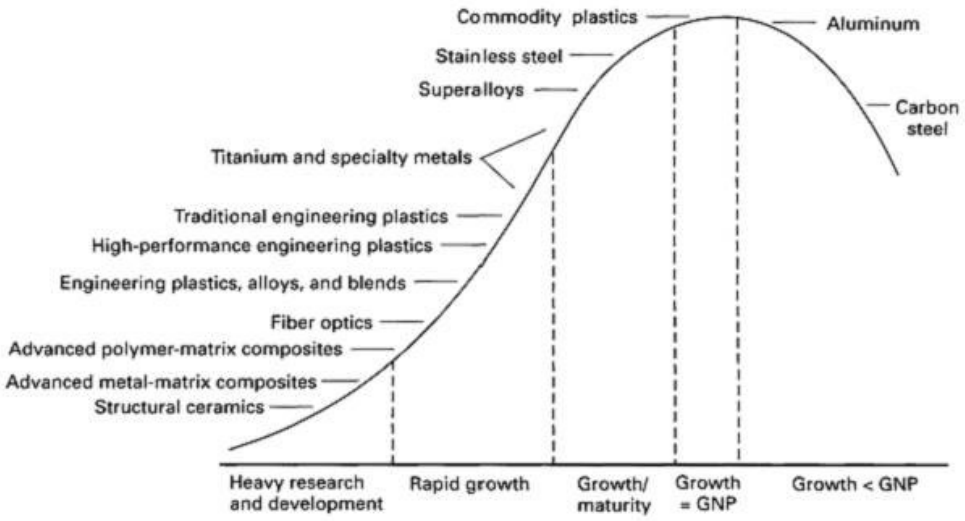

Fig. 2.2 Schematic product life cycle curve of various products and technologies, titanium ranges from rapid growth to growth/maturity stage [20].

2.2.2 Application of Ti and its alloys

Ti and its alloys are very attractive to use in the aerospace industry because of many advantages in their physical and mechanical properties. They are mostly use as aerospace materials, since other applications are not

fully exploited. Many potential applications of Ti will be discussed in this section.

Aerospace applications - High specific strength, good fatigue property, good fracture toughness and creep resistance make Ti a preferred metal for the aerospace application. Figure 2.3 shows a weight of mill Ti products per plane, where the rapid increase of Ti in airframe and engine of commercial aircrafts is visible [21]. The earliest product of titanium was for nacelles and firewall of the Douglas DC-7 airliner. At that time, Ti and its alloys were used for structural components on aircraft ranging from Boeing 747 to space satellites and missiles. Titanium research is important for improving the fuel efficiency of engine, and the usage of Ti in jet engine hot sections is applicable because it can withstand high temperatures. This is a successful development.

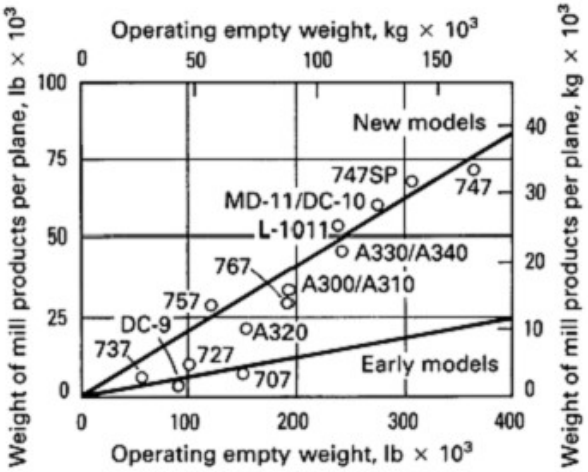

Fig. 2.3 Increasing of Ti mill products demand in early and new models of aircrafts for both airframe and engine applications [22].

Corrosion applications - Commercially pure Ti is more suitable in comparison to Ti alloys regarding corrosion applications. For chemical and petrochemical processing, the corrosion resistance of Ti equipment such as pump, vessel or storage tank is important for certain chemical production. In marine engineering, Ti is used in ship design and offshore oil platforms. The applications include thruster pump, propeller, and submarine components. Ti is also used for surgical implants because of its good corrosion resistance in human body fluid. Ti alloys are also used in

biomedical applications from hip and knee implants to implantable pump and components for artificial hearts. Porous surface of Ti implants promote ingrowth of bone, resulting in a good bonding between bone and the implant device.

Automobile applications - The applications of Ti in the automotive field are mostly in racing cars. Racing automobiles have made extensive use of Ti alloys for engine parts, drive system and suspension components. For commercial cars, not many manufacturers have used Ti on production model. Automotive parts that are considered to have a commercial potential for Ti applications are valve and valve retainer.

2.2.3 Commercially pure Ti

Pure Ti wrought products have a titanium content ranging from 98.635 to 99.5 wt%. Pure Ti products are commonly used in applications where high ductility or corrosion resistance is required. Table 2.1 and 2.2 show the physical properties of pure Ti in comparison with other structural materials, and chemical compositions of commercially pure Ti mill products with its mechanical properties, respectively.

Table 2.1 Physical properties of Ti and other structural materials.

Physical properties	Ti	Al	Fe	Cu
Density (g cm^{-3})	4.51	2.70	7.86	8.96
Thermal conductivity (W m^{-1} K^{-1})	22	235	80	401
Thermal expansion (μm m^{-1} K^{-1})	8.6	23.1	11.8	16.5
Heat capacity (J mol^{-1} K^{-1})	25.1	24.2	25.1	24.4
Electrical conductivity (10^6 cm^{-1} Ω^{-1})	0.023	0.377	0.099	0.596

Among structural materials, Ti is considered to be a light weight material with a density of 4.51 g/cm^3, which is only higher than Mg (1.74 g/cm^3) and Al (2.7 g/cm^3). According to physical properties of each structural material, Ti possesses much lower thermal conductivity and expansion coefficient comparing to Al and Cu, which makes Ti suitable for applications where the high specific strength and low thermal conductivity are required.

Table 2.2 Chemical compositions and standard mechanical properties of commercially pure Ti with different grade [23].

Designation	Compositions (wt%)					Tensile properties		
	C	H	O	N	Fe	UTS (MPa)	YS (MPa)	Elongation (%)
ASTM grade 1	0.1	a)	0.18	0.03	0.2	240	170	24
ASTM grade 2	0.1	a)	0.25	0.03	0.3	343	275	20
ASTM grade 3	0.1	a)	0.35	0.05	0.3	440	380	18
ASTM grade 4	0.1	a)	0.40	0.05	0.5	550	485	15
JIS class 1		0.015	0.15	0.05	0.2	275	165	27
JIS class 2		0.015	0.2	0.05	0.25	343	215	23
JIS class 3		0.015	0.3	0.07	0.3	480	345	18

a) Hydrogen limits vary according to product form as follow: 0.015H (sheet), 0.0125H (bar), 0.01H (billet)

Note: All listed values are minimums

Ti is a high reactive metal and has extremely high affinity to oxygen. Therefore, it can form a very stable oxide film on the surface. This oxide film forms spontaneously when a fresh metal surface exposes to air or moisture, and provides an excellent corrosion resistance of Ti. However, anhydrous condition in the absence of oxygen may result in Ti corrosion because the protective film cannot be generated, and lead to crevice corrosion. A crevice can originate from adhering process stream deposits, metal to metal joint and other seal joints. The mechanism of crevice corrosion of Ti is similar to stainless steel, where oxygen depletion induces an anodic reaction in tight crevice.

Hydrogen embrittlement of Ti could occur when it exposed to solution containing hydrogen at room or elevated temperatures [24]. However, Ti alloys are widely used in hydrogen containing environments or galvanic couples conditions causing hydrogen to directly contact with the metal surface. Although, hydrogen embrittlement is observed, oxygen and moisture in hydrogen gas containing environment formed an effective oxide film that avoids or limits hydrogen absorption. The hydrogen embrittlement can also occur at a low level of hydrogen content because it can induce a stress in a material.

The microstructure of unalloyed Ti at room temperature is commonly 100% α structure. Beta phase could be formed at α grain boundary if there are impurities in Ti (primarily iron). The unalloyed Ti after annealing may have an acicular or equiaxed alpha structure. Acicular α structure is formed during cooling at a temperature where ß phase transforms to α phase [25]. The acicular width depends on cooling rate, where a high cooling rate results in a thin and fine acicular structure. The equiaxed structure could only be formed by recrystallization of the material that experiences an extensive plastic deformation on α phase.

Effects of impurities on mechanical properties - Besides the effect on the lattice parameter and phase transformation temperature, the impurities also have effects on mechanical properties of Ti. Residual elements such as carbon, silicon, nitrogen or iron increase the strength of Ti but lower its ductility. The effect of interstitial elements on the tensile strength and elongation to failure of Ti is shown in Fig. 2.4

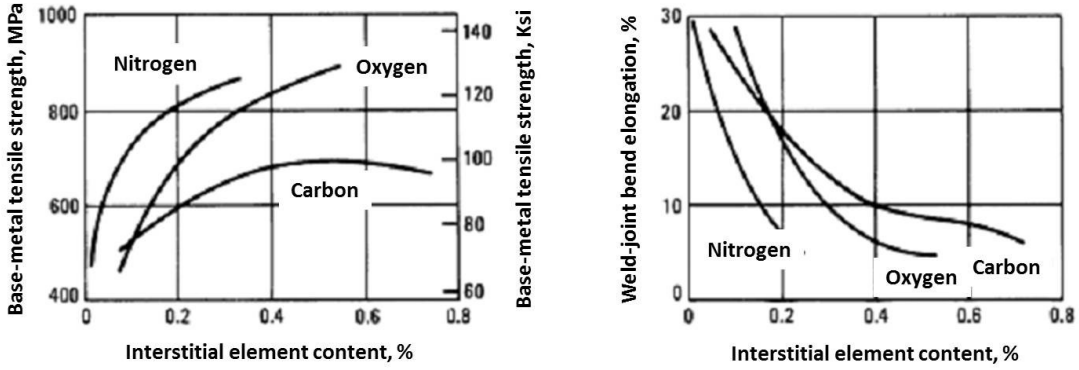

Fig. 2.4 Effect of interstitial elements content on tensile strength and bend elongation of unalloyed Ti [23].

Generally, oxygen and iron are residual elements that control the strength in commercially pure Ti. On the other hand, carbon and nitrogen are controlled at a low level to prevent embrittlement in Ti. The extra oxygen and iron content were intentionally added in some commercially grade Ti to provide an increased strength. For applications that require good ductility and toughness, extra-low interstitial (ELI) Ti materials are used. For ELI grades, the interstitial elements such as oxygen, nitrogen, hydrogen

and carbon must be held at an acceptable level because they lower the ductility of final products.

Properties of commercially pure Ti - In case of tensile and fatigue strengths, commercially pure Ti is not as strong as steel or Ti alloys. It has an intermediate modulus of elasticity which can be influenced by texture. Commercially pure Ti has impact strength comparable to that of quenched and tempered low alloy steel. Ti may exhibit an increase in toughness at low temperatures, depending on the control of interstitial impurities and brittle refractory constituent. Yield and creep strengths at allowable maximum deformation are important determination criterions depending on which one is lower at service temperature. At 200-315 ºC, deformation of Ti loaded to a yielding point does not increase with time. Thus, the creep strength is not an important factor in this range. Nonetheless, above 315 ºC, the creep strength becomes an important factor.

2.3 Magnesium and its alloys

2.3.1 Magnesium overview

Mg was first produced by Sir Humphry Davy in England. He used electrolysis on the mixture of mercury oxide and magnesia. He firstly designated it as magnea, but the name of magnesium is now used. Mg is an eight-most-abundant on the earth's crust by mass. It is mostly founded in the forms of magnesite, dolomite and ion in mineral water. The Mg^{2+} cation is a second most founded ion in sea water, which makes sea water and sea salt an attractive commercial source for Mg. The extraction of Mg from mineral is known as Pigeon process. This process is related to a reduction of MgO by silicon at high temperatures, as shown in eq. 2.3. The process can also be performed by carbon at a temperature of 2300 ºC, as shown in eq. 2.4.

$$2MgO_{(s)}+Si_{(s)}+2CaO_{(s)} \rightarrow 2Mg_{(g)}+Ca_2SiO_{4(s)} \quad \text{(eq. 2.3)}$$

$$MgO_{(s)}+C_{(s)} \rightarrow Mg_{(g)}+CO_{(g)} \quad \text{(eq. 2.4)}$$

Mg is the lightest structural material with a density of 1.74 g/cm^3. It is the third-most-commonly-used metal, following iron and aluminum. The main applications of Mg are alloyed with Al, sulfur reduction element during iron

and steel production, and used in a Ti production process (Kroll process). Mg has many advantages including the high specific strength and modulus that make it suitable for structural applications. However, there are also disadvantages that prevent some applications of Mg, such as poor formability, high reactivity to oxygen and water, low toughness and low strength at elevated temperatures.

Mg and Mg alloys are widely used in many applications including both structural and non-structural fields. The structural applications of Mg and its alloys include automotive, aerospace components and other industrial fields. In the automotive industry, applications include clutch, brake pedal support brackets and manual transmission housing. Mg alloys are valuable for aerospace applications because of their light weight and high specific strength and stiffness at room and elevated temperatures. Mg is also employed in various non-structural applications. For example, it is used as an alloying element in Al, Pb, and non-ferrous metals. It is also used as an oxygen scavenger and desulfurizer in iron and steel industry. Another important non-structural application of Mg is in Grignard reaction in organic chemistry. Al and Zn are common alloying elements in Mg alloys, their solid solubility in Mg decrease at low temperatures. Manganese is helpful in improving corrosion stability of Mg alloys that contained Al and Zn [26]. Several Mg alloys which employed Mn to control Fe content and activity in alloy are available and have excellent corrosion resistance. In addition, Mg alloys contain yttrium are also available and exhibit improved corrosion resistance.

Table 2.3 Physical and standard mechanical properties of various pure metals [27].

Properties	Mg	Al	Ti	Fe
Density (g/cm^3)	1.74	2.70	4.51	7.86
Crystal structure	hcp	fcc	hcp	bcc
Melting point (°C)	650	660	1668	1538
Thermal conductivity ($W\ m^{-1}\ K^{-1}$)	156	235	22	80
Tensile strength (MPa)	135	170	398	345
Elastic modulus	45	70	116	211

From Table 2.3, it can be seen that the density of Mg is considerably lower than other pure metals such as Al, Ti or Fe which their alloys are used for structural materials. Namely, it is about 64.4%, 38.6% and 22.1% of that

for Al, Ti and Fe, respectively. The tensile strength of Mg is lower than Al and Fe but while considering about the specific tensile strength, Mg exhibits a higher value than them.

2.3.2 Casting Mg alloys

High-pressure die casting alloys. There are three systems of commercial Mg alloys produced via high-pressure die casting: magnesium-aluminum-zinc (AZ), magnesium-aluminum-manganese (AM) and magnesium-aluminum- silicon (AS). Nominal compositions and casting methods for those alloys are given in Table 2.4. The most commonly used die cast Mg alloy is AZ91D, which exhibits good mechanical and physical properties in combination with excellent castability and corrosion resistance. For applications that require good ductility, AM60B is used instead of AZ91D. Despite a decrease in Al content, the tensile and yield strengths of AM60B are only slightly lower than AZ91D. The AM60B is used in die casting automobile wheels and some other sport equipment.

Sand and permanent mold casting alloys. There are several systems available for sand and permanent mold casting as follows:

- Magnesium-Aluminum-Manganese with and without Zinc (AZ and AM).
- Magnesium-Zirconium (K).
- Magnesium-Zirconium-Zinc with and without rare earth element (ZE and ZK).
- Magnesium-Thorium-Zirconium with and without Zinc (HZ and HK).
- Magnesium-Zinc-Copper-Manganese (ZC).
- Magnesium-Silver-Zirconium with rare earth or Thorium (QE and QH).

Table 2.4 Nominal compositions and casting methods of various Mg alloys [28].

Alloys	Compositions (wt%)			
	Al	Zn	Mn	Other
Sand and permanent mold casting				
AM100A-T6	10.0	-	0.10	-
AZ92A-T6	9.0	2.0	0.10	-
AZ63A-T6	6.0	3.0	0.10	-
AZ81A-T4	7.6	0.7	0.13	-
Die casting				
AS21X1	1.7	-	0.40	1.1Si
AM60A	6.0	-	0.13	-
AZ91	9.0	0.7	0.13	-

Mg-Al casting alloys. The magnesium permanent mold and sand casting alloys such as AZ63A, AZ81A, and AZ91 exhibit good castability, good ductility and moderate yield strength at temperatures up to 120 ºC. For AZ91E, iron, nickel and copper are controlled at a very low level. As a result, it exhibits excellent seawater corrosion resistance. For Mg-Al-Zn alloys, an increase in aluminum content results in the increase of yield strength and reduction of ductility.

2.3.3 Microstructure of Mg-Al alloys

In Mg-Al alloys such as AZ31B, AZ61 and AZ91, a eutectic structure is obtained by precipitation of intermetallic compound of $Mg_{17}Al_{12}$ on Mg matrix as shown in Fig. 2.5a. With normal or air cooling, this eutectic takes either of two forms depending on whether the alloy contains Zn or not. In an alloy without Zn, the eutectic forms as a massive compound that contains Mg solid solution islands. However, in an alloy containing Zn, the compound forms completely separate from Mg solid solution matrix. The precipitation of $Mg_{17}Al_{12}$ can be continuous or discontinuous. At an aging temperature above 205 ºC, $Mg_{17}Al_{12}$ becomes a continuous Widmanstätten (Fig. 2.5b). At an aging temperature lower than 205 ºC, the discontinuous precipitation forms at grain boundaries with a lamellar structure. The Mg-Al alloys contain Mn form various compounds including AlMn, Al_4Mn or Al_6Mn. These compounds may be contained as a single particle, where a ratio of Al to Mn increases from the center to surface of the particle. Solution heat treatment may transform the particle to Al_6Mn. The Al-Mn compounds often appear in the form of needle or chunk. When Zn is added in Mg-Al alloys,

the Mg-Al eutectic takes a completely separate form, in which massive particles of $Mg_{17}Al_{12}$ or $(Al, Zn)_{49}Mg_{32}$ are surrounded by Mg solid solution. The $(Al, Zn)_{49}Mg_{32}$ particle is formed when a ratio of Zn to Al exceeding 1 to 3.

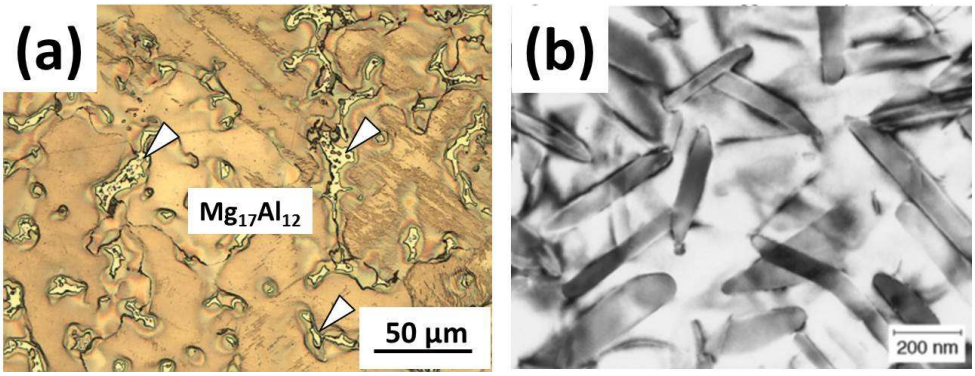

Fig. 2.5 Microstructure of Mg alloys (a) A co-existence between $Mg_{17}Al_{12}$ IMC and Mg matrix in as cast Mg-Al alloys (b) A Widmanstätten of $Mg_{17}Al_{12}$ obtained after aging at a temperature above 205 °C.

2.3.4 Mechanical properties of Mg and its alloys

Tensile strength. Tensile properties of various Mg alloys (casting and extruded material) are shown in Table 2.5. The yield and tensile strengths of Mg alloys are strongly dependent on Al content, where a higher Al content results in higher strengths. This improvement is due to the solid solution strengthening of Al and precipitation strengthening of $Mg_{17}Al_{12}$. However, an increase in strength always comes with a trade-off of ductility because of the existence of brittle compound, $Mg_{17}Al_{12}$. Mg alloy products fabricated by different methods can exhibit a large difference in tensile and yield strength even they possess the same Al content. This is because when the alloys are subjected to severe plastic deformation during extrusion, many dislocations are introduced into the matrix, which is known as work hardening.

Table 2.5 Tensile properties of various cast and extruded Mg alloys [28].

Alloys	YS (MPa)	UTS (MPa)	Elongation (%)
AZ80A-T5[a]	275	380	7
AZ61A[a]	230	310	16
AZ31B[a]	200	260	15
AZ10A[a]	145	240	10
AZ81A-T4[b]	83	275	15
AZ63A-T6[b]	130	275	5

[a] Extruded Mg alloys [b] Cast Mg alloys

Compressive strength. Compressive yield strength is defined as a stress that is required for generating a deviation or offset of 0.2% from the modulus line. For casting materials, compressive yield strength is approximately equal to tensile yield strength. For wrought alloys, however, the yield strength under compression can be lower than the yield strength under tension. The ratio of yield strength under compression to that under tension may vary from 0.4 for alloy M1A to an average value of 0.7 for other wrought Mg alloys.

Shear strength. Shear strength is an important property used in the design of joint in magnesium parts, such as thread joint and spot weld.

2.3.5 Design and weight reduction

Many structural parts can be substantially reduced in weight by substituting heavy structural materials such as Al alloys, steel or copper with Mg alloys with little or no redesign. For example, a replacement of steel with Mg alloy in car frame or automobile wheel. This is possible because technical limitations have made many parts heavier than necessary. In many cases, magnesium produced through forging, casting or extrusion can have comparable strength with the heavy metals without increasing in the wall thickness. Certainly, in some scenarios, Mg substitutions may require an increase in component thickness or a major redesign in order to achieve maximum weight saving. The bending strength and stiffness of structural component can be increased by designing the component to be a square or cube. Therefore, it is possible to obtain a large increase in the strength and stiffness with moderate increase in thickness and cross-

sectional area. When increasing in depth is acceptable, it is useful to redesign the part by using Mg for economical purpose. A reduction in stability allows design simplification and reduces manufacturing cost. Table 2.6 shows a tensile strength, young modulus and weight of various structural materials with same thickness. Mg alloys substitution of Ti alloys can reduce a weight of component by 62.6% with a decrease of approximately 70% of tensile strength (AZ31B extrusion and AZ91 cast). This weight reduction is considerably large for structural application when high strength is not required. Even comparing to Al sheet, a weight reduction could be achieved by 22.6% with a small decrease of tensile strength and young modulus. These data show a potential of Mg alloys for weight reduction.

Table 2.6 Tensile strength, young modulus and weight of various structural materials with same thickness [29].

Materials	Tensile strength	Young modulus	Weight	HT condition
Ti-6Al-4V	100.0	100.0	100.0	Annealed
6061-T6 Al sheet	33.3	34.5	60.0	T6
AZ31B extrusion	28.0	22.4	37.4	-
AZ91 cast	29.6	23.1	37.4	T6

Note: All comparison express in percent (%) which compare to properties of Ti-6Al-4V.

HT: Heat treatment, T6: Solution treatment and aging

2.4 Joining of Ti and Mg alloys

2.4.1 Introduction of joining technique

Many joining techniques can be applied in industrial manufacturing, and offer flexibility in fabrication of structural components. It is important to distinguish joints connecting between similar materials (metal, ceramic or plastic) and those between dissimilar materials. In the case of dissimilar materials, the engineering compatibility between two materials must be considered. For example, mismatch between elastic modulus of the materials is one of the mechanical compatibilities. If two materials possessing a large difference in their elastic modulus, it may lead to the formation of stress concentration and stress discontinuities at the bonding

interface between the two materials. Another factor that must be considered is the physical compatibility. A thermal expansion mismatch represents a poor physical compatibility and this is a regular problem when joining a metal to ceramic. A mismatch in thermal expansion leads to the development of thermal stress that occurs locally at the joint and reduces its load-carrying capability. This problem can cause the failure of bonded components. In addition, the poor chemical compatibility associates with undesired chemical reaction near the neighborhood of joint area. For example, formation of brittle intermetallic compounds at the bonding interface after joining, or formation of an electrochemical corrosion couple at the contact area because of an electrochemical potential difference between the two materials can lead to the failure of bonded components [30].

Joining between different materials requires a careful selection of joining methods. Many of joining methods have a potential to bond different materials together and will be discussed in this chapter. Joining between pure Ti and Mg alloys is a challenge work since no intermetallic compound can be formed by them referring to their binary phase diagram (Fig. 2.6). Some researchers proposed that the ternary compound between Ti-Al-Mg could be formed as $Ti_2Mg_3Al_{18}$ which was located only in aluminum-rich areas. The materials had to be melted in the production process or fabricated by the special process [112]. Furthermore, the mismatch of physical and mechanical compatibility between pure Ti and Mg alloys may cause problems in joining process. For example, a large difference in melting points and young modulus (E) between pure Ti (E= 116 GPa, T_m = 1668 ºC) and Mg alloys (E ~ 45 GPa, T_m ~ 650 ºC) can lead to a failure in joining.

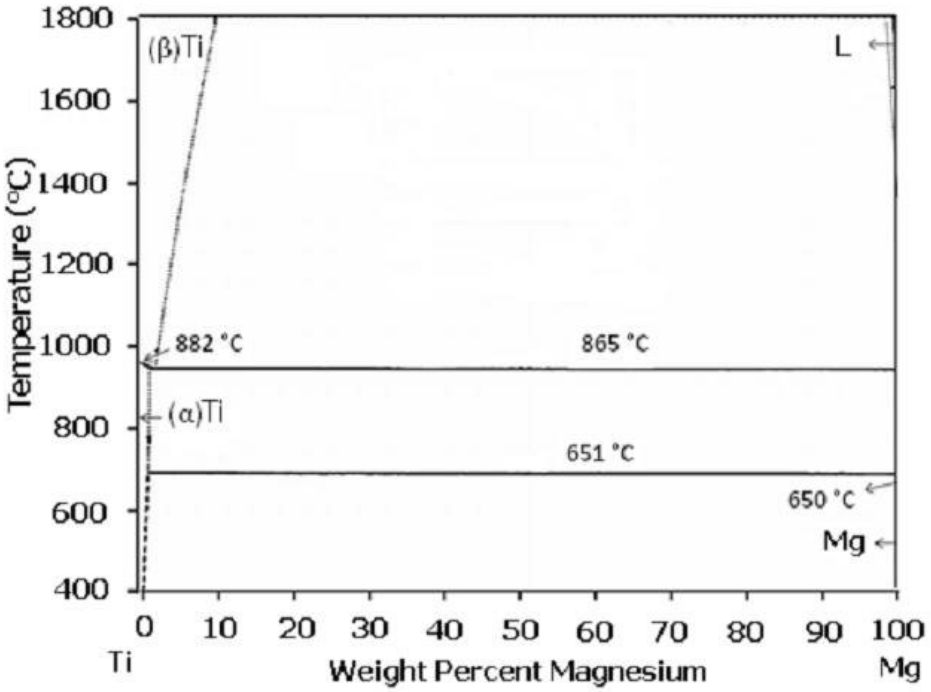

Fig. 2.6 Binary phase diagram between Titanium and Magnesium [16].

2.4.2 Adhesive bonding

Adhesive bonding is also referred as glue bonding, and it can be described as a wafer bonding technique that applies intermediate layer to connect two different materials. The materials used for adhesive bonding can be divided in two types, thermoplastic (which is soluble in water and melts when heating) and thermosetting (which is non-soluble in water and burns when heating). There are many advantages of adhesive bonding, such as uniform distribution of stress, no deformation of parent metals after bonding, applicable for irregular surface [31]. Moreover, this bonding process can perform at a relatively low temperature and no electric voltage and current are required. Since the surface of bonded materials does not contact directly, this method has some potentials in joining different materials, for example metal-to-ceramic or metal-to-polymer. The process also has some limitations such as safety problem, because adhesive materials are usually flammable. In addition, chemical emission is not controlled and it is very time consuming for curing. The main disadvantage of this joining process is the very limited application temperature. As is known, the thermal instability usually occurs at a temperature above 300 ºC

for common adhesive materials, and these materials are also sensitive to extreme environments (where includes water and humidity). Joint design is critical for success in adhesive bonding, where it is encouraged for using in shear applications [32].

2.4.3 Soldering and brazing

Soldering and brazing are bonding process which involved a use of filler metal that has a melting temperature below the melting point of the components to be joined. The difference between soldering and brazing is the melting temperature of filler metal, where soldering uses a lower melting temperature (lower than 450 ºC) than brazing. The melting point of the filler metal that applied in brazing may approach that of one of the components to be bonded. The bonding mechanism basically contains three steps that start with wetting the filler metal on the surfaces of bonding components, and then alloy between filler metal and bonding components, and finally spread the molten metal through a capillary action. The brazing process can be carried out in vacuum. Soldering and brazing are considered as two joining techniques which can solve the problem facing in fusion welding, since the parent metals still in solid state during processing. In addition, brazing is also considered as one of the most acceptable methods for joining dissimilar metals and alloys.

R. Cao et al. (2014) studied the joining between pure Ti and AZ31B by a cold metal transfer (CMT) welding brazing method. A satisfied welding joint was obtained at suitable welding condition by using AZ61 as the filler metal. The brazing interface is mainly composed of Ti_3Al, $Mg_{17}Al_{12}$ and $Mg_{0.97}Zn_{0.03}$ intermetallic compounds. Al and Zn were reported as important elements in joining pure Ti to AZ31B successfully [33].

S. Chen et al. (2011) studied the joining between Ti64 (Ti-6Al-4V) and 5A06 Al alloys by a laser welding-brazing method. The two materials were bonded well together by using Al-Si wire as the filler metal. The fusion welding zones were divided into three, which are fusion line zone, columnar crystal zone and equiaxed crystal zone. The microstructures in the brazing zone are in order of α-Ti, nanosize granular $Ti_7Al_5Si_{12}$ and serration-shaped $TiAl_3$ from the Ti alloy matrix to the seam. The reaction between Ti, Al, and Si was considered to be an important bonding mechanism [34].

2.4.4 Fusion welding

In fusion welding, two components are joined by heating at the interface region above the melting point of one or both of the matrixes. It is different from soldering and brazing, in which a low melting point filler metal is used for joining, as well as from diffusion bonding, in which the temperature at the bonding interface is not exceeding the melting point of all phases present. Fusion welding is one of the most versatile and effective means available for the assembly of individual components into larger module for both large and small engineering systems. Weld assemblies are able to carry loads similar to those supported by individual components from which they are constructed. No mechanical bond can compete in its high strength to weight ratio with this load carrying efficiency of a welding joint. No adhesive bond can match the tensile strength or shear strength of a welded joint. If disassembly is not a requirement, then welding is a first candidate of joining methods. However, for Ti-Mg alloys bonding, fusion welding was not a suitable method since Mg alloys are very easy to evaporate during melting, and brittle phases may be formed at the bonding interface after cooling.

M. Esmaily et al. studied the joining between Ti64 by gas tungsten arc welding (GTAW). The parent metals were joined well together at welding voltages of 100 and 110 V. Higher voltage than 110 V caused a melting at the edge of plates. The microstructure at fusion zone was depended on heat input and the cooling rate. The less heat input following with faster cooling rates produces a more basket-weave microstructure. Increasing the heat input results in decreasing in the cooling rate, where the resultant microstructure at fusion zone is acicular α+ß phase [35].

S. Takhti et al. studied the joining between cast A356 Al alloys by using Al-Si as a filler metal. The microstructure of the base metal after welding consists of coarse dendrite of α-Al and eutectic mixture. In the HAZ, the eutectic structure coarsens and separates into Al matrix and Si particles. The fusion zone appears as a fine dendrite structure. The primary α in the fusion zone becomes fine and roughly equiaxed when increasing the pulse frequency. These materials showed a good tensile strength without fracture occurring at the fusion zone [36].

G. Casalino et al. studied the joining between pure Ti and the 5754Al alloy by Yb-YAG laser offset welding. Neither a filler metal nor groove

preparation was necessary to produce a sound joint. Good bonding interface at the Al alloy side was obtained with no porosity or spatter. The morphology analysis revealed a linear or curvilinear of IMC layer depending on energy input and laser offset. The fracture occurred at the IMC layer with an open fracture mode [37].

2.4.5 Transient liquid phase welding

Transient liquid phase (TLP) bonding is a variation in a solid state bonding process and has been used to join advanced metals. It is one specific isothermal bonding technique, which has been developed for high performance superalloys, to achieve an ideal bond. The bonding zone has engineering properties, composition and microstructure close to those of the components. The process is based on the use of chromium and nickel interlayer with several percentages of boron, which drastically reduces the melting temperature of pure Ni (Fig. 2.7).

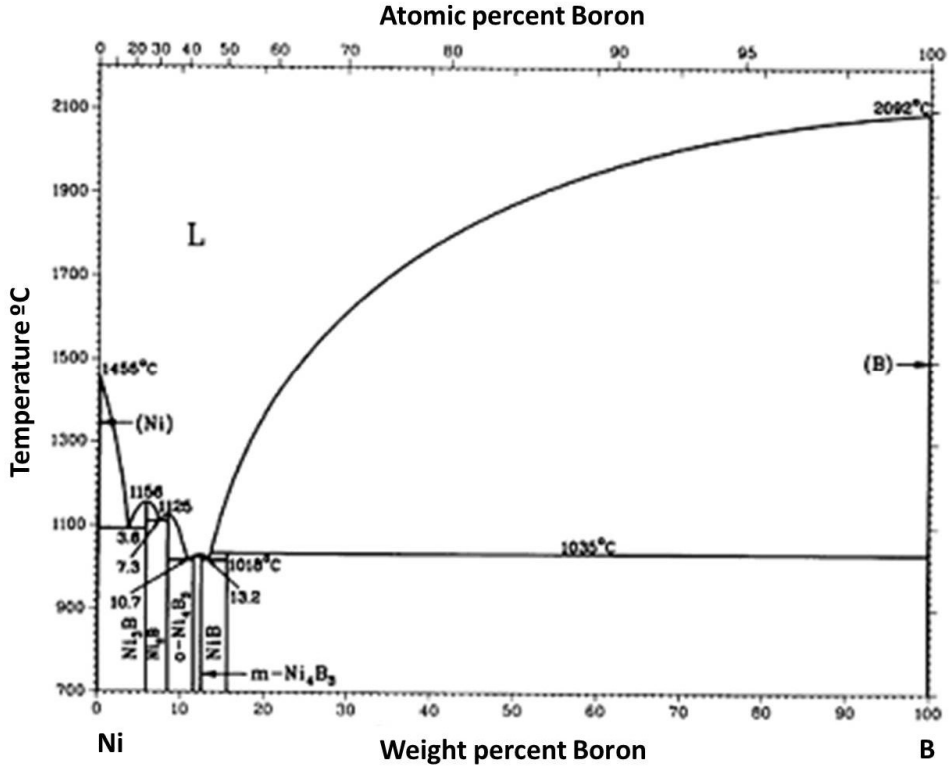

Fig. 2.7 Ni-B binary phase diagram. Addition of non-metallic, interstitial boron drastically reduces a melting point of nickel.

The diffusion rate of boron in solid state is extremely rapid near the melting point, since boron is present in interstitial solid solution. The Cr-B alloy interlayer is chosen for bonding superalloys with a bcc structure (Cr-Fe based alloys), while Ni-B interlayer is selected for fcc superalloys (Ni-Co based alloys). The interlayer is sandwiched between the components to be bonded and the assembly then is heated in a protective atmosphere to a temperature over melting point of the interlayer. The molten interlayer wets the components and boron diffuses rapidly into the components. As the boron diffuses, the melting temperature of the molten interlayer rises, until it exceeds bonding temperature. The whole bonding process occurs isothermally, and it is known as transient liquid phase bonding [38].

Cam et al. studied the joining between TiAl and Ti64. The joining between these two materials was achieved by using TLP bonding, and the process parameters (temperature, time and pressure) were optimized to obtain good shear strength. The joint strengths were less than that of parent metals, and this was attributed to the presence of brittle α_2 layer at the bonding interface. The optimum joining condition was found at 850 ºC and 5 MPa. The highest joint shear strength was obtained at a bonding time of 15 min. When bonding time was increased to 30 and 45 min, the shear strength decreased due to an increasing in the amount and size of brittle α_2 phase at the bonding interface [39].

Gale et al. suggested that TLP bonding allows joining non-weldable materials, especially those materials used for high temperature application. In brazing, an oxide can be formed at the contact interface and filler metal normally appears in the final joint, and thus prevents the use of brazing at high temperature. TLP bonding can overcome those problems and produce ideal joint microstructure, characteristic and properties that like the parent metal, which makes bonding intermetallic compounds possible [40].

Alhazaa et al. and Kenevisi et al. studied the joining between Ti-6Al-4V and Al7075 by TLP bonding. In addition to the process parameters, the interlayer material shows an important role on the joining strength and microstructure development. Both alloys used in this research are aerospace alloys that have attractive properties such as high specific strength and good corrosion resistance. Al7075 is 40% lighter than Ti-6Al-4V alloy and is much cheaper. Ti-6Al-4V alloy has superior mechanical properties than Al7075. Thus, joining of these alloys is very attractive for a wide range of

engineering applications. The use of traditional fusion welding to join these two materials is not suitable because of their difference in mechanical and physical properties. The formation of an oxide layer at the surface of these alloys hinders the application of other joining techniques. However, TLP bonding can remove oxide at the aluminum surface and results in good joint due to better wettability at the joint. Different interlayers have been used to facilitate bond in a solid state and in the TLP bonding process. In solid state bonding without interlayer, the successful bonding is possible when a higher temperature and pressure are used in comparison with that an interlayer. The effect of bonding time is also noticeable on the joint microstructure and mechanical properties [41-44].

2.4.6 Friction stir welding

Friction stir welding (FSW) is a relatively new technique for bonding. This bonding method is capable to join high-strength aerospace aluminum alloys and other metallic alloys that are difficult to weld by conventional friction welding. This bonding technique is energy efficient, environment friendly and versatile. Friction stir welding is a solid-state bonding method, and it is initially applied to Al alloys. The bonding concept of FSW is very simple. A non-consumable rotating tool with a specially designed pin and shoulder is inserted into the contact region of sheets or plates to be joined and moves along the line of joint in high speed rotation (Fig. 2.8). The tool provides heat to the workpiece with a movement of material to produce the joint. The localized heating softens the material around the pin and with the help of tool rotation that transfers the material from the front of the pin to its back. As a result of this process, a joint is produced in solid state. During the FSW process, the material experiences an intense plastic deformation at an elevated temperature, resulting in the formation of fine and equiaxed grains due to dynamic recrystallization. The fine microstructure obtained in FSW provides good mechanical properties in joining materials [45].

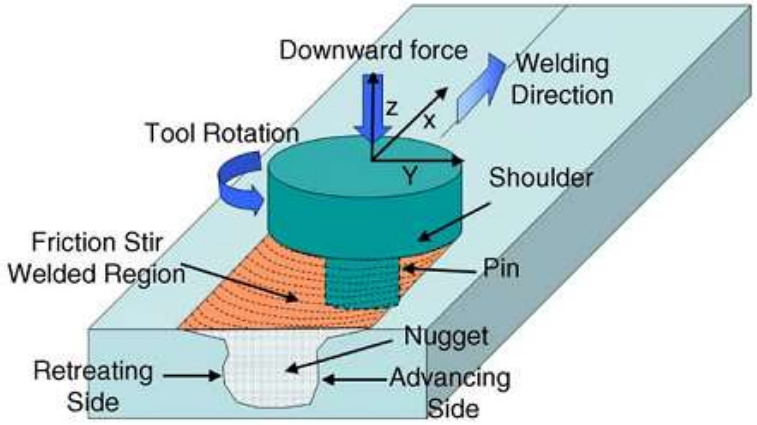

Fig. 2.8 Schematic drawing of friction stir welding (FSW) [46].

Li et al. fabricated a Ti64/Al bimetal clad plate by applying FSW with multi passes, following with annealing at various temperatures. The Ti64/Al metallurgical bonding interlayer at the clad plate interface demonstrated good densification and considerable thickness. They suggested that the FSW thermo-mechanical effect was the main mechanism to form the Ti64/Al interface structure. The post heat treatment at 400-500 ºC for 1 h can generate a homogeneous multi-island structure of Al and $TiAl_3$, which improves the bonding strength of the Ti64/Al clad material [47].

Dorbane et al. studied the bonding between AZ31B (Mg alloy) and Al 6061-T6 aluminum alloys by the FSW method. At the stir zone, grain sizes in both Mg and Al rich side were refined by dynamic recrystallization, and a thin IMC layer was formed. This IMC layer also has an effect on the bonding strength of the bonded materials, but the dominant factor was the reduction of grain size in the stir zone. The increase in average grain size resulted in an increased strain to failure and a decreased strength. The materials after bonding showed brittle fracture characteristic at the bonding interface where cracks generally initiated from the IMC of Mg and Al [48].

2.4.7 Diffusion bonding

Diffusion bonding is also a solid state bonding process based on the careful application of the applied pressure and temperature, and involves thermally activated creep deformation of either one of the components. All such processes are termed as diffusion bonding. Diffusion bonding processes

depend on a combination of three factors for their success [49].

1. Absence of contamination at the mating surface and surface polishing. The surface must be clean and in many cases has to be polished before bonding.
2. The ability of at least one component to undergo sufficient plastic flow (creep) in order to develop complete contact along the interface between the components.
3. Sufficient time for diffusion to occur at the interface region in order to obtain the complete reaction and establish an adequate bonding strength.

Thermal mismatch. Another essential condition that should be added to the three factors is the thermal expansion characteristic of the components over the temperature ranging from room temperature to a temperature required for diffusion bonding so as to minimize the thermal stress in the assembled joint [50]. When one of the components is ductile, the level of shear stress at the interface is of the order of the yield strength for the ductile component. If the other component is brittle, the fracture strength of the bonded material can be reduced to a value given by equation 2.5,

$$\sigma_b = \frac{K_c}{\sqrt{\pi c}} - \sigma_y \qquad \text{(eq. 2.5)}$$

where K_c is the fracture toughness of the brittle component (MPa$\sqrt{m}$), c is the dimension of the largest inherent interfacial defect (m) and σ_y is the yield strength of the ductile component (the residual stress in joint) (MPa). The elastic mismatch between the two components can impact this relationship. Surely, the actual bonding strength depends on the loading condition (tensile or shear, uniaxial or biaxial), but the equation does give a clear indication of the defect size, fracture toughness of the brittle component and yield strength of the ductile component on the bonding strength. This equation can be applied to dissimilar bonding materials. Surface contamination is prevented during bonding through a controlled atmosphere, usually a reduced atmosphere (wet or dry hydrogen) in vacuum or dry argon [51].

Surface finish. All surfaces must be adequately prepared before bonding, including both chemical cleaning (as well as degreasing with organic solvent) and mechanical abrasion. A variety of abrasives are used, ranging from silica for sand blast a component to diamond or Al_2O_3 powder paste in

submicron mechanical polishing. The four terms erosion, abrasion, lapping and polishing refer to four distinct mechanisms for achieving a surface finish. Sand blasting is an erosion process, in which the kinetic energy of particles that are carried in an air jet does the mechanical work when the particles strike the surface [52]. Abrasion makes use of grid particles that have been bonded to either a flexible or rigid substrate. Most abrasion processes employ a fluid coolant, which can be water or a commercial machining fluid. Lapping differs from abrasion in that the grit particle is free to move on the carried substrate. For the lapping process, the particle-embedded depth is generally reduced comparing to abrasion, resulting in a smaller depth to be removed once a time with less surface damage and better surface finish. Polishing refers to preparing mirror finish, corresponding to a surface roughness below the wave length of visible light (0.4-0.7 μm). Chemical polishing employs chemical agent that forms a viscous layer at the surface, resulting in preferential removal of any protrusions [53]. Electropolishing achieves the same result by forming a viscous layer of high electrical resistance at the anode. This method is only suitable for electrically conductible materials [54]. Mechanochemical polishing is sometime possible, in which chemically active cooling fluid is used with the polishing grit.

Plastic flow. Diffusion bonding requires yielding and plastic deformation of at least one component to reduce residual porosity at the interface so as to increase the true contact area at the joint until it is equal to nominal area of contact. As the original contact point develops and links up during the diffusion bonding process, the local stress decreases in inverse proportion to the true area of contact. The rate of plastic flow in the region of the contact points is determined by the local stress and the bonding temperature, and can also decrease as the true contact area increases [55]. Ashby has identified the principle mechanism for plastic flow in metals, alloys and ceramics, with the governing equations for time-dependent plastic flow [56]. Generally, small creep relaxation is expected to take place at temperatures less than $0.6T_m$, where T_m is the melting point in K. On the other hand, the diffusion bonding generally requires a temperature of the order of $0.8T_m$ to ensure the sufficient plastic flow to occur (T_m is now a melting point of the less refractory material). The strain rate generally increases exponentially with the temperature, but follows a power law dependence on stress (eq. 2.6

and 2.7).

$$\ln\left(\frac{\varepsilon}{\varepsilon_0}\right) = \frac{-Q}{RT} \text{ (}\sigma \text{ constant)} \qquad \text{(eq. 2.6)}$$

$$\frac{\varepsilon}{\varepsilon_0} = \left(\frac{\sigma}{\sigma_0}\right)^n \text{ (T constant)} \qquad \text{(eq. 2.7)}$$

n is typically in the range from 2 to 10.

Since the local stress decreases as the contact area increases, most of the time requires for diffusion bonding is associated with the final stages of the bonding, corresponding to the elimination of individual pores. In the final stage, the radius of curvature of isolated pores provides a hydrostatic driving force for pore closure (eq. 2.8). Two populations of residual pores may develop. Those larger pores result from geometrical mismatch of the mating surface, and the finer pores which present in microscopic scales are corresponding to the original surface topology [32].

$$\Delta P = \gamma\left(\frac{1}{r_1} + \frac{1}{r_2}\right) \qquad \text{(eq. 2.8)}$$

The former can be extremely difficult to eliminate. The macroscopic pores can be reduced in scale by employing a fine sand paper for the final surface abrasion, in order to reduce a spacing of the original contact points. The optimum results are often obtained for a specific surface roughness which inhibits the formation of the larger, isolated pores but still leaves behind the small pores which are able to shrink under hydrostatic capillary pressure [57]. The aim of discussion on the influence of the surface topology is that the initial surface finish can be more important than the applied pressure for an ideal bonding. General yielding at high temperature ($0.8T_m$) may occur at a pressure less than 50 MPa so that applied bonding pressure must be limited to the order of 20 MPa. Therefore, the bonding pressure must be kept below the stress for general yielding, so as to avoid distortion of the component.

Diffusion. Pore shrinkage depends on the diffusion rate of the material that determines the volume of atoms that can be transferred in the solid state. The mechanism of mass transfer determines the activation energy for the process. Surface, boundary and bulk diffusions are all possible contenders. However, boundary diffusion is the most common limiting case, and involves the migration of vacant lattice site from the pore surface into the boundary,

where the vacancies are absorbed (the boundary acting as a vacancy sinks). Shrinkage of the pores is thus accompanied by migration of the center of gravity of the grain toward the plane of the boundary [58].

The diffusion rate is usually analyzed in term of Fick's first two laws. The first controls the net flux of atoms in a concentration gradient, as shown in eq. 2.9 [59].

$$J_x = -D \cdot \frac{\partial c}{\partial x} \qquad \text{(eq. 2.9)}$$

J = Diffusion flux (mol/m^2·s).
D = diffusion coefficient (m^2/s).
c = concentration (mol/m^3).
x = distance (m).

Fick's second law determines the rate of change of flux (eq. 2.10). A common result for planar diffusion is the error function solution in which the diffusion distance is normalized by the parameter "$2\sqrt{Dt}$". The diffusion coefficient is an exponential function of the temperature (eq. 2.11) and the normalized diffusion distance must also depend on the temperature [60]. The minimum diffusion distance required to ensure pore closure is several folds of the pore diameter. On the other hand, the activation energy most probably approximates that for boundary diffusion.

$$\frac{\partial c}{\partial t} = D \frac{\partial^2 c}{\partial x^2} \qquad \text{(eq. 2.10)}$$

t = time (s).

$$D = D_0 \exp\left(\frac{-Q}{RT}\right) \qquad \text{(eq. 2.11)}$$

Table 2.7 lists some values for the diffusion coefficients for bulk diffusion.

Table 2.7 Diffusion data for selected pure metals [61].

Metals	Solute elements	Temp. Range [°C]	Q [kcal/mol]	D_0 [cm^2/s]
Al	Al	450-650	34.0	17.10
	Cu	433-652	32.3	0.65
	Ga	406-652	29.2	0.48
Mg	Mg	467-635	32.5	1.50
	Fe	400-600	21.2	4.0×10^{-6}
	Ni	400-600	22.9	1.2×10^{-5}
Ti(β)	Ti	900-1540	31.2	3.6×10^{-4}
	Cr	950-1600	5.1	5.0×10^{-3}
	Fe	900-1600	31.6	7.8×10^{-3}

Lee et al. studied the bonding between ELI graded Ti-6Al-4V by applying the diffusion bonding method. Bonding was completed by means of inert gas pressure applied in the bonding tool at a high temperature. The evidence of nucleation of new grains and migration of grain boundaries at the interface proved that the diffusion process was successful. Moreover, it was shown that the super plastic forming and diffusion bonding is possible for ELI graded Ti-6Al-4V at temperatures lower than that for conventional Ti-6Al-4V [62].

Elrefaey et al. studied the bonding between Ti and low carbon steel by using a Cu alloy sheet as an interlayer. The successful joining was obtained at a temperature of 850 °C. The Cu interlayer was successfully employed to inhibit a mutual diffusion between Ti and Fe. The hard and brittle Fe-Ti and Ti-C intermetallics were not formed at the bonded joint. In spite of the formation of Cu-Ti intermetallic at the interface structure, it is less detrimental on the strength of the joint than the Ti-Fe intermetallic [63].

T. Vigraman et al. studied the joining between Ti-6Al-4V and AISI 304L. The samples were bonded at 900 °C with a bonding pressure of 4 MPa for 60 min following with annealing, and showed a maximum tensile strength of 242.6 MPa. This bonding strength is 41.6% and 25.3% of AISI 304L and Ti-6Al-4V, respectively. Many of intermetallic compounds could be detected at the bonding interface such as Fe_2Ti, $TiNi_2$, Ti_2Si_2, Al_6Ti_{19} and $Fe_3Al_2Si_4$. By observation, these phases impaired mechanical properties of the bonded materials [64].

2.4.9 Diffusion of Al atom in Mg

There are many researchers studying the diffusion of Al in Mg by mean of experimental or simulation methods. For example, by studying the microstructure evolution and mechanical properties of Mg/Al dissimilar materials fabricated by vacuum diffusion bonding at 475 ºC for 80 min, Liu et al. found that, at the first stage, the Mg and Al atoms exhibited an interdiffusion process that results in the formation of Al based solid solution (α) and Mg based solid solution (δ) on the Al and Mg side, respectively. The liquid micro-area occurred when it maintained at 475 ºC for enough time until the solubility limits of Al and Mg were exceeded. The supersaturated solid solution is unstable, and Mg_2Al_3 and $Mg_{17}Al_{12}$ intermediate phases can be nucleated. Finally, these IMCs grow transversely and form a whole body. The relationship between the thickness of IMCs and the bonding time can be described in eq. 2.12 for diffusion-controlled growth of a phase with a semi-infinite boundary condition.

$$\Delta x^2 = k(t - t_d) \quad \text{.....eq. 2.12}$$

When Δx = Thickness of IMC (μm)

k = Parabolic growth constant ($\mu m^2/s$)

t = Bonding time (s)

t_d = Latent time (s)

The calculated thickness of the intermetallic compound was in good agreement with experimental results. The thickness of Mg_2Al_3 was larger than $Mg_{17}Al_{12}$ for all the bonding conditions. This is because the energy barrier to nucleation and growth for Mg_2Al_3 is much lower than that for $Mg_{17}Al_{12}$. Besides, Mg_2Al_3 also exhibits lower activation energy for growth than $Mg_{17}Al_{12}$, where the values are 127 and 195 kJ/mol, respectively. These results imply that the diffusion rate of Mg into Al was higher than that of Al into Mg [109].

Jafarian et al. studied the effect of thermal tempering on the microstructure and mechanical properties of the bonded materials between AZ31 (Mg alloy) and Al-6061 (Al alloy) via diffusion bonding. Two types of Al alloys, where one is solution treated and aged (T6) Al alloy and the other is annealed Al alloy, were applied in their study. The solution treated and

aged Al alloy showed higher compressive strength and hardness than the annealed Al alloy. The microstructure at the bonding interface of AZ31 bonded to solution treated and aged Al alloy (AM1) and AZ31 bonded to annealed Al alloy (AM2) showed the similar characteristics to Liu's work. The Mg_2Al_3 and $Mg_{17}Al_{12}$ intermetallic compounds were observed near the interface of Al alloy and Mg alloy, respectively. The high compressive strength and hardness of T6 Al alloy resulted from an increase of the time that used for eliminating the surface roughness by plastic deformation. The Mg atoms in AM1 were difficult to diffuse into Al lattice, and therefore they tended to accumulate in the Mg alloy surface.

In this condition, the supersaturated solid solution was easier to form on Mg alloy surface in AM1 than that in AM2. In diffusion bonding, when the concentration reaches a critical level, reaction may occur between the elements and therefore an interaction layer is formed. From this explanation, each IMCs layer in AM1 had a larger thickness compared to AM2, and this made shear strength of AM1 lower than AM2. In AM2 bonded materials, mutual diffusion of atoms on both sides led to the delay in formation of supersaturated solid solution which reduced the thickness of IMCs layer. The lack of Kirkendall cavities in surface transition zone can be attributed to the similarity of the diffusion coefficients of aluminum and magnesium as much as 2.29×10^{-12} and 1.89×10^{-12} m^2/s, respectively. The another reason for explaining the more diffusion of the Mg atoms in AM2 bonding is the further loosening of bonds between Al atoms in annealed Al alloy by the applied force. Thus, the bonds could be broken easily and the vacancies were quickly formed. This causes the diffusion of Mg atoms into the Al lattice in AM2 much easier than that in AM1 [110].

In order to form the intermetallic compounds during diffusion bonding, intermetallic compounds are formed sequentially, where the second phase begins to nucleate and grow when the first phase reaches a certain thickness. In addition, the process of the formation of intermetallic compounds is highly dependent on the thickness of base metals. In early stages of the formation and growth of intermetallic compounds during diffusion bonding, diffusion occurs in both sides with different rates along with the formation of a supersaturated solid solution. The crystal nucleation of new phases is formed in defects. Where the concentration of the diffused element is high, crystal nucleation of intermetallic compounds

will grow along the interface. Many of this growth nucleation come together and normally grow longitudinally. Afterwards, the crystal nucleation of the second intermetallic compound will form and grow in the interface.

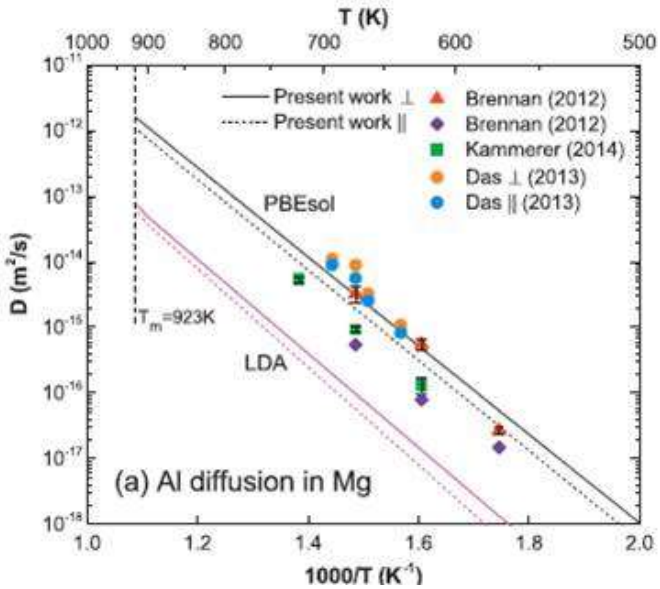

Fig. 2.9 Predicted dilute solute tracer diffusion coefficients of Al in Mg along with available experimental data.

Zhou et al. calculated the diffusion coefficient of solute atom in dilute Mg alloys by using first-principles calculations based on density functional theory (DFT). It is shown that the recently developed PBEsol exchange-correlation (X-C) functional gives better agreement with experimental data compared with the commonly used X-C functions such as the local density approximation (LDA). Solute diffusion results of Al from LDA slope agree well with experiments but consistently underestimate intersects of diffusion coefficient (D_0), as shown in Fig. 2.9. The diffusion coefficient of Al in Mg is significantly increases by increasing temperature. Ti, V, Cr, Mn do not form favorable bonds with Mg. In binary Mg-X alloy systems with these elements, no ordered intermetallic compounds are experimentally observed. These alloying elements in hcp Mg also tend to have positive enthalpies of mixing, often indicating an energetic preference for phase separation and limited solid solubility [111].

2.5 Corrosion behavior of bonded materials

2.5.1 Galvanic corrosion

Galvanic corrosion occurs when metals or alloys are electrically coupled to another metal or conducting nonmetal in the same electrolyte. A mixed metal system in a common electrolyte that is electrically isolate cannot experience galvanic corrosion [65]. During galvanic coupling, a metal that possess less corrosion resistance will corrode and the surface becomes anodic. The driving force for corrosion or current flow is the potential developed between two dissimilar materials. The difference in potentials causes electron flow between them, when they are electrically couples in an electrolytic solution. A galvanic series of metals and alloys were used for predicting galvanic relationships (Fig. 2.10). The series provides an arrangement of metals and alloys according to their potentials measured in a specific electrolyte. The potentials of metals and alloys are affected by environmental factors. Corrosion product film and other changes in surface composition can occur in some environment [66].

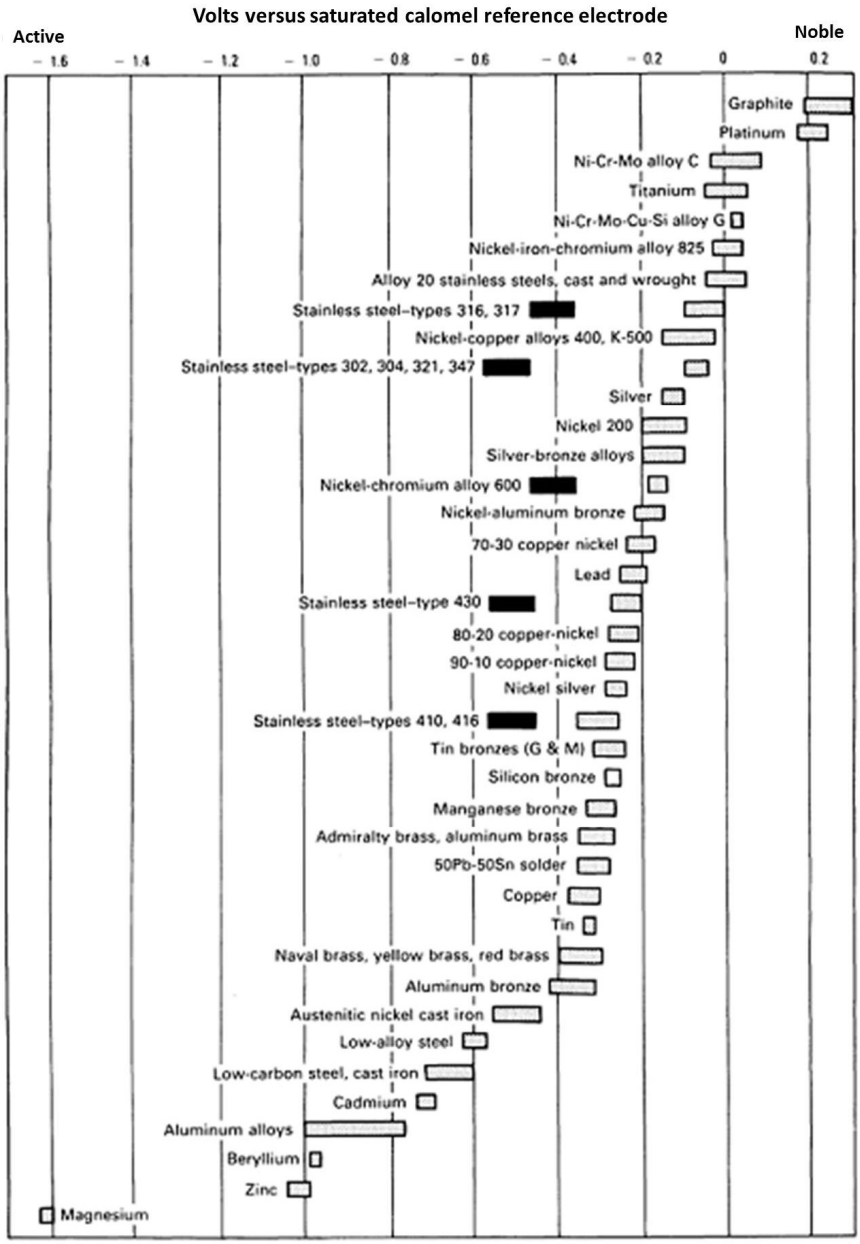

Fig. 2.10 Galvanic series for sea water of various materials [67].

Polarization. During galvanic corrosion, electrons flow from the noble end to an active end. This causes a change in potential by polarization because the potential of metals or alloys tends to approach each other. The magnitude of shift depends on environment and the initial potential. The nobler the metals or alloys are, the more the potential shifts toward the

active metals or alloys. The shift in potential of the active metals or alloys in the direction of cathode is therefore minimized so that accelerated galvanic corrosion is not as great as expected. On the other hand, when the noble metals or alloys are not ready to polarize, the potential of the active metal shifts further toward cathode, such that appreciable accelerated galvanic corrosion occur [68].

Factor such as area ratio, distance between electrical materials and their geometric shapes also affect the galvanic corrosion behavior.

Area effect. Area effect on a galvanic corrosion involves the ratio of the surface area of the noble to active member [69]. When a surface area of noble metal or alloy is larger than an active member, an unfavorable area ratio exists for the prevailing situation in which couple is under cathodic control. The anodic current density on the active metal or alloy is extremely large. Therefore, the resulting polarization leads to pronounced galvanic corrosion. On the other hand, large active member surface and small noble member surface produced only slightly accelerated galvanic effect [70].

Effect of distance. Dissimilar metals in galvanic couple that are in close physical contact usually suffer from galvanic corrosion than those that are further apart. The distance effect depends on solution conductivity because the path of current flow is primarily considered.

Effect of geometry. The geometry of the circuit also has an effect on the extent as the current does not readily flow around corner. This is because current takes path that has the least resistance.

2.5.2 Corrosion of Mg and Mg alloys

The corrosion of Mg and its alloys depends on many factors similar to other metals. However, the intense electrochemical activity of Mg makes some factors greatly amplified. In some environments, Mg parts can be severely damaged even galvanic corrosion is avoided by proper design. Unalloyed Mg is not extensively used for structural applications. Thus, the corrosion resistance of Mg alloys is primarily concerned [71]. Two types of Mg alloys are suitable to be used for corrosion application. One is the alloys containing 2-10% Al, combining with minor addition of Zn and Mn. These alloys are widely available at a moderate cost, and have good mechanical properties at temperature ranges 95-120 ^{o}C. The other group consists of Mg

alloys with various additional elements such as rare earth, Zn or Th, all containing a small but effective Zr content that contributes to a fine grain structure. The cause of corrosion failure in Mg and its alloys, as well as the measures available to prevent such failure, are discussed.

Chemical composition. Figure 2.11 shows the effect of various elements on the salt water corrosion performance of Mg binary alloys, with an increase of the content of different elements. Aluminum and manganese are known to have a little if any deleterious effect on the basic salt water corrosion performance of pure Mg, when present at a level exceeding their solubility. Zinc has a mild to moderate accelerating effect on the corrosion rate. Iron, nickel and cobalt have an extremely deleterious effect because of their low solid solubility limits and their ability to serve as cathodic site in water.

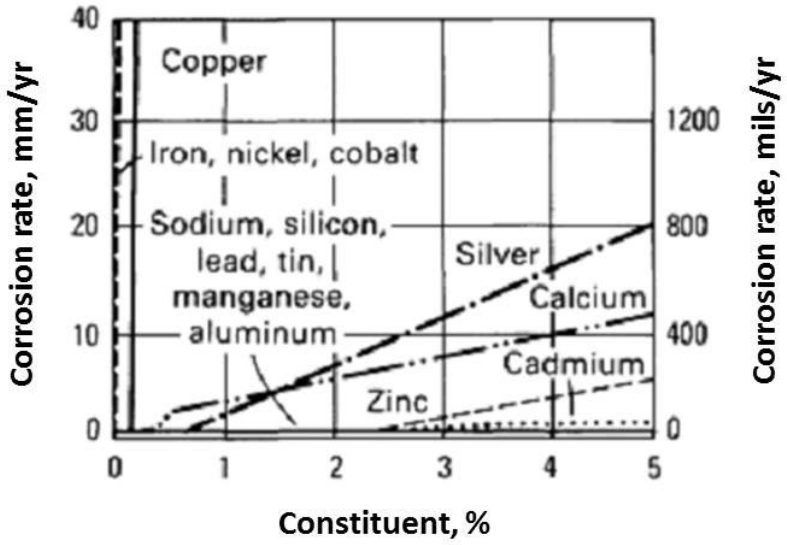

Fig. 2.11 Effect of various alloying elements in Mg on the salt water corrosion performance [72].

Environment factors. In stagnant distilled water at room temperature, Mg alloys rapidly form a protective film that prevents further corrosion. Small amount of salt in water can break down the protective film locally, which usually results in pitting. Dissolved oxygen plays a no major role on the corrosion of Mg in either stagnant fresh water or saline solution. However, agitating or any other means to destroy or inhibit the formation of protective film formation can lead to corrosion. When magnesium is

immersed in stagnant water, its corrosion rate is negligible. Nevertheless, when replenishing the water constantly, the corrosion may increase because solubility limit of $Mg(OH)_2$ can never be reached [73]. The corrosion of Mg by pure water increases substantially with temperature. Severe corrosion may occur in neutral solution of salt of heavy metal such as Cu, Fe or Ni. Chloride solutions are corrosive even at a small amount because it destroys the protective film of Mg. Fluorides form insoluble magnesium fluoride and consequently are not appreciably corrosive. Oxidizing salts, especially those containing chloride and sulfur atom, are more corrosive than non-oxidizing salts.

Magnesium is rapidly attacked by all mineral acids except hydrofluoric (HF and H_2CrO_4). Hydrofluoric does not attack magnesium to an appreciable extent, because it forms an insoluble, protective magnesium fluoride film. However, pitting will develop at a low acid concentration when temperature increases. Pure H_2CrO_4 attacks Mg and its alloys at a very low rate. However, trace of chloride ion in the acid can markedly increase this rate. A boiling solution of 20% H_2CrO_4 in water is widely used to remove a corrosion product from Mg alloys without attacking the base metal [74].

CHAPTER 3: EXPERIMENTAL PROCEDURE

3.1 Introduction

In order to fabricate high strength bonded materials between Ti and Mg alloys with good corrosion resistance, the understanding of the effect of bonding parameters on these properties is necessary. A change in bonding parameters such as time and temperature directly influences the character at the bonding interface, resulting in a change in bonding strength. Moreover, solution-treatment of Mg alloys before bonding with pure Ti can change the characteristics of bonding interface, which then reflects on bonding strength of dissimilar materials. To understand these effects, the bonding surfaces of the parent metals before and after spark plasma sintering (SPS) were observed and the mechanical properties of the bonded materials were evaluated to clarify the underlying bonding mechanism. The mechanism of bonding strength improvement was investigated by examining the fracture surface. In addition to those, the surface potentials were measured from both the bonding interface and the parent metal surfaces so as to study the corrosion behavior of the bonded materials. By observing bonding interface before and after the corrosion test, the galvanic corrosion resistance of each bonded material was evaluated. Both galvanic corrosion resistance and overall corrosion resistance of the bonded materials were further clarified by surface profile observation after corrosion test.

This chapter includes the description of the parent materials used in this research, bonding technique, sample preparation for characterization, metallographic observation on the bonding interface and bonding strength evaluation. The microstructures of the parent metals, the bonding interface characteristics and fracture surface after tensile test were observed. The characterization equipment that were applied in chapter 4 include optical microscope (OM), scanning electron microscope (SEM), energy dispersive spectroscopy, (EDS), transmission electron microscope (TEM), x-ray diffractometer (XRD), Universal tensile test machine and differential thermal analysis (DTA) equipment. The mechanical strength of bonded materials was evaluated by tensile testing. The bonding interface characteristics were related to the bonding strength so as to clarify the

bonding mechanism. For the corrosion behavior analysis of Ti/Mg alloys bonded materials (chapter 5), scanning kelvin probe force microscope (SKPFM) was applied to measure the surface potential difference between two materials at the bonding interface. Furthermore, the surface profile after corrosion test was observed by surface analysis microscope.

3.2 Material characterizations

3.2.1 Parent metals

The materials used in this research are extruded pure Ti, and various types of cast Mg alloys such as AZ31B, AZ61, AZ80 and AZ91. All materials were purchased from Nilaco Co. Ltd. The components of the extruded pure Ti are shown in Table 3.1. For the Mg alloys, the main difference in chemical composition is the Al contents, which are 2.8, 5.5, 7.8 and 8.5 wt% for AZ31B, AZ61, AZ80 and AZ91, respectively. The main compositions of the Mg alloys are listed in Table 3.2.

Table 3.1 Chemical composition of pure Ti used in this research (in wt%).

Material	Ti	H	O	N	Fe
Pure Ti	Bal.	0.013	0.13	0.05	0.3

Table 3.2 Chemical compositions of Mg alloys used in this research (in wt%).

Mg alloys	Mg	Al	Zn	Mn
AZ31B	Bal.	2.8	0.8	0.3
AZ61	Bal.	5.5	0.7	0.3
AZ80	Bal.	7.8	0.3	0.4
AZ91	Bal.	8.5	0.6	0.4

3.2.2 Microstructure observation of parent metals

The microstructures of the parent metals (pure Ti and Mg alloys) were observed before bonding. The surface preparation process is described in this section. The parent metals were cut and then mounted in a resin for grinding. For pure Ti, the surface was ground by sand paper from 240 to 2000# so as to remove the contaminant on the as-received sample surface. The grinding machine used in this research is IM-P2, IMT Co., Ltd. After grinding, the sample was rinsed in ethanol by ultrasonic cleaning machine for 1 min, and further polished by Al_2O_3 colloidal solution in two stages.

Firstly, the Al_2O_3 particle (of 0.3 μm) was used, and secondly the Al_2O_3 particle (of 0.05 μm) was used. Then, the sample was cleaned in ethanol by ultrasonic cleaning machine for 1 min. For microstructure observation, the polished Ti surface was etched by Kroll's etchant (H_2O:HNO_3:HF = 100:5:1) and rinsed thoroughly by running water. For Mg alloys, the surface was ground by sand paper from 400 to 2000#, and cleaned in ethanol by ultrasonic cleaning machine for 1 min. After grinding, Mg alloys surface was polished by diamond paste (diamond particle size of 0.25 μm mixed with lubricant oil) until mirror surface was obtained, and was subsequently rinsed in acetone. For microstructure observation, Mg alloys surfaces were etched by picric acid (Trinitrophenol 0.22 g + Ethanol 10 ml + Acetic acid 0.5 ml + water 10 ml), and subsequently rinsed in ethanol. The microstructure observation of the parent metals was performed by optical microscope (BXS1M, OLYMPUS) and scanning electron microscope (JEOL JSM6500F). The thickness of original oxide film on the surface of the parent metals surfaces was observed by transmission electron microscope (JEOL JEM-2010).

3.2.3 Phase characterization of parent metals

In order to investigate the pre-existing phases in the parent metals, X-ray diffractometer (LAB X XRD-6100 SHIMADZU) was applied in this research. The surfaces of the samples were prepared by grinding with sand paper until 2000# before analysis so as to obtain clear diffraction peaks. The scanning rate was set at 5°/min, and the scanning range was 20° to 80°.

3.2.4 Surface roughness of parent metals

For measuring the surface roughness of the parent metals before bonding, a surface roughness measurement machine (ACCRETECH SURFCOM1400G) was applied in this research. The sample surface was prepared by same method used for microstructure observation but without etching. The surface roughness was measured from three different positions and an average value was calculated.

3.3 Bonding process

3.3.1 Sample preparation

Pure Ti rod with a diameter of 16 mm was cut with a length of 20 mm. For Mg alloys, the cast ingot was machined into a rod shape with a diameter of 16 mm and a length of 20 mm. In order to eliminate the brittle $Mg_{17}Al_{12}$ that is usually found in Mg-Al alloys, Mg alloys were solution treated in muffle furnace (KDF-S70, Denken) at 400 °C for 12 h in air atmosphere, and immediately quenched in water. The Al element was then uniformly diffused along the matrix grain boundaries and all the $Mg_{17}Al_{12}$ particles were eliminated after solution treatment. To modify the surface before bonding, the surface of pure Ti and Mg alloys (with and without solution treated) rods were prepared by same method as that for microstructure observation without etching. After polishing, samples were rinsed in acetone by ultrasonic washing machine for 1 min to degrease and eliminate polishing substance. The samples were immediately kept in vacuum desiccator to prevent excessive oxidation.

3.3.2 Bonding equipment

Spark plasma sintering (SPS) machine (SYNTECH CO. SPS103S) was applied in this research for joining pure Ti to Mg alloys. This machine has many advantages that it can provide high temperature and high pressure simultaneously with a rapid heating rate. The SPS machine works by inputting the pulse DC current which directly passes through the graphite die, as well as the sample. The heat generation is internal, in contrast to the conventional hot pressing, where the heat is provided by external heating. This facilitates a very high heating and cooling rate. Nevertheless, this machine is named as spark plasma sintering, but there is neither spark nor plasma in the process. The heating process occurs just by electrical resistance of materials. Figure 3.1 shows a schematic diagram of the arrangement of the components inside the SPS machine.

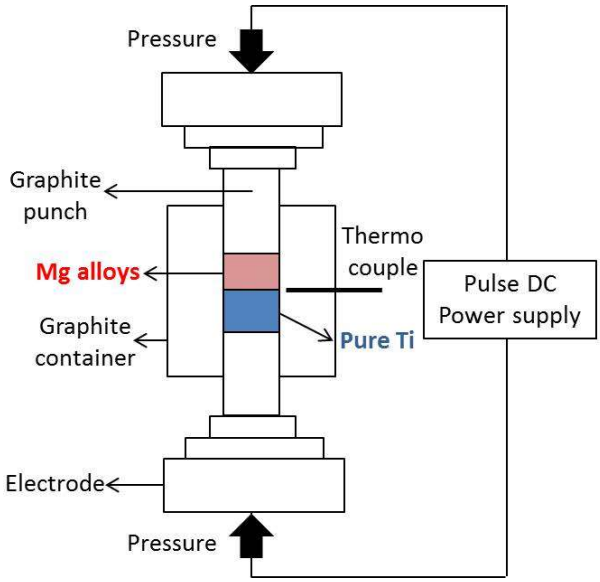

Fig. 3.1 Schematic drawing of components arrangement inside a SPS chamber.

3.3.3 Bonding procedure

In this research, the effect of three bonding parameters on bonding strength were studied, which are the temperature, time and pressure used in the SPS process. The pure Ti and Mg alloys rods with the diameter and height of 16 and 20 mm, respectively, were inserted into a graphite container with its inner diameter and outer diameter of 16 and 56 mm, respectively. The graphite punches were inserted at both ends of the container. The arrangement of the graphite container, graphite punches, thermocouple and samples is shown in Fig. 3.1. For accurate temperature measurement, the distance between the tip of the thermocouple and the samples was designed to be 1 mm. The atmosphere was controlled under a vacuum of 5 Pa during the bonding process. Four bonding temperatures were used in this research, which are 400, 420, 450 and 475 ºC. The bonding time was set for 0.5, 1 and 2 h, while the bonding pressure was set to be 10, 20 and 40 MPa. Different conditions with a various combination of those parameters were applied for bonding so as to study the effect of the parameters on the bonding strength and corrosion behavior of the product. The heating rate was 15 ºC/min for every bonding condition at the temperature rise stage. After bonding, the sample was cooled down in the SPS chamber with a cooling rate of 10 ºC/min. One of the successfully

bonded samples is shown in Fig. 3.2.

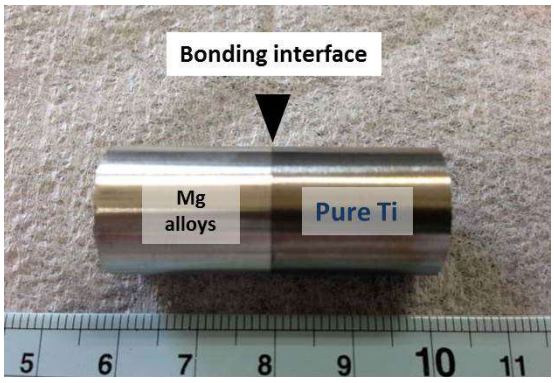

Fig. 3.2 One of the successfully bonded samples between pure Ti and Mg alloys by SPS.

3.4 Bond evaluation

3.4.1 Bonding interface observation

The bonded samples were cut in a perpendicular direction to the bonding interface and mounted in a resin to observe the microstructure. The samples were ground by sand paper from 400 to 2000#, and then polished by diamond paste and etched by picric acid. Microstructure at the bonding interface was observed by OM, SEM and TEM. For TEM observation, samples were prepared by using focus ion beam (FIB, HITACHI FB-2000A) where a thickness of less than 100 nm was finally obtained for the sample. SEM-EDS and TEM-EDS were applied to study the diffusion of alloying elements and the formation of reaction layer at the bonding interface.

3.4.2 Bonding strength evaluation

The bonding strength of bonded materials was evaluated by tensile test, which was conducted on a universal testing machine (AUTOGRAPH AGX 50kN, SHIMADZU). For each bonded samples, three tensile specimens were machined with a diameter of 3 mm and a gauge length of 20 mm (Fig. 3.3). One example of the tensile specimens is shown in Fig. 3.4. The tensile test was performed at a constant speed of 0.05 mm/min at room temperature until fracture occurs. The strain of tensile specimen is measured by charge-coupled device (CCD) camera that detects an increase in distance between two stickers which are attached on tensile specimen. The bonding strength

of the samples was then obtained from the stress-strain curves (S-S curves). The fracture surface of the bonded materials was examined by SEM to establish the relationship between the fracture characteristics and the bonding strength. In addition, the remaining debris on the fracture surface of pure Ti was identified using X-ray diffractometer (XRD).

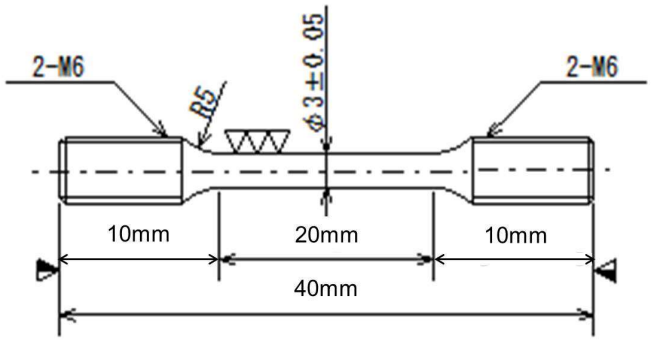

Fig. 3.3 Schematic drawing of tensile testing specimen.

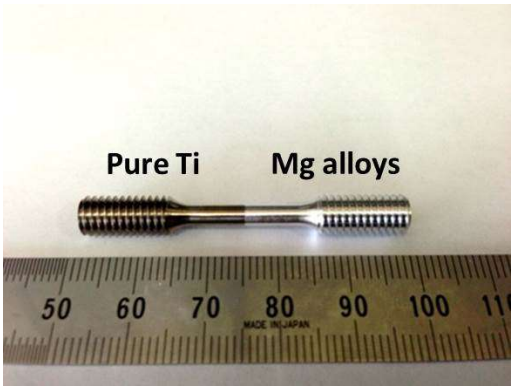

Fig. 3.4 Tensile specimen machined from a bonded sample.

3.4.3 Real-time fracture characteristic

To investigate the real-time failure characteristics of the bonded samples, in-situ tensile tests were performed in SEM chamber. The bonded samples were machined into specific tensile specimens, for which the dimensions are shown in Fig. 3.5 with a thickness of 2 mm. Before testing, the specimen surface was ground by sand paper from 1000 to 2000#, rinsed in ethanol, polished by diamond paste, and then etched by picric acid. The tensile testing equipment was arranged in SEM chamber, and the tests were performed under a high vacuum atmosphere. During the in-situ tensile test,

the loading process was occasionally stopped for a short period, during which the bonding interface was observed. For each test, five interruptions were executed for microstructure observation until the occurrence of failure.

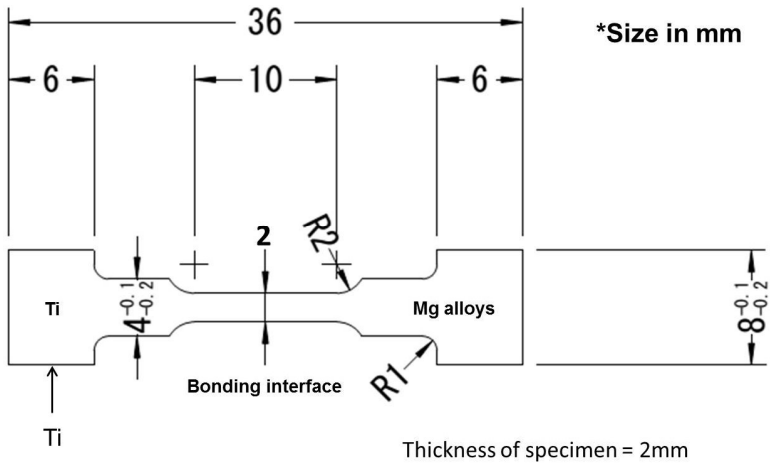

Fig. 3.5 Schematic drawing of an in-situ tensile testing specimen.

3.5 Corrosion behavior of bonded materials

3.5.1 Corrosion test

For the corrosion test, the bonded samples were cut into a size of 8 mm×8 mm×4 mm (width × length × thickness), and all the sample surfaces were polished by the same method used in making the sample for microstructure observation (Fig. 3.6). Two solutions were used in the corrosion test, which are 5 wt% NaCl solution and Kroll's etchant. For 5 wt% NaCl solution, the sample was immersed in the solution for 15 min. The temperature of solution was controlled at 30 ºC, and a magnetic stirrer was used to keep the solution uniform in concentration and temperature throughout the corrosion test. The rotation speed of magnetic stirrer was 170 rpm. The setup of equipment for corrosion test is shown in Fig. 3.7. The weight of the bonded samples before and after corrosion was measured by using a high precision weight measurement apparatus (UW420H, SHIMADZU). The corroded surface was observed by SEM, and the corrosion product was characterized by SEM-EDS. For Kroll's etchant, the samples were immersed in solution at room temperature with no magnetic stirrer for 2 min for microstructure observation. The surface profile at the bonding

interface of the samples immersed in Kroll's etchant was also observed by surface analysis microscope (DSX500, OLYMPUS).

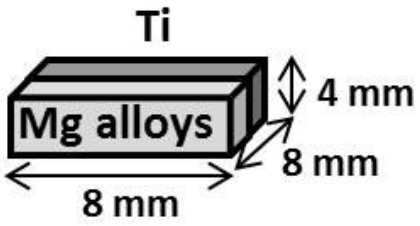

Fig. 3.6 Schematic drawing of a corrosion testing sample.

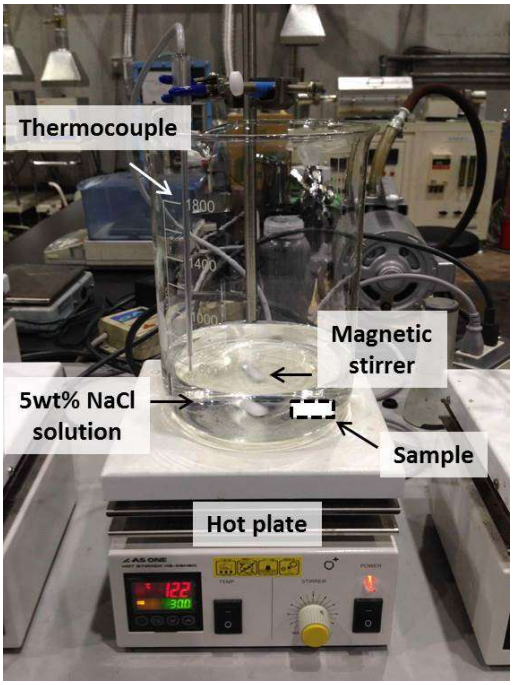

Fig. 3.7 Stirrer equipment for corrosion tests in 5 wt% NaCl solution.

3.5.2 Surface potential measurement

To investigate the corrosion behavior of these dissimilar materials, scanning kelvin probe force microscope (WET-SPM, SHIMADZU) or SKPFM was applied to measure the surface potential difference (SPD) between pure Ti and Mg alloys. Kelvin probe force microscope is a scanning method where potential offset between the probe tip and sample surface can be measured. The cantilever is a reference electrode that forms a capacity with a surface, over which it is scan literally at a constant distance. The cantilever is not

the piezoelectrically driven at its mechanical resonance frequency as that used in conventional atomic force microscopy (AFM), although an alternating current (AC) is applied at this frequency. When there is a direct current (DC) potential difference between the tip and surface, the AC+DC voltage offset will cause vibration in cantilever. The resulting vibration will be detected by scan-probe microscopy (typically involving diode laser and four-quadrant detector). A null circuit is used to drive a DC potential of the tip to a value that minimized the vibration. The map of direct potential versus the lateral position coordinate produces an image of work function at the surface. Figure 3.8 shows a schematic drawing of the SKPFM components.

Before the surface potential measurement, the samples were polished by a similar method used for the microstructure observation preparation. Surface roughness must be controlled as low as possible because a rough surface gives rise to an error surface potential value. The scanning time was set for 3 h with a scanning area of 30×30 μm^2.

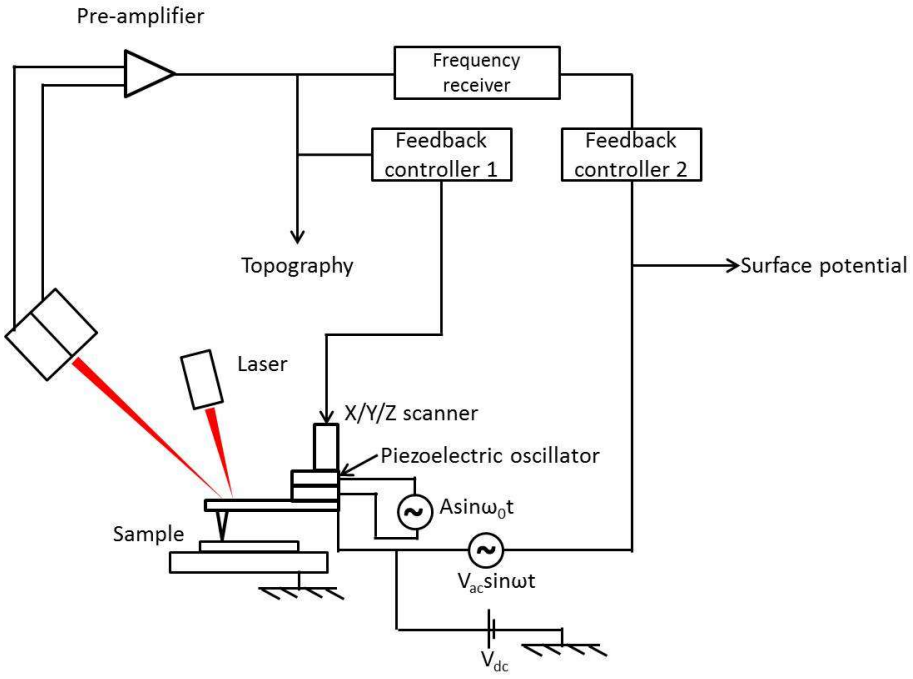

Fig. 3.8 Schematic drawing of components in the scanning kelvin probe force microscope (SKPFM).

CHAPTER 4: BONDING MECHANISM OF DISSIMILAR MATERIALS BETWEEN TITANIUM AND MAGNESIUM ALLOYS

4.1 Introduction

In comparison to researches on bonding Ti or its alloys to other metals such as aluminum [75] or steel [76], researches on bonding Ti or its alloys to Mg alloys are still scarce. Disregard the limited literatures reporting on the topic, there are sporadic papers showing a successful bonding between Ti alloys and Mg alloys. For example, Atieh et al. studied the bonding behavior between Ti-6Al-4V and AZ31-Mg alloys by transient liquid phase (TLP) bonding [77]. Prior to bonding process, Pure Ni was used to coat on Ti-6Al-4V by electro-deposition because Ni coated layer can enhance the metallurgical interface bonding, and results in an improved joint strength. The maximum shear strength of the specimen was found to be 61 MPa when bonded at 520 ºC for 20 min under a bonding pressure of 0.2 MPa. However, the strength decreased when the bonding time was over 20 min due to the increase in volume fraction of the intermetallic phase. On the other hand, an increase of the temperature from 500 to 540 ºC resulted in a change in the bonding mechanism from solid-state to eutectic liquid formation. At temperature above 540 ºC, the dominant joining mechanism became eutectic formation at the Ti-Ni interface. The intermetallic compound that could be detected at the bonding interface was Mg_3AlNi_2 and Mg_2Ni. Applying a pressure during TLP bonding has an advantage that it provides a tight contact and facilitates an interaction or diffusion at the bonding interface. However, applying a bonding pressure more than 0.4 MPa can result in the squeezing of eutectic liquid out of the joint, therefore causing a decrease in the shear strength of bonded materials.

4.2 Characterization of parent metals

The optical microstructure of pure Ti used in this research is shown in Fig. 4.1. It shows only α-Ti matrix and some twins with no other phases, and its average grain size is measured to be 30 μm. Figure 4.2 shows the microstructures of as-cast Mg alloys used in this research, which are AZ31B, AZ61, AZ80 and AZ91. They all show a precipitated $Mg_{17}Al_{12}$ particles on a Mg matrix and the amount of the precipitated gradually increase with the Al content. This phase is usually observed at the Mg grain boundary and its morphology is an irregular plate.

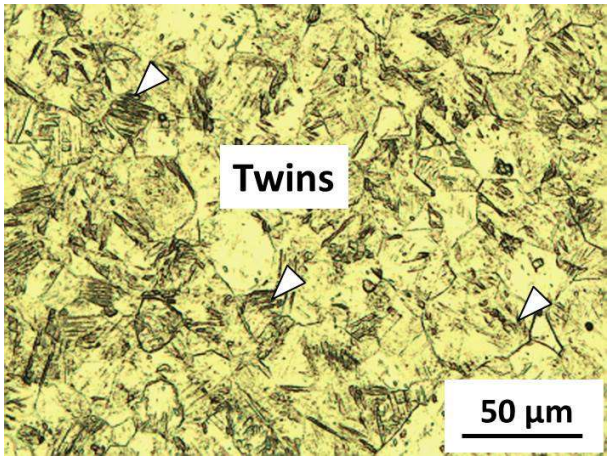

Fig. 4.1 Microstructure of pure Ti observed by an optical microscope.

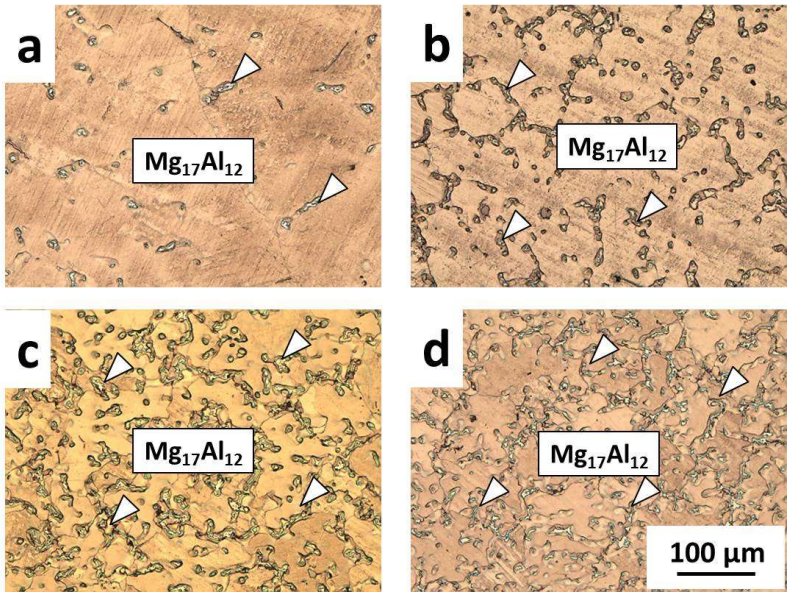

Fig. 4.2 Microstructures of Mg alloys observed by an optical microscope a) AZ31B, b) AZ61, c) AZ80, and d) AZ91.

SEM-EDS analysis was performed to investigate the precipitated phase, where the results are shown in Fig. 4.3. Mapping images show a higher Al content at the precipitated phase comparing to the matrix. The attached table shows the values of Mg and Al contents for the marked four points and chemical formula of the precipitated phase can be simply calculated. This formula corresponds to $Mg_{17}Al_{12}$ which is usually found in Mg-Al alloys. Al_6Mn precipitated phase was also detected in Mg alloys but its amount was rather low compared to that of $Mg_{17}Al_{12}$ [78]. The surfaces of Ti and Mg alloys were polished until a mirror surface was obtained, and the roughness of polished surfaces was measured by a surface roughness measurement machine. Table 4.1 shows an average roughness (R_a) of each parent metal, it can be seen that all polished surfaces were very smooth (R_a < 0.2 µm) that assured a perfect contact between pure Ti and Mg alloy surface during the solid state bonding process.

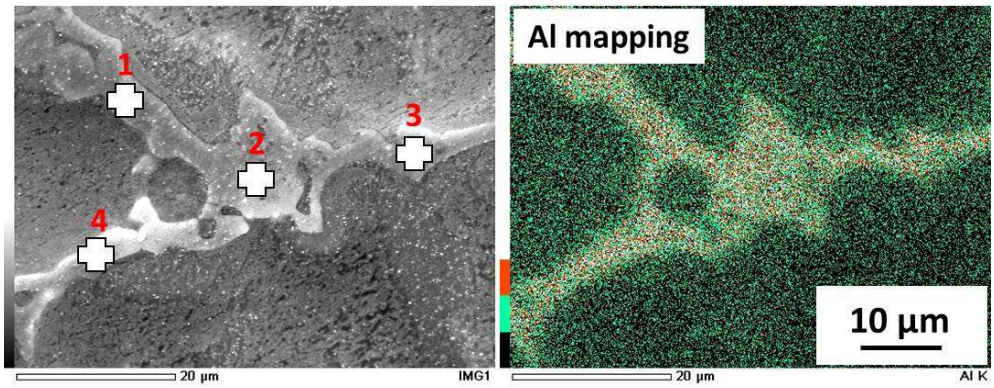

Point	Mg(%)	Al(%)	Chemical formulae
1	62.17	37.83	$Mg_{17}Al_{10.3}$
2	63.62	36.28	$Mg_{17}Al_{9.7}$
3	67.97	32.03	$Mg_{17}Al_{8.0}$
4	65.34	34.36	$Mg_{17}Al_{8.9}$

Fig. 4.3 SEM-EDS analysis on precipitated phases with attached table of Mg and Al contents.

Table 4.1 Average surface roughness (R_a) of each parent metal.

Roughness (R_a) / Material	Test 1 (µm)	Test 2 (µm)	Test 3 (µm)	Average (µm)
Pure Ti	0.11	0.14	0.14	0.13
AZ31B	0.12	0.15	0.14	0.14
AZ61	0.10	0.12	0.12	0.11
AZ80	0.17	0.18	0.15	0.17
AZ91	0.19	0.17	0.14	0.17

The initial surface of pure Ti and Mg alloys was observed by TEM, and it shows an existence of original oxide film on both surfaces with a thickness of about 15 nm (Fig. 4.4). It is commonly known that fresh surface of pure Ti and Mg alloys are very active to oxygen in the air, so the oxide layer with a thickness of 15-25 nm is usually found on their surfaces [79]. Some researchers have reported that the oxide layer had a disadvantage effect on solid state bonding process because it is brittle and inhibited the metallurgical reaction at the bonding interface [80].

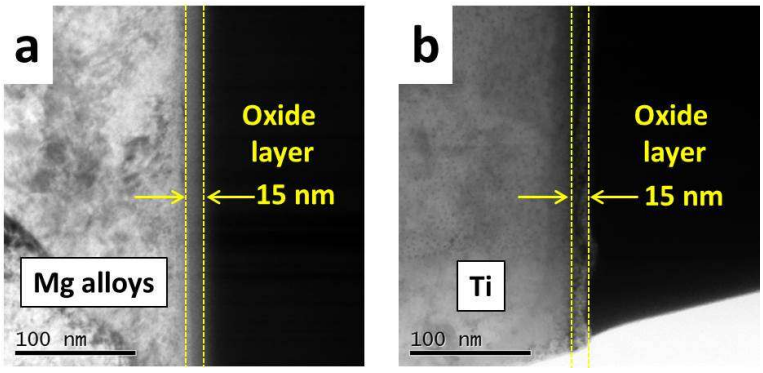

Fig. 4.4 TEM observation of initial surfaces of parent metals a) Mg alloys and b) Pure Ti.

4.3 Bonding between pure Ti and non-solution treated Mg alloys

4.3.1 Microstructure observation of bonding interface

The bonding interface between pure Ti and various Mg alloys bonded at 400 °C for 1 h is observed by optical microscope, where the results are shown in Fig. 4.5. From a macroscopic view of the structure, a fine bonding interface without crack and void was obtained through solid state bonding. The small amount of $Mg_{17}Al_{12}$ particles in AZ31B matrix were transformed to a plate shape $Mg_{17}Al_{12}$ (TR $Mg_{17}Al_{12}$) after SPS. The transformed $Mg_{17}Al_{12}$ was a re-precipitated $Mg_{17}Al_{12}$ formed during cooling stage in SPS chamber (Fig 4.6a). For Mg alloys containing higher Al content than AZ31B such as AZ61, AZ80 and AZ91, a TR $Mg_{17}Al_{12}$ was observed remaining in the matrix, as shown in Figs. 4.5b-4.5d. The remained $Mg_{17}Al_{12}$ is a non-dissolved $Mg_{17}Al_{12}$ particle that was usually found in AZ80 and AZ91 and remains after solution treatment. A large amount of such $Mg_{17}Al_{12}$ can be observed in original AZ80 and AZ91 matrix (Fig. 4.6b). SEM observation shows that neither micro crack nor void was found at the bonding interface. This is due to the application of the applied pressure of 40 MPa, causing a plastic deformation of the Mg alloys. This resulted in perfect contact between Ti and Mg alloys. However, an interaction layer or intermetallic compound could not be observed at the interface by SEM.

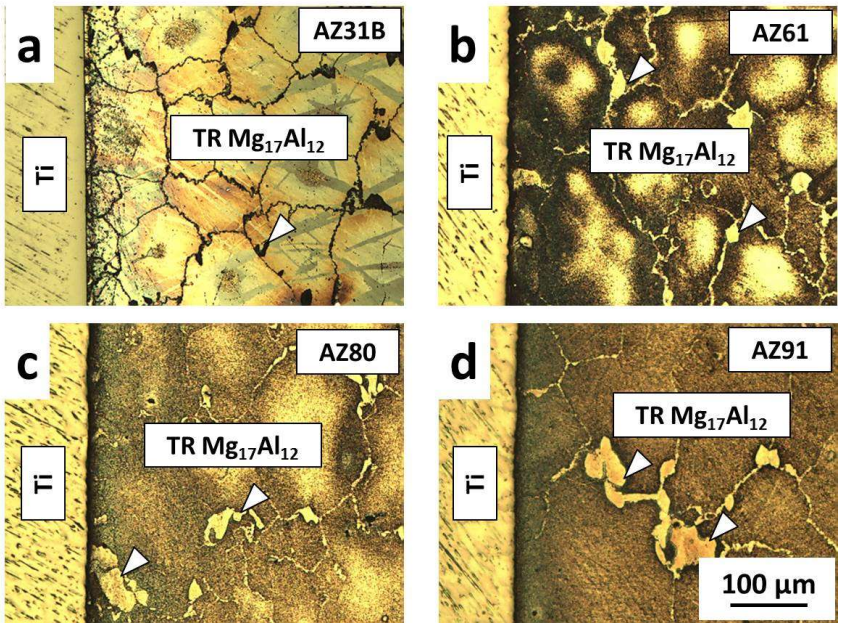

Fig. 4.5 Optical images observed on the bonding interface of a) Ti/AZ31B, b) Ti/AZ61, c) Ti/AZ80, and d) Ti/AZ91 bonded at 400 ºC for 1 h.

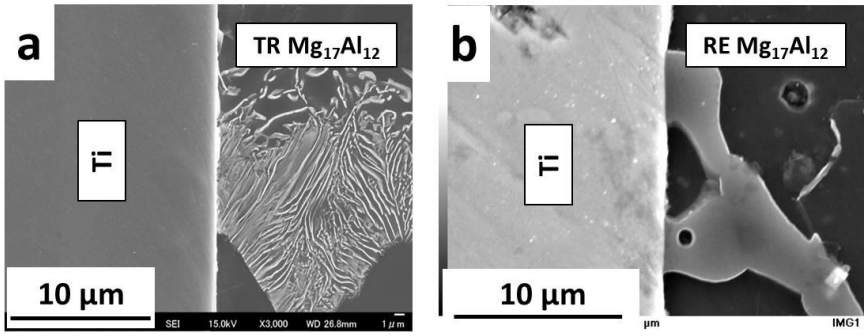

Fig. 4.6 SEM images of bonding interfaces of pure Ti and Mg alloys a) Transformed $Mg_{17}Al_{12}$ (TR $Mg_{17}Al_{12}$) and b) Remained $Mg_{17}Al_{12}$ (RE $Mg_{17}Al_{12}$).

Figure 4.7 shows SEM-EDS analysis results at the bonding interface of Ti/AZ80 dissimilar materials bonded at 400 ºC for 1 h, no diffusion of any elements was observed after SEM-EDS scanning. This is explained by a thickness of interaction layer that may be measurable in a nano-scale, but could not be detected by SEM-EDS. Point analysis of each element across the bonding interface was also performed by SEM-EDS as shown in Fig. 4.8. The concentration of Ti or Mg was found rich only on their sides, and their

concentration was suddenly decreased when crossing to the other side. Therefore no concentrated area of these two elements was found. This corresponds to a binary phase diagram of Ti-Mg that no intermetallic compound could be formed between these two elements at any temperature or composition [16]. On the other hand, Al concentrated area of 7.53 wt% was detected at the bonding interface. This value was higher compared to a further right side which Al content was measured to be approximately 5 wt%. This result confirms an existence of intermetallic compound or Al segregated layer at the bonding interface although it was not detected by means of EDS mapping. The similar results were also obtained from other bonded materials with a different in a Al content on a Mg alloys side.

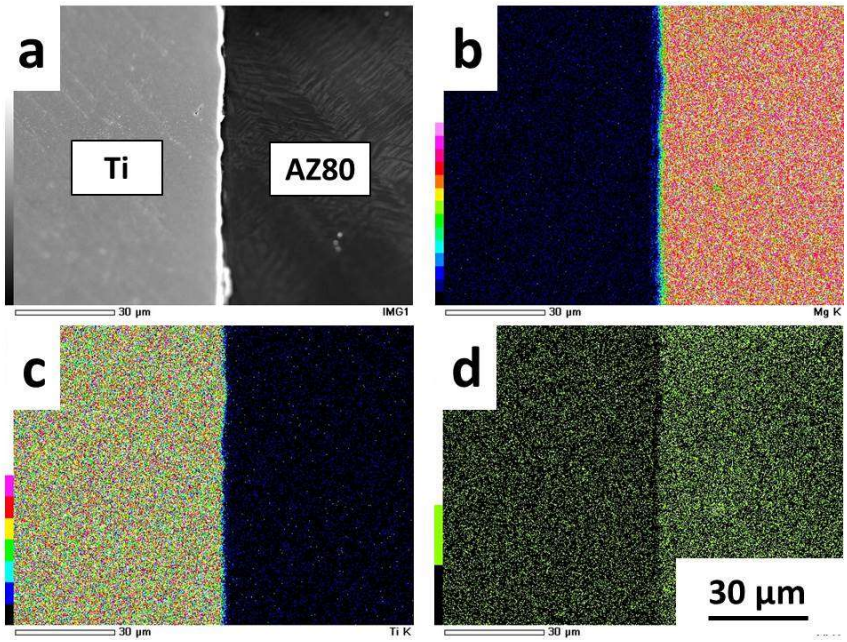

Fig. 4.7 SEM-EDS scanning images at the bonding interface of Ti/AZ80 bonded materials. a) SE image, b) Mg mapping, c) Ti mapping, and d) Al mapping.

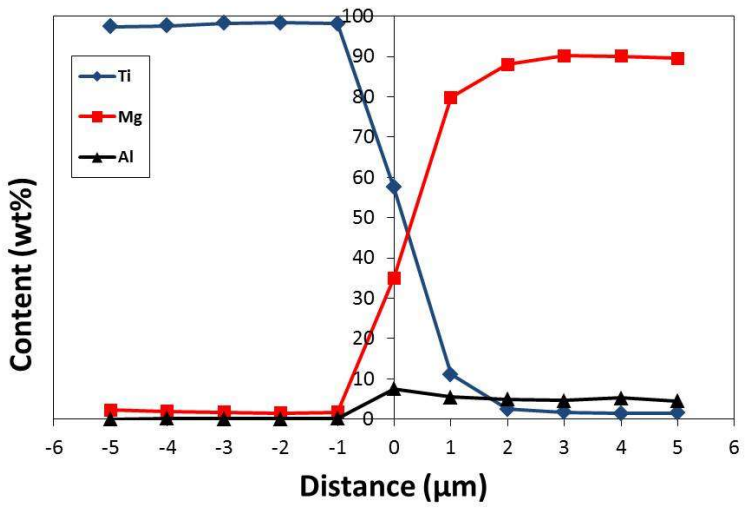

Fig. 4.8 Distribution of Ti, Mg and Al in the distance of 5 μm away from the bonding interface of Ti/AZ61 bonded at 400 ºC for 1 h.

According to no useful information regarding diffusion or interaction at the bonding interface that could be obtained by SEM, TEM observation was then performed. Figure 4.9 shows the microstructures at the bonding interface of each bonded material bonding at 400 ºC for 1 h. The oxide film which could be observed on initial surface of Ti and Mg alloys before bonding (Fig. 4.4) disappeared after solid state bonding. This can be explained by the highly applied pressure of 40 MPa during SPS. Mg alloys were plastically deformed on the Ti surface, and the oxide film on both Ti and Mg alloy surface was destroyed [81]. Figure 4.9a shows the bonding interface between pure Ti and AZ31B, which was clearly observed by TEM. Titanium side appeared darker in the TEM image than Mg alloy side since Ti had a higher atomic weight than Mg or Ti film is thicker than that of Mg alloy film resulted in smaller transmitted electron amounts [82]. The intermetallic compound layer was not observed in these bonded materials due to the low bonding temperature and the low Al content in AZ31B. The bonding interfaces between pure Ti and AZ61 shows a similar characteristic to that between pure Ti and AZ31B. Although AZ61 has a higher Al content than AZ31B, an intermetallic compound layer still could not be observed. This could be explained by a much higher Al content in $Mg_{17}Al_{12}$ particle compared to Al content in a matrix of AZ61 which was much lower than 6 wt%. Therefore, an intermetallic layer can still be difficult to form for

bonding between pure Ti with either AZ31B or AZ61. On the other hand, thin interaction layer of Ti_3Al (encircled by red line) was observed in Ti/AZ80 and Ti/AZ91 bonded materials, as shown in Figs. 4.9c and 4.9d, respectively. The diffraction pattern obtained from the area surrounded by a red broken line (Inset figure in Fig. 4.9d) indicates Ti_3Al grain formation. This implies that Al content in the matrix of AZ80 and AZ91 was sufficiently high to form a Ti_3Al layer at the bonding interface.

Not only by the diffraction pattern, but also by a dark field image the Ti_3Al intermetallic layer was confirmed (Fig. 4.10). The dark field image (DF) only shows bright area where the scattered electrons beams are used to form an image. Thus, by specific selection of the beam, the intermetallic layer can be shown in bright while the matrix in dark [83].

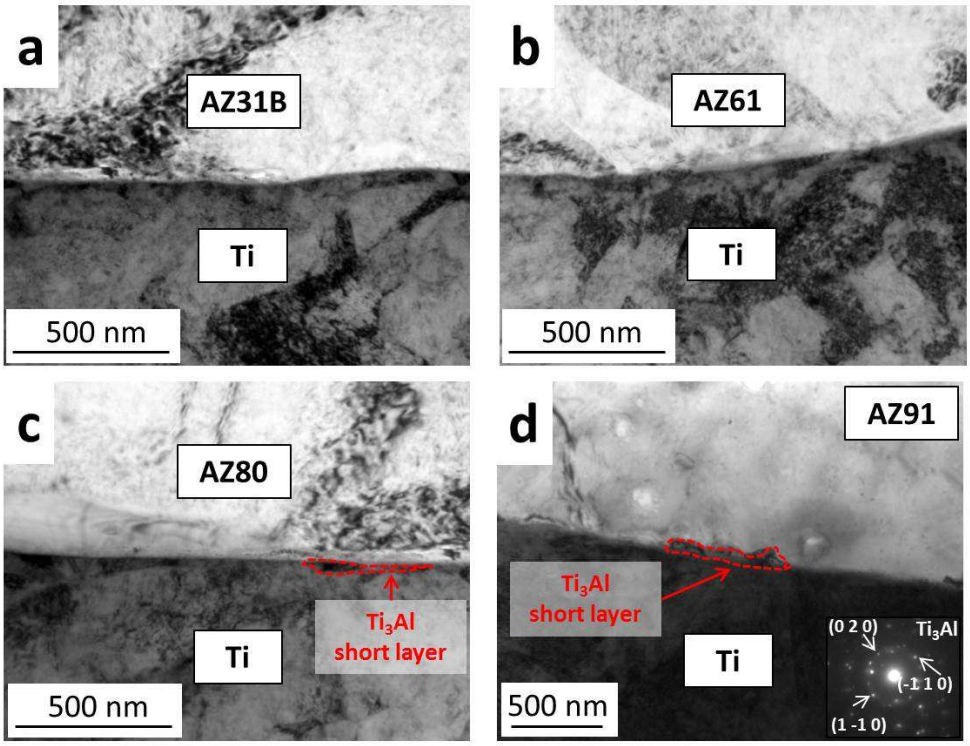

Fig. 4.9 Bonding interfaces of dissimilar materials bonded at 400 ºC for 1 h a) Ti/AZ31B, b) Ti/AZ61, c) Ti/AZ80 and d) Ti/AZ91.

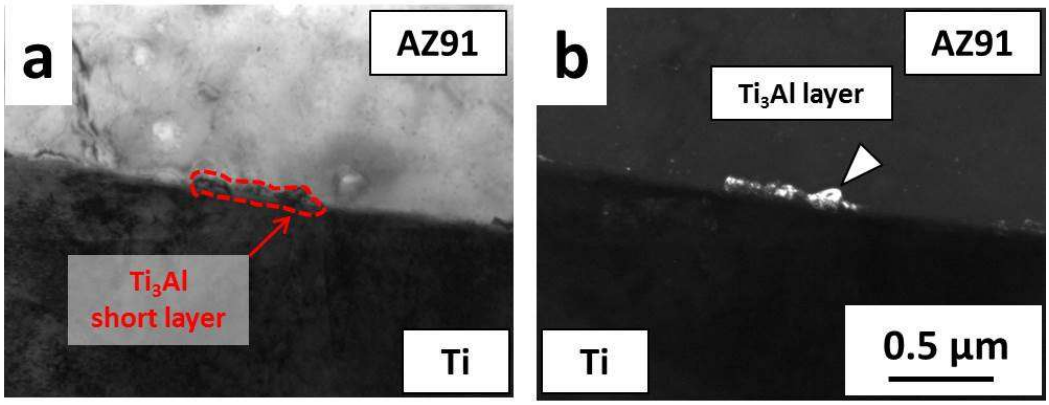

Fig. 4.10 Intermetallic layer at the bonding interface of Ti/AZ91 bonded at 400 ºC for 1 h a) Bright field (BF) image and b) Dark field (DF) image.

Due to the effect of applied pressure, dislocation piled-up areas can be easily observed near the bonding interface in Mg matrix (Fig. 4.11). Fig. 4.11a-1 to 4.11a-3 show the dislocation piled-ups in Mg matrix near the bonding interface from three different areas. The dislocation piled-up in Mg matrix was formed in a network colony pattern. These areas possessed a high stress concentration induced by the bonding pressure [84]. These results confirmed that plastic deformation on Mg alloy side gave rise to a perfect contact between the two materials by creating a new contact surface which oxide film is removed. Fig. 4.11b-1 to 4.11b-3 show the interference fringes inside $Mg_{17}Al_{12}$ particle near the bonding interface from three different areas. These interference fringes are appear by the deformation of TEM sample when it is placed on the sample holder because of a TEM sample is very thin as a film. The dislocations piled-up will not be formed in $Mg_{17}Al_{12}$ particles as they are formed in Mg matrix because of these IMC particles cannot deform under an applied pressure.

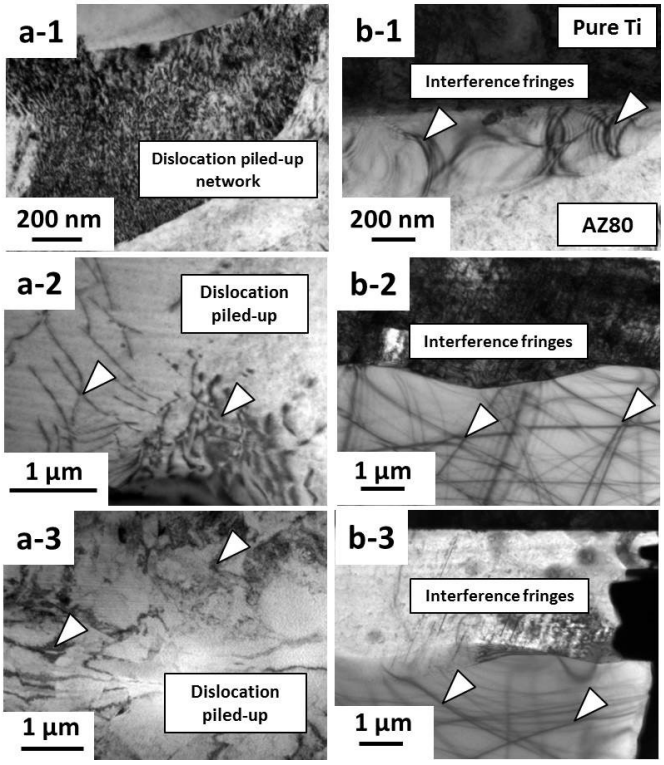

Fig. 4.11 Dislocation piled-up (a-1 to a-3) in Mg alloys matrix and interference fringes inside $Mg_{17}Al_{12}$ particle (b-1 to b-3) near the bonding interface of Ti/AZ80 material bonded at 400 ºC for 1 h.

Figure 4.12 shows a mapping of Al and O elements at the bonding interface of Ti/AZ31B and Ti/AZ91 bonded materials bonded at 400 ºC for 1 h. For Ti/AZ31B, a diffusion layer of Al with a thickness of 25 nm was observed without an existence of Ti_3Al layer which confirmed by a dark field image. The oxygen mapping image shows no oxygen concentrated layer, implying that the original oxide layer on both bonding surfaces were destroyed during SPS (Fig. 4.11a). Figure 4.12b shows the bonding interface for the Ti/AZ91 bonded material, an Al diffusion layer with a thickness of 40 nm was detected by TEM-EDS. The thickness of diffusion layer observed at the interface of Ti/AZ91 was thicker and more uniform compared to the Ti/AZ31B bonded material. This can be explained by the higher Al content in AZ91 than in AZ31B, which are 8.33 and 2.56 wt%, respectively. The RE $Mg_{17}Al_{12}$ particles were also detected near the bonding interface of Ti/AZ91 and they exhibited high Al content in the TEM-EDS mapping image. Similar to Ti/AZ31B, a mapping image of oxygen at the bonding interface of

Ti/AZ91 shows no oxygen concentrated layer. From this result, it is confirmed that the original oxide layer on the parent metals surfaces was completely destroyed during SPS, and it play no effect in the bonding strength of Ti/Mg alloy bonded materials.

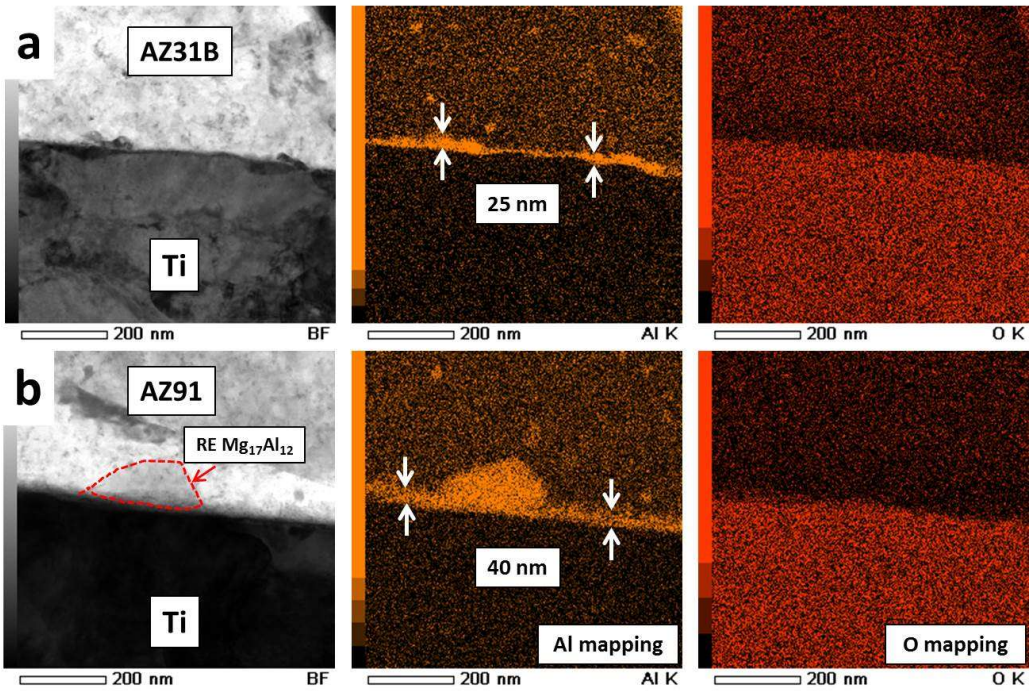

Fig 4.12 TEM-EDS mapping analysis of Al and O element of a) Ti/AZ31B and b) Ti/AZ91 bonded at 400 ºC for 1 h.

4.3.2 Bonding strength of Ti/Mg alloys bonded materials

The in-situ tensile test of Ti/Mg alloy dissimilar materials was performed in SEM chamber to investigate the failure characteristics at the bonding interface. Fig. 4.13 shows a load-displacement profile of the Ti/AZ80 specimen bonded at 400 ºC for 1 h at 40 MPa under a tensile test in SEM. The tensile load was applied to the specimen in 5 steps where it reached 50, 90, 130, 170 and 185 N, respectively. The load was stopped in each step and microstructure observation was performed at the bonding interface including after failure. The tensile load reached 195 N before the specimen failed.

The microstructures at the bonding interface of the Ti/AZ80 bonded material observed in each step of the in-situ tensile test are shown in Fig. 4.14. At the start position, there are two types of contact area: Ti/Mg matrix

and Ti/TR $Mg_{17}Al_{12}$. The Mg matrix around TR $Mg_{17}Al_{12}$ contains a higher Al content compared to other areas (Fig. 4.25). Figure 4.14b shows a microstructure at the bonding interface after applying a tensile load of 90 N. However, this stage shows no change in the microstructure compared to that at the starting position. After a tensile load at 170 N, there are still no changes in the microstructure of Ti and Mg alloy, and neither cracks nor damage were observed at the bonding interface. However, the bonded specimen cracked suddenly at the bonding interface when the tensile load reached 195 N. Both smooth and rough surfaces were observed at the fracture surface, where these surfaces were located at Mg matrix and TR $Mg_{17}Al_{12}$, respectively. The high magnification image at area (a) in Fig 4.14d is shown in Fig. 4.14f, where an elongated Mg matrix near TR $Mg_{17}Al_{12}$ was observed. This area exhibited good bonding characteristics between pure Ti and a Mg alloy. This result implies that the Mg matrix which contained high Al content show a good potential in bonding to pure Ti. The TR $Mg_{17}Al_{12}$ shows a brittle fracture characteristic as observed in Fig. 4.14f that this phase should be eliminated before bonding.

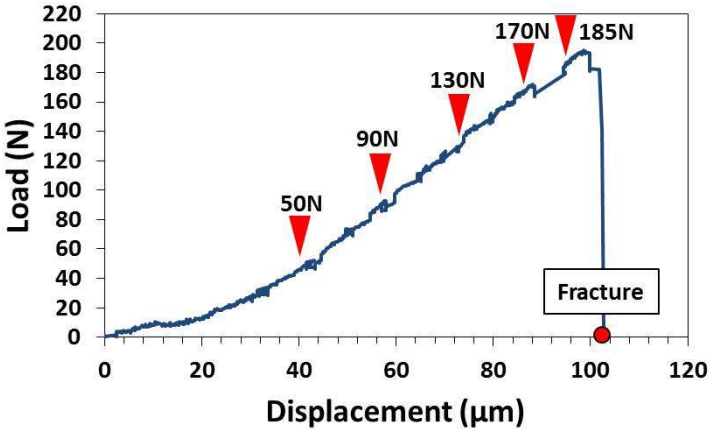

Fig. 4.13 Load-displacement profile of Ti/AZ80 bonded at 400 ºC for 1 h obtained from in-situ tensile test.

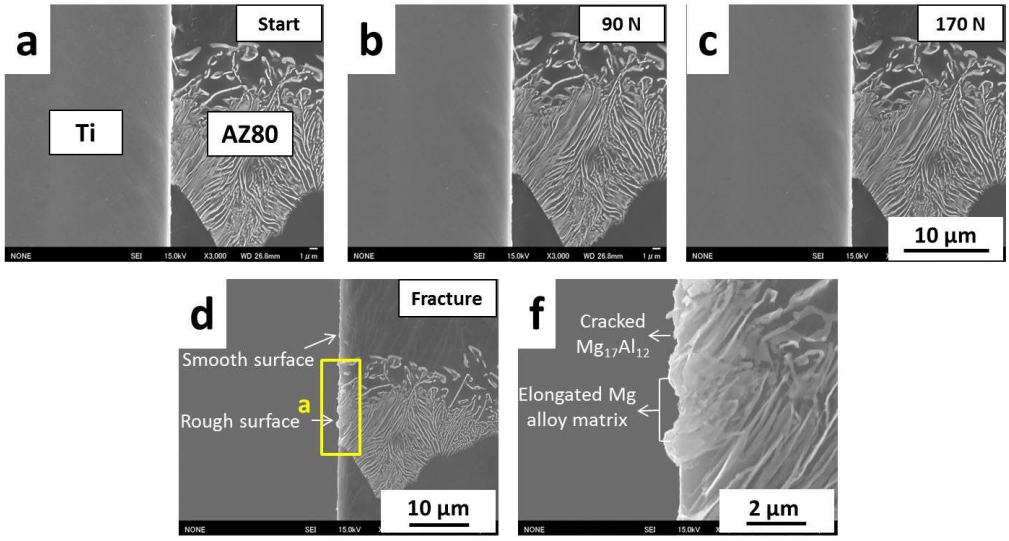

Fig. 4.14 Microstructures at the bonding interface of Ti/AZ80 bonded at 400 ºC for 1 h during in-situ tensile test when tensile load increased to a) 0 N, b) 90 N, c) 170 N, d) After failure and f) High magnification image of area in Fig. d.

Figure 4.15 shows stress-strain curves for the Ti/Mg alloys dissimilar materials bonded at 400 ºC for 1 h. Bonding pure Ti to low Al content Mg alloys such as AZ31B and AZ61 shows an inferior bonding strength compared to pure Ti bonded to AZ80 or AZ91. This result suggested that Al was an important element to bonding between pure Ti and Mg alloys, because high Al content area exhibited a good potential for bonding to pure Ti. From the microstructures at the bonding interface of Ti/AZ80 and Ti/AZ91 (Fig. 4.9c and 4.9d), the short intermetallic layers of Ti_3Al were observed. This suggested that an improvement of tensile strength due to the formation of the intermetallic layer [85]. Bonding between pure Ti and pure Mg was also performed at 400 ºC for 1 h with an applied pressure of 40 MPa. However, tensile test could not be performed, because the bonded specimens failed during machining (Fig. 4.16). This result confirmed an important role of the Al alloying element on solid state bonding between pure Ti and Mg alloys.

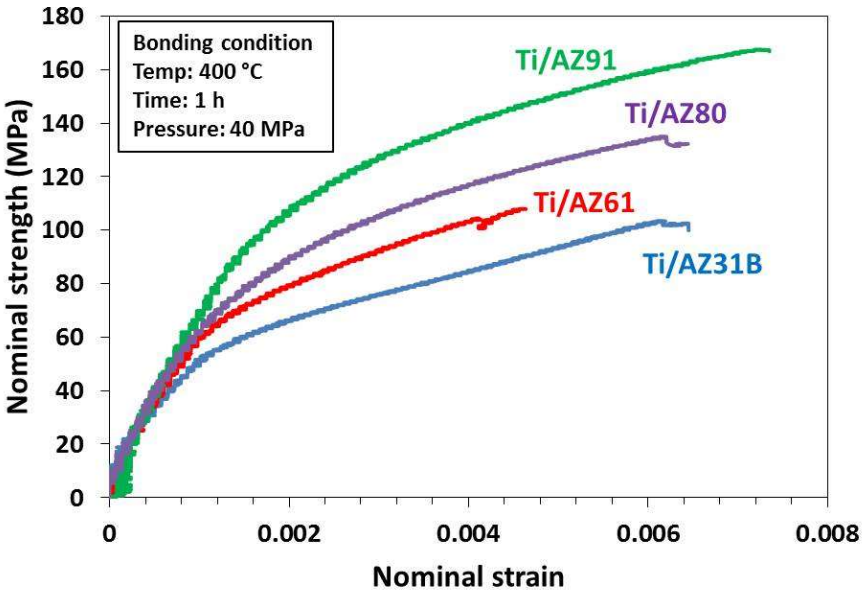

Fig. 4.15 Stress-strain curves of Ti/Mg alloy materials bonded at 400 ºC for 1 h under an applied pressure of 40 MPa.

The tensile properties of the parent metals (pure Ti and Mg alloys), and the materials bonded at 400 ºC for 1 h under an applied pressure of 40 MPa are listed in Table 4.2. Tensile properties of the bonded materials were obtained as an averaged value of three specimens. The fracture always occurs at the bonding interface under a tensile test.

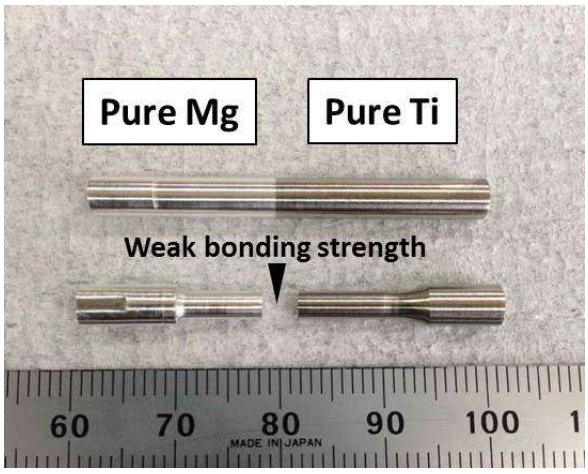

Fig. 4.16 Failure of pure Ti/pure Mg bonded specimen during machining.

Table 4.2 Average tensile properties of parent metals (pure Ti and Mg alloys), and Ti/Mg alloys dissimilar materials bonded at 400 ºC for 1 h obtained from three specimens.

Material	0.2%YS (MPa)	UTS (MPa)	Elongation (%)
Pure Ti	355 (361/349)	398 (402/394)	22.0 (23.0/21.0)
AZ31B	55 (61/50)	163 (165/162)	6.2(6.5/5.6)
AZ61	84 (87/81)	170(176/165)	3.5 (3.6/3.4)
AZ80	109 (115/101)	183 (194/165)	3.1 (3.2/2.9)
AZ91	126 (128/122)	177 (184/163)	1.6 (2.0/1.0)
Ti/AZ31B	84 (91/77)	102 (127/76)	0.6 (0.7/0.5)
Ti/AZ61	88 (98/79)	115 (141/123)	0.4 (0.5/0.3)
Ti/AZ80	125 (131/117)	160(169/154)	0.7 (0.7/0.7)
Ti/AZ91	120 (125/115)	140(149/133)	0.7 (0.8/0.6)

Note: (maximum value/minimum value)

The yield strength of each bonded specimen was rather similar to the yield strength of the Mg alloy. The ultimate tensile strength (UTS) of pure Ti was about two times that of the parent Mg alloys. Although there is a large difference in tensile properties and others between pure Ti and Mg alloys, it is proved that these two materials can be successfully bonded with satisfying tensile strengths. Ti/AZ31B and Ti/AZ61 exhibited UTS of 101.8 and 115.1 MPa, respectively, which are much lower than their parent metal. On the other hand, the bonded material between pure Ti and high Al content Mg alloys such as AZ80 or AZ91 exhibited superior UTS or bonding strength. The UTS or bonding strength obtained from the tensile test can be a strong evidence to emphasize the importance of Al element in improving the bonding strength between pure Ti and Mg alloys. The elongation of bonded materials was very low compared to that of their parent metals and it increases with a bonding strength. The bonded specimens were found to be elongated only on Mg alloys side, and tensile load seems to be concentrated at the bonding interface because different materials with different mechanical properties are joined together at this area [86]. This causes a low ductility of the bonded interfaces.

Figure 4.17 shows bonding efficiency of Ti/Mg alloy specimens bonded at 400 ºC for 1 h, which could be simply calculated by eq. 1 [87]. Bonding efficiency shows large improvement when 2.8 wt% of Al is added in Mg. It increases gradually in a linear relationship when the Al content in

Mg alloys increases from 2.8 wt% to 8.5 wt%. The highest bonding efficiency was obtained to be 87.5% for Ti/AZ80. Ti/AZ91 also shows high bonding efficiency with a value of 80.0%, noticing that a thin intermetallic layer of Ti_3Al was observed at the bonding interface of these bonded materials as shown in Fig 4.9.

$$\text{Bonding efficiency} = \frac{\sigma_b}{\sigma_p} \times 100 \qquad \text{eq. 1}$$

Where, σ_b = Bonding strength of bonded materials (MPa)

σ_p = Tensile strength of parent Mg alloys (MPa)

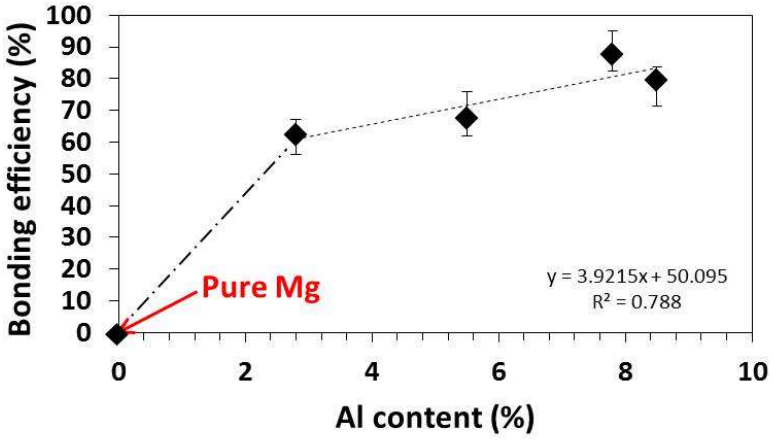

Fig. 4.17 Bonding efficiency depending on Al content in Ti/Mg alloy materials bonded at 400 ºC for 1 h under an applied pressure of 40 MPa.

4.3.3 Fracture surface of pure Ti and Mg alloys bonded materials

Figure 4.18 shows the SEM images of the fracture surfaces on the Mg alloys side of the Ti/Mg alloys specimens bonded at 400 ºC for 1 h. For Ti/AZ31B and Ti/AZ61 that show a low bonding efficiency, most of the areas on the fracture surface are smooth, and fracture features can only be found in sporadic areas. On the other hand, more obvious fracture features can be found on the surfaces of Ti/AZ80 and Ti/AZ91. The fracture characteristics are well corresponding to the bonding strength and bonding efficiency, in which a high bonding strength and efficiency result in a severe damage on the fracture surface [88].

Figure 4.19 shows the fracture surfaces on the pure Ti side of Ti/AZ80 bonded specimens. A large amount of AZ80 debris can be observed on the Ti

surface, where some of them show evidences that the AZ80 surface was deformed on the Ti surface. The Ti surface was smooth after failure, and none of damages was observed. The high magnification image from the smooth area on the fracture surface of Ti shows a large amount of small AZ80 particles spreading throughout this area. Similar particles are also observed on the smooth fracture on Ti side of Ti/AZ31B and Ti/AZ61 with a similar density. This indicates that a bonding between pure Ti and Mg alloys occurred throughout the bonding surface, and large debris of Mg alloy on the fracture surface of pure Ti represents an excellent bonding area, where the bonding strength can even exceed the strength of the parent Mg alloys [89]. The large debris was mostly observed on the fracture surface of pure Ti that bonded to AZ80 or AZ91.

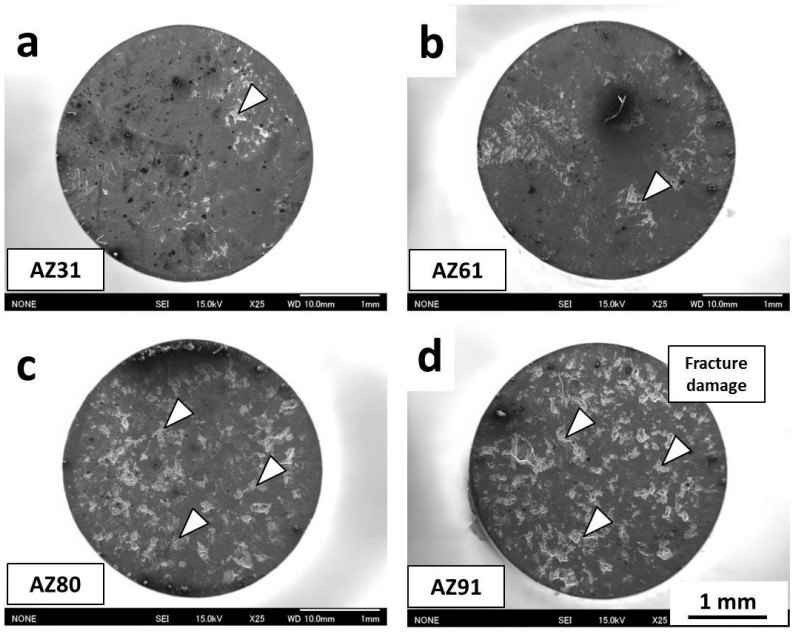

Fig. 4.18 Fracture surface observation on Mg alloys side of bonded materials bonded at 400 ºC for 1 h under an applied pressure of 40 MPa a) Ti/AZ31B, b) Ti/AZ61, c) Ti/AZ80, and d) Ti/AZ91.

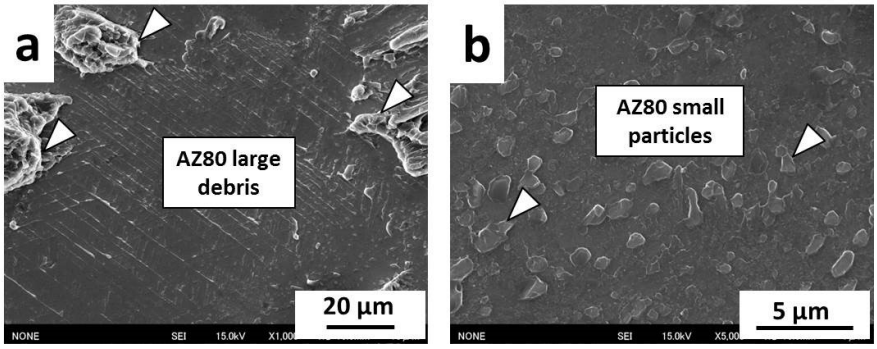

Fig. 4.19 Fracture surfaces of Ti/AZ80 bonded at 400 °C for 1 h observed on Ti side a) Large AZ80 debris and b) AZ80 particles on smooth fracture area.

4.3.4 Effect of bonding time on bonding strength

To study the effect of bonding time on bonding strength of Ti/Mg alloy bonded materials, pure Ti and Mg alloys was bonded for 1 and 2 h, respectively. Figure 4.20 shows the effect of Al content and bonding time on the bonding strength of Ti/Mg alloy dissimilar materials. The bonding strengths of the specimens bonded for 1 and 2 h gradually increase with the Al content in Mg alloys. These results indicate that the higher Al content leads an increase in the thickness of Al diffusion layer and the formation of thin intermetallic layer of Ti_3Al (Fig. 4.9 and 4.12). The bonding strengths of Ti/AZ31B and Ti/AZ61 fabricated by using bonding time of 2 h are similar to those bonded for 1 h at the same bonding temperature and pressure. This can be explained by the similar microstructure from the bonding interface, where the samples bonded for 2 h show similar characteristics to the samples bonded for 1 h with the same thickness of Al diffusion layer (Fig. 4.12a). Bonding strengths of Ti/AZ80 and Ti/AZ91 produced under these two conditions show a very small difference. This may be affected by the different surface condition such as the amount of $Mg_{17}Al_{12}$ particle and distribution of Al element in the bonding surface. From these results, it can be concluded that increasing the bonding time from 1 to 2 h did not significantly improved the bonding strength of the dissimilar materials.

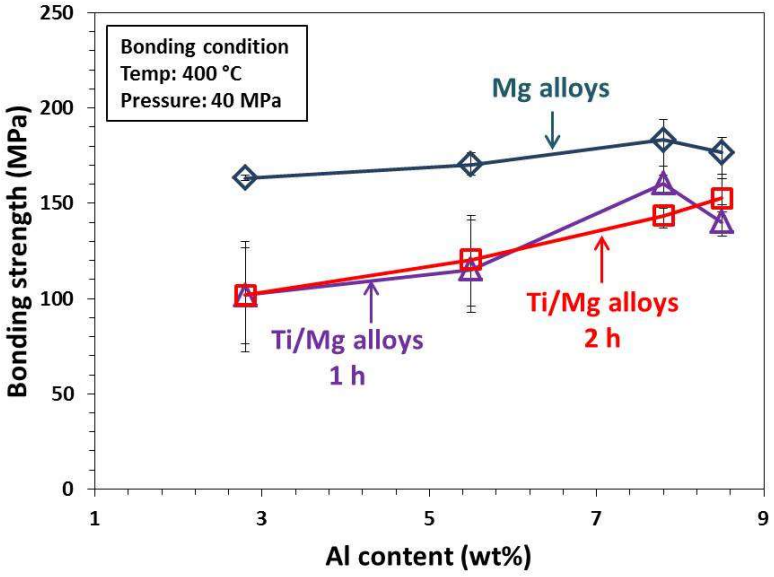

Fig. 4.20 Effect of Al content and bonding time on bonding strength of Ti/Mg alloy dissimilar materials bonded at 400 ºC under an applied pressure of 40 MPa.

Figure 4.21 shows the bonding efficiency of Ti/Mg alloy bonded materials bonded at 400 ºC under an applied pressure of 40 MPa for 1 and 2 h. The bonding strength of Ti/Mg alloy bonded for 2 h is similar to that bonded for 1 h, Ti/AZ31B and Ti/AZ61 exhibited very poor bonding efficiency compared to Ti/AZ80 and Ti/AZ91. The highest bonding efficiency was obtained for Ti/AZ80 to be 87.5%, which is similar to the bonding efficiency of Ti/AZ91 bonded for 2 h. For Ti/Mg alloy dissimilar materials, applying a bonding time of 1 h is enough to obtain a satisfied bonding efficiency. That is to say, the bonding efficiency did not significantly improve when increasing the bonding time to 2 h. This can be explained by the microstructure at the bonding interface, where the samples bonded for 1 and 2 h exhibit the same characteristics. The thin Ti_3Al layer was only observed in Ti/AZ80 and Ti/AZ91, where the thickness of Al diffusion layer was similar. The bonding time of 1 h seems to be sufficient for Al atom diffusion from a Mg alloy side to a Ti side. Titanium and Mg alloys were also bonded by applying a bonding time of 0.5 h. However, all the samples exhibited a very poor bonding strength and failed after SPS because of an insufficient bonding time.

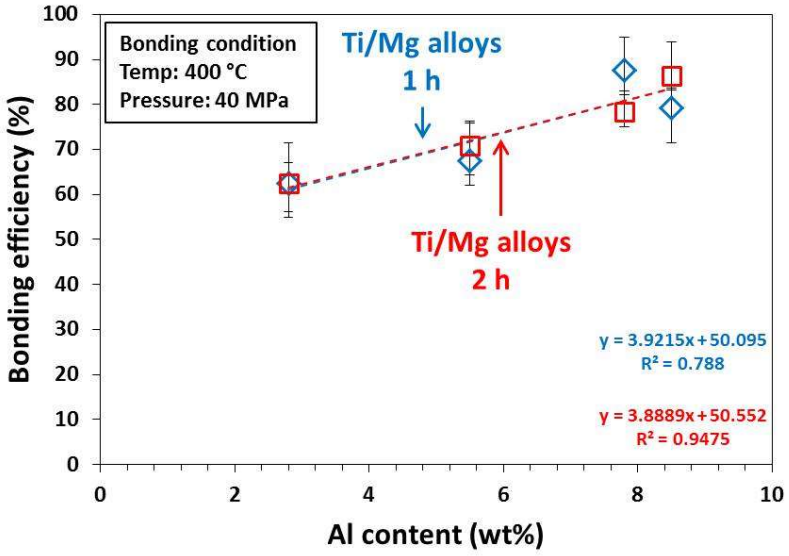

Fig. 4.21 Effect of Al content and bonding time on bonding efficiency of Ti/Mg alloys dissimilar materials bonded at 400 ºC under an applied pressure of 40 MPa.

4.4 Bonding of pure Ti to solution treated Mg alloys

In order to improve the bonding strength of the bonded materials, a solution heat treatment process was performed for Mg alloys before bonding to pure Ti. The solution treatment can dissolve all of the brittle $Mg_{17}Al_{12}$ particles into Mg matrix and then provide a homogenous Al distribution in the bonding surface of Mg alloys [90]. In the previous sections, a thin Ti_3Al layer was introduced at the bonding interface of Ti bonded to AZ80 or AZ91. However, this intermetallic compound was observed in only in sporadic areas because of the non-homogeneous Al distribution in the bonding surface. The formation of Ti_3Al layer was an important bonding mechanism for pure Ti and Mg alloys. Thus, modifying the distribution of Al element in the surface before bonding could facilitate the formation of continuous Ti_3Al layer and result in an improvement of the bonding strength.

4.4.1 Solution treated Mg alloys or Mg alloys (ST)

Mg alloys to be bonded to pure Ti were solution treated in muffle furnace at 420 ºC and subsequently quenched in water. Figure 4.22 shows the microstructures of AZ91 after solution treatment (ST) in various holding times. The microstructure of as-received AZ91 shows a large amount of $Mg_{17}Al_{12}$ particles in the matrix (Fig. 4.22a). After solution treatment for 4 h, $Mg_{17}Al_{12}$ particles started to dissolve into the matrix where the dissolved area appears in dark located around remained $Mg_{17}Al_{12}$ particle (Fig. 4.22b). After 8 h of solution treatment, most of $Mg_{17}Al_{12}$ particles were dissolved into the matrix and the remained particles were located at grain boundaries (Fig. 4.22c). All of $Mg_{17}Al_{12}$ particles were dissolved into the matrix after 12 h of solution treatment, and grain boundaries were clearly observed. Then, a final microstructure consisting of Mg matrix with no $Mg_{17}Al_{12}$ particles was obtained.

Figure 4.23 shows the microstructures of the four kinds of Mg alloys applied in this study after solution treatment at 420 ºC for 12 h, following with immediate quenching in water. All the Mg alloys show an identical microstructure and grain size, where only Mg matrix grains and twins were observed. This confirmed that the solution treatment at 420 ºC for 12 h following with quenching in water is sufficient to dissolve all $Mg_{17}Al_{12}$ particles into the matrix for all the Mg alloys [91].

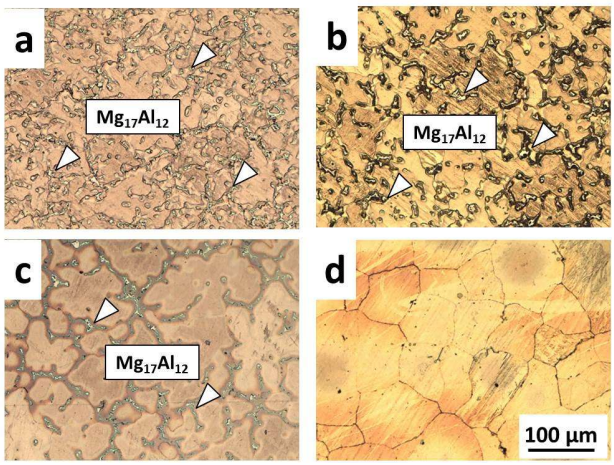

Fig. 4.22 Microstructures of AZ91 after solution treatment and quenched in water for various holding times a) As-received, b) 4 h, c) 8 h, and d) 12 h.

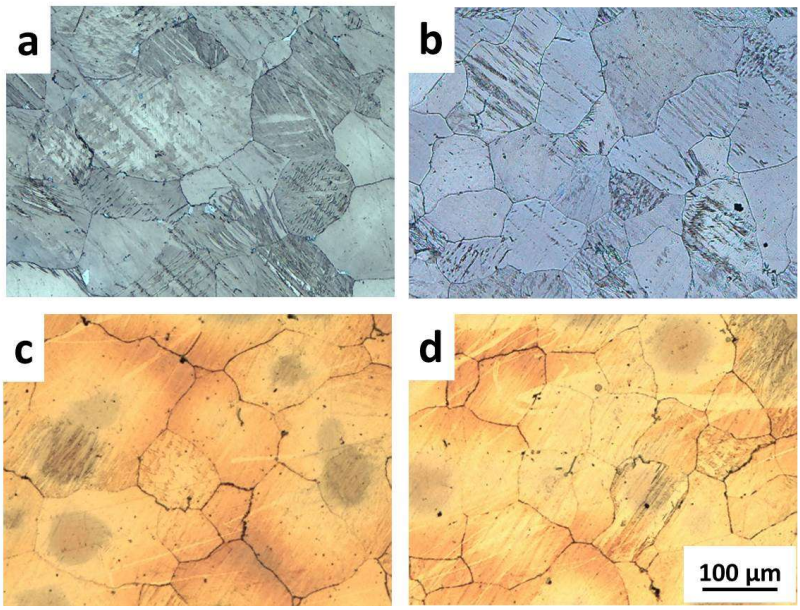

Fig. 4.23 Microstructures of Mg alloys after solution treatment at 420 ºC for 12 h and quenched in water a) AZ31B, b) AZ61, c) AZ80, and d) AZ91.

4.4.2 Interface characteristic of Ti/Mg alloy (ST) bonded materials

Figure 4.24 shows the microstructures at the bonding interface of pure Ti bonded to AZ91 (ST) at 400 ºC for 2 h under an applied pressure of 40 MPa. The solution treated Mg alloys will be hereafter noted as Mg alloys (ST). The microstructures of the bonding interface of Ti/Mg alloys (ST) observed by SEM are similar to those bonded to non-solution treated Mg alloys. The fine bonding interface was observed with no crack, void or undesired oxide layer. The other Ti/Mg alloy (ST) bonded materials bonded at 400 ºC for 2 h also show a similar bonding interface to Ti/AZ91 (ST) when observed by SEM. The TR $Mg_{17}Al_{12}$ was observed at the bonding interface, which however only shows in fewer areas than that bonded with non-solution treated Mg alloys. The RE $Mg_{17}Al_{12}$ was not observed at the bonding interface since all of the $Mg_{17}Al_{12}$ particles was already dissolved into the Mg matrix. SEM-EDS mapping images of Ti, Mg and Al are shown in Fig. 4.24. However, both the diffusion of those elements and the formation of an interaction layer cannot be detected.

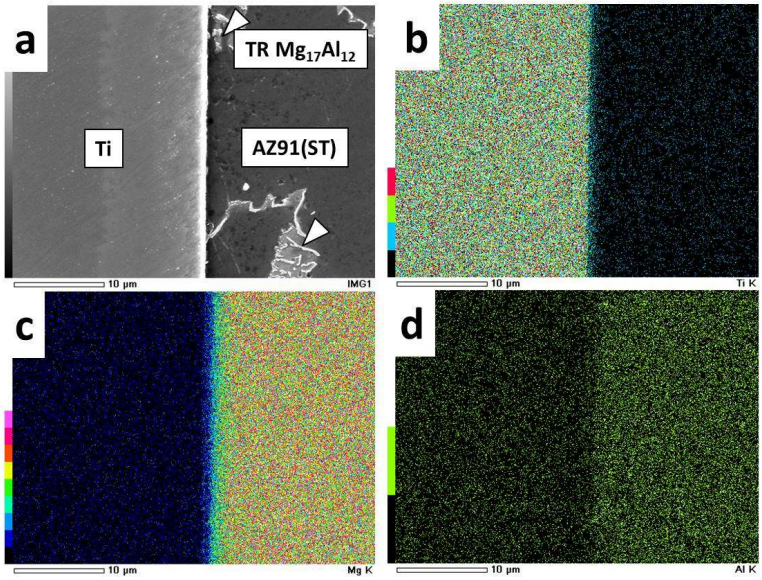

Fig. 4.24 SEM-EDS analysis at the bonding interface of Ti/AZ91 (ST) dissimilar materials bonded at 400 ºC for 2 h a) SE image at the bonding interface, b) Ti mapping, c) Mg mapping, and d) Al mapping.

In order to investigate the distribution of Al element in the bonding surface of Mg alloys, samples were cut from the Mg alloy side of the bonded materials near the bonding interface. The samples were cut from both Ti/Mg alloy and Ti/Mg alloy (ST) bonded materials bonded at 400 ºC for 2 h to compare the difference in Al distribution between the solution treated and non-solution treated Mg alloys after bonding. Figure 4.25 shows the microstructures of the non-solution treated Mg alloys cut from the bonded materials. The microstructure of AZ31B (Fig. 4.25a) shows slightly high Al content areas (black area) while most area of the matrix contain a low Al content (grey area). High Al content areas are easily observed in AZ61 since Al content increases and these areas seem to appear at grain boundaries. The small amount of TR $Mg_{17}Al_{12}$ was also observed on the matrix near the high Al content area (Fig. 4.25b). In the case of AZ80, large areas of high Al content and TR $Mg_{17}Al_{12}$ are observed at grain boundaries. The distribution of the high Al content area in AZ80 is more uniform in comparison with AZ61 (Fig. 4.25c). For AZ91, most of the matrix contains high Al content, and these areas were much more uniform compared to AZ80 (Fig. 4.25d). This result shows that a high bonding strength was obtained for samples where the Mg alloy contains a high Al content, and a uniform distribution of

the Al element in the bonding surface [92].

Figure 4.26 shows the Al concentrations measured from low (grey) and high (black) Al content area in Fig. 4.25 in each Mg alloy. The Al content measured from both low and high Al content areas is found increasing with the Al content in Mg alloys. For AZ31B, the difference in the Al content of two different areas is 2.5 wt%. The difference in Al content between grey and dark area is larger in AZ61, AZ80 and AZ91, where shows a different value of 4-5 wt%. The large difference of Al contents may cause a difference in mechanical properties of the bonded materials.

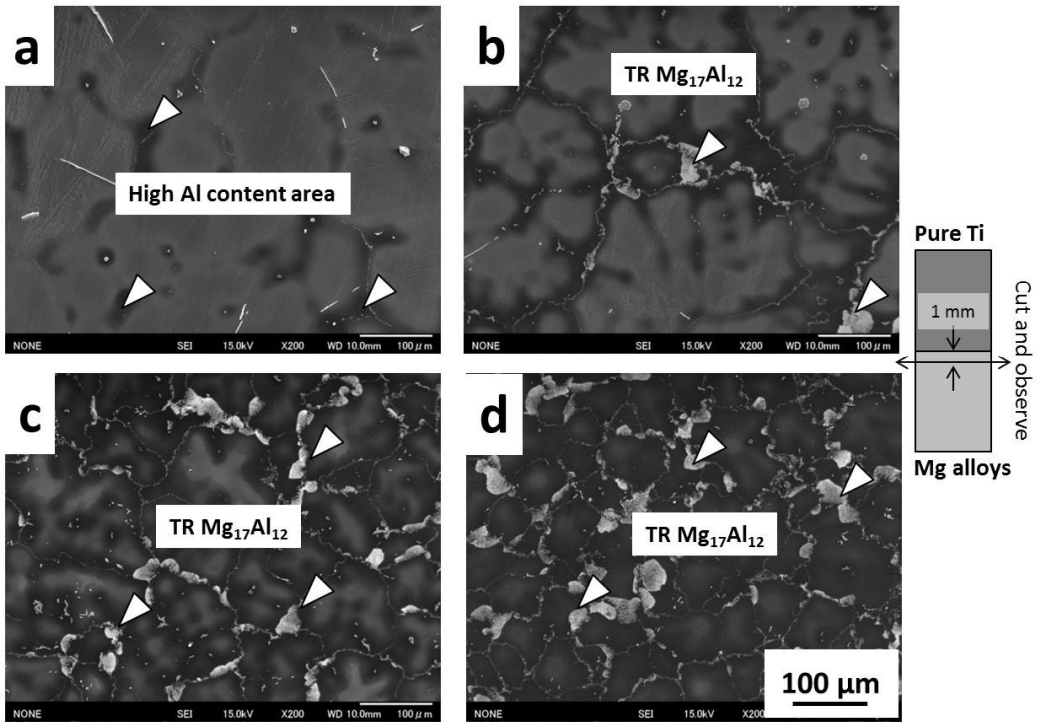

Fig. 4.25 Microstructures of Mg alloys cut from bonded materials near the bonding interface of a) AZ31B, b) AZ61, c) AZ80, and d) AZ91.

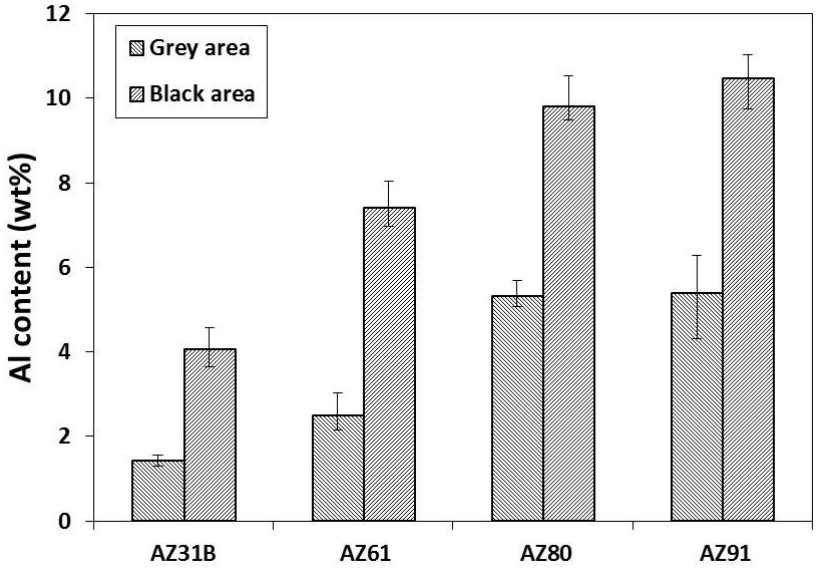

Fig 4.26 Concentration of Al in low (Grey) and high (Black) Al content area in each Mg alloy measured from Fig. 4.25.

Figure 4.27 shows the microstructures of the Mg alloys (ST) cut from the bonded materials bonded at 400 ºC for 2 h near the bonding interface. The microstructure of AZ31B (ST) shows a high Al content in some areas similar to Fig. 4.25a, where the difference in contrast between the low and high Al content areas decreases due to the effect of solution treatment (Fig. 4.27a). The decrease in contrast is also visible in AZ61. As such, it confirmed that the distribution of Al in the Mg matrix was uniform. The TR $Mg_{17}Al_{12}$ was also barely observed in the solution treated sample due to solution treatment (Fig. 4.27b). On the other hand, in the case of AZ80 (ST) and AZ91 (ST), there is almost no contrast difference between the low and high Al content areas, and at the same time the black area at the grain boundary disappears. This indicates that the distribution of Al was much more uniform in those Mg alloys after solution treatment at 420 ºC for 12 h. Elimination of brittle TR $Mg_{17}Al_{12}$ is also achieved that it almost disappears from Mg alloys matrix after SPS.

Figure 4.28 shows the Al concentrations measured from the low and high Al content areas in Fig. 4.27. AZ31B (ST) shows a difference of 1 wt% in the Al content between two areas. This difference is smaller than that of AZ31B, where a difference of 2.5 wt% was obtained. The differences in the

Al content between different areas in AZ61 (ST), AZ80 (ST) and AZ91 (ST) are 2, 1.7 and 2.5 wt%, respectively. These values are lower than those obtained for AZ61, AZ80 and AZ91 without solution treatment, for which the values of 4.9, 4.5 and 5 wt% are obtained, respectively. Moreover, the average values of Al content measured on the matrix are close to the genuine Al contents in the Mg alloys. This further confirmed that the uniform distribution of Al element was achieved in the Mg alloys (ST) by solution treatment at 420 ºC for 12 h.

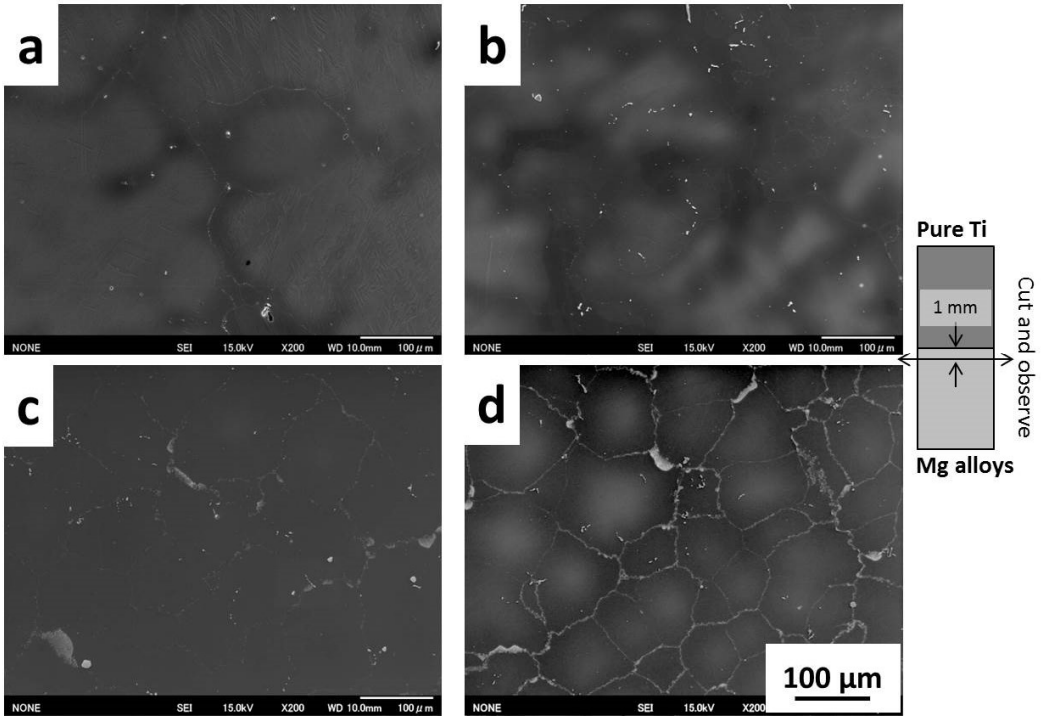

Fig. 4.27 Microstructures of Mg alloys (ST) cut from bonded materials near the bonding interface of a) AZ31B (ST), b) AZ61 (ST), c) AZ80 (ST), and d) AZ91 (ST).

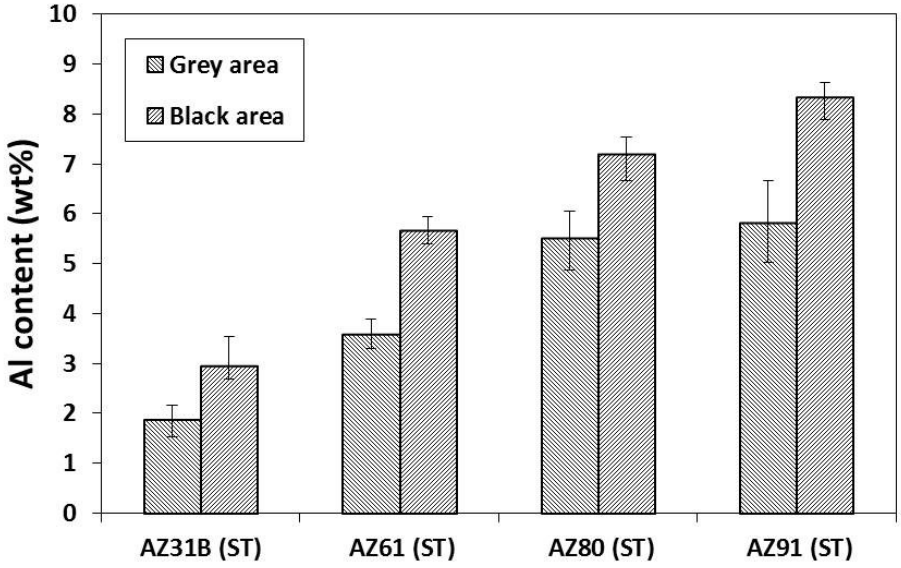

Fig. 4.28 Concentration of Al in low (Grey) and high (Black) Al content area in each Mg alloy (ST) measured from Fig. 4.27.

4.4.3 Bonding strength of Ti/Mg alloy (ST) bonded materials

Fig. 4.29 shows the bonding strengths of the bonded materials using either Mg alloys or Mg alloys (ST). All the samples were bonded with the same condition at 400 ºC for 2 h under an applied pressure of 40 MPa. It is obvious that the bonding strengths of Ti/Mg alloys (ST) are higher than that of Ti/Mg alloys. Namely, for Ti/AZ31B (ST), the bonding strength increases from 101.8 to 140.1 MPa when using the solution treated AZ31B. This has been confirmed by repetitive tensile tests. The large increase in the bonding strength of Ti/AZ31B (ST) can be explained by the great improvement of Al distribution. This is similar to Ti/AZ80 (ST) and Ti/AZ91 (ST), where the Al distribution is rather uniform even without solution treatment. Similar to Ti/AZ31B (ST), the bonding strength of Ti/AZ61 (ST) increases from 120.5 to 135.7 MPa, and the tensile strengths obtained from three repeated tests are rather similar.

The bonding strength of Ti/AZ61 (ST) however is slightly lower than that of Ti/AZ31B (ST), which may be caused by non-uniform Al distribution in the bonding surface. In the case of Ti/AZ80 (ST) and Ti/AZ91 (ST), an increment of bonding strength about 20 and 24 MPa was achieved, respectively. The tensile strengths obtained for the bonded samples using

AZ80 (ST) and AZ91 (ST) are similar to those using non-solution treated AZ80 and AZ91. This can be attributed to the fact that the bonding surfaces of AZ80 and AZ91 are already the Al-rich areas. The improvement of bonding strength in Ti/Mg alloy (ST) was relied on the solution treatment, which provides a uniform distribution of Al. This made Al element uniformly diffused at the bonding interface, and therefore a uniform bonding strength can be obtained because a uniform reaction between Ti and Al.

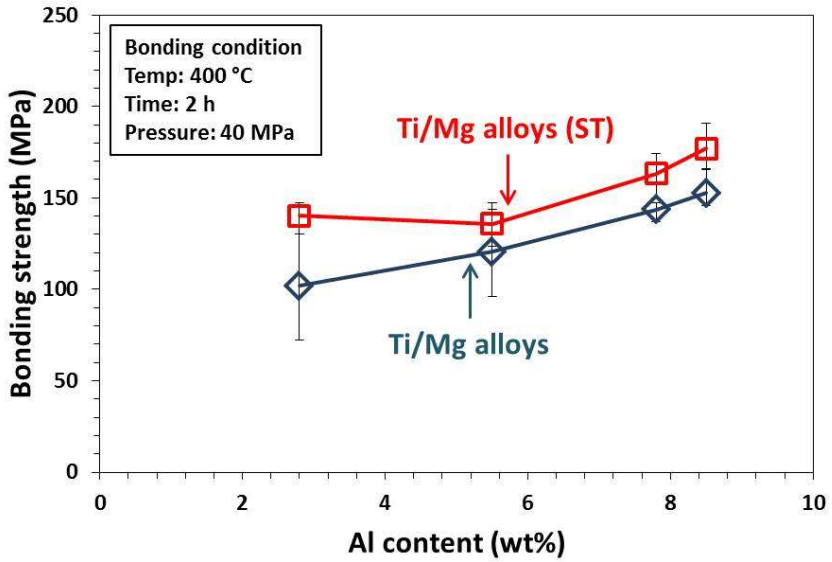

Fig. 4.29 Effect of Al content and solution treatment on bonding strength of Ti/Mg alloys dissimilar materials bonded at 400 ºC for 2 h.

Figure 4.30 shows the stress-strain curves of Ti/AZ31B and Ti/AZ31B (ST) bonded materials bonded at 400 ºC for 2 h, obtained from three tensile specimens. Titanium bonded to non-solution treated AZ31B shows a variable bonding strength such as 72, 103.5 and 130 MPa. On the other hand, Ti bonded to AZ31B (ST) exhibits the bonding strength much more uniformly, with the values of 146.2, 158.8 and 163.4 MPa. From the stress-strain curves, the bonding strength of Ti/AZ31B (ST) is higher than that of Ti/AZ31B due to the solution treatment effect. The ductility of the bonded materials was also improved about two times when using the Mg alloy (ST). For Ti/Mg alloys, the ductility is low for each bonded specimen and not exceeds 1.5%. On the other hand, Ti/Mg alloys (ST) show a high ductility that the value of each sample is almost 2%. The ductility range between

maximum and minimum value also decrease from 0.9% to 0.3% by an effect of solution treatment. The ductility seems to depend on bonding strength, where a higher strength normally causes larger deformation for the Mg alloy side [93].

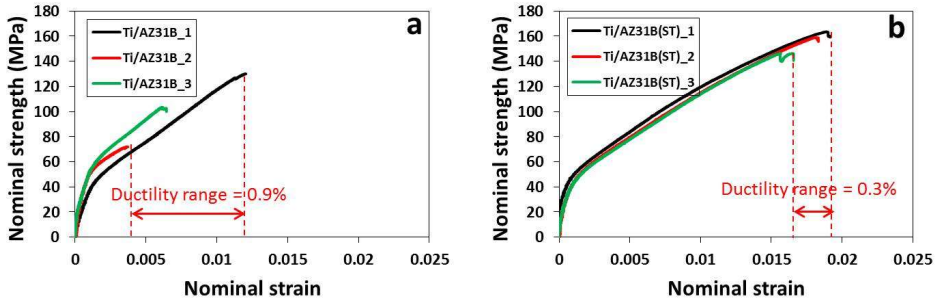

Fig. 4.30 Stress-strain curves of a) Ti/AZ31B and b) Ti/AZ31B (ST) bonded at 400 ºC for 2 h under an applied pressure of 40 MPa obtained from three specimens.

Figure 4.31 shows the bonding efficiency for Ti/Mg alloy and Ti/Mg alloy (ST) dissimilar materials bonded at 400 ºC for 2 h. It is clear that the bonding efficiency of Ti/Mg alloy (ST) is higher than that of Ti/Mg alloy for all the bonded materials, which agrees with their bonding strength. The highest bonding efficiency was obtained for Ti/AZ91 (ST) to be 88.1%, while the other Ti/Mg alloys and Ti/Mg alloys (ST) bonded materials also exhibited a satisfied bonding efficiency. The relationship between the bonding efficiency and Al content is proportional. That is to say, the bonding efficiency increases with the Al content in the Mg alloys.

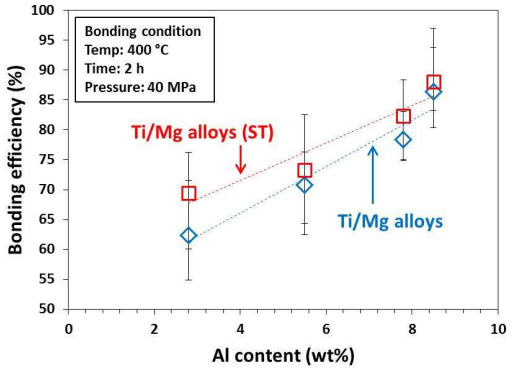

Fig. 4.31 Effect of Al content and solution treatment on bonding efficiency of Ti/Mg alloys dissimilar materials bonded at 400 ºC for 2 h.

4.4.4 Effect of bonding time on bonding strength

Fig 4.32 shows the bonding strengths of the Ti/Mg alloys (ST) bonded materials bonded at 400 ºC with various bonding times including 0.5, 1 and 2 h. The Ti/Mg alloy (ST) bonded for 0.5 h shows a poor bonding strength, while only Ti/AZ91 (ST) exhibits a good bonding strength when applying a bonding time of 0.5 h. In the case of Ti/AZ31B (ST), all the tensile specimens failed at the very early stage of the test. This can be explained by the low Al content in AZ31B and a short bonding time that resulted in a non-uniform Al diffusion. This also happened to Ti/AZ61 (ST), where one tensile specimen failed before the tensile test. Ti/AZ80 (ST) also exhibits a poor bonding strength with an ultimate strength of 130.6 MPa when applying a bonding time of 0.5 h. This result indicates that the short bonding time of 0.5 h is not sufficient for bonding between pure Ti and Mg alloys due to an inadequate diffusion of Al element.

The bonded materials that were bonded at 400 ºC for 1 and 2 h show a similar bonding strength, similar to those obtained for Ti/Mg alloys bonded materials using non-solution treated Mg alloys. This suggests that one hour is sufficient to obtain a maximum bonding strength for the bonded materials at certain temperatures. It can be a great advantage that, while maintained a high bonding strength, half of the processing time is reduced for producing the dissimilar bonded materials.

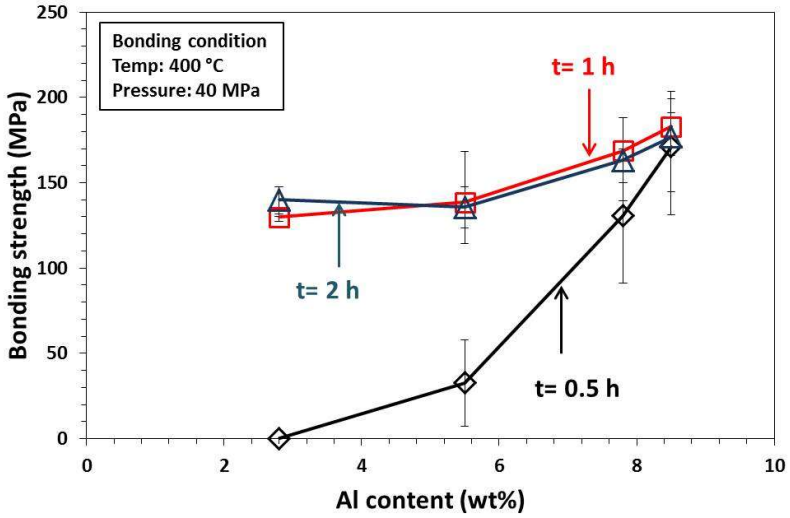

Fig. 4.32 Effect of Al content and bonding time on bonding strength of Ti/Mg alloys (ST) dissimilar materials bonded at 400 ºC under an applied pressure of 40 MPa.

Figure 4.33 shows the characteristics of Al diffusion at the bonding interface of Ti/AZ61 (ST) bonded at 400 ºC for 0.5 and 1 h, respectively. The bonding interface of Ti/AZ61 (ST) bonded for 0.5 h shows no formation of intermetallic layer at the bonding interface in the TEM bright field image. The mapping image of Al element on the right side shows a non-uniform diffusion in the thin layer. This is because a bonding time of 0.5 h was not sufficient to provide a thick and uniform Al diffusion layer (Fig. 4.33a). This result corresponds to its bonding strength, which exhibits a low value of 32.6 MPa. The TEM bright field image of Ti/AZ61 (ST) bonded at 400 ºC for 1 h shows the similar characteristics to Ti/AZ61 (ST) bonded for 0.5 h that no intermetallic layer was observed. The mapping image of Al shows a uniform Al diffusion layer with a thickness of 34 nm (Fig. 4.33b). This resulted in the improvement of bonding strength from 32.6 to 138.5 MPa in comparison to the sample bonded for 0.5 h.

In the case of Ti/AZ80 (ST) and Ti/AZ91 (ST), the Al mapping at the bonding interface between the samples bonded for 0.5 and 1 h are similar. The uniform diffusion of Al element was achieved even with applying a short bonding time because they possessed a much higher Al content in the Mg matrix compared to AZ31B (ST) and AZ61 (ST). There is almost no difference in bonding strength for Ti/AZ80 (ST) and TiAZ91 (ST) when increasing the bonding time from 0.5 to 1 h compared to Ti/AZ31B (ST) and Ti/AZ61 (ST) because of the aforementioned reasons. The thin Ti_3Al layer also observed in Ti/AZ80 (ST) and TiAZ91 (ST) bonded for 0.5 h in a few areas.

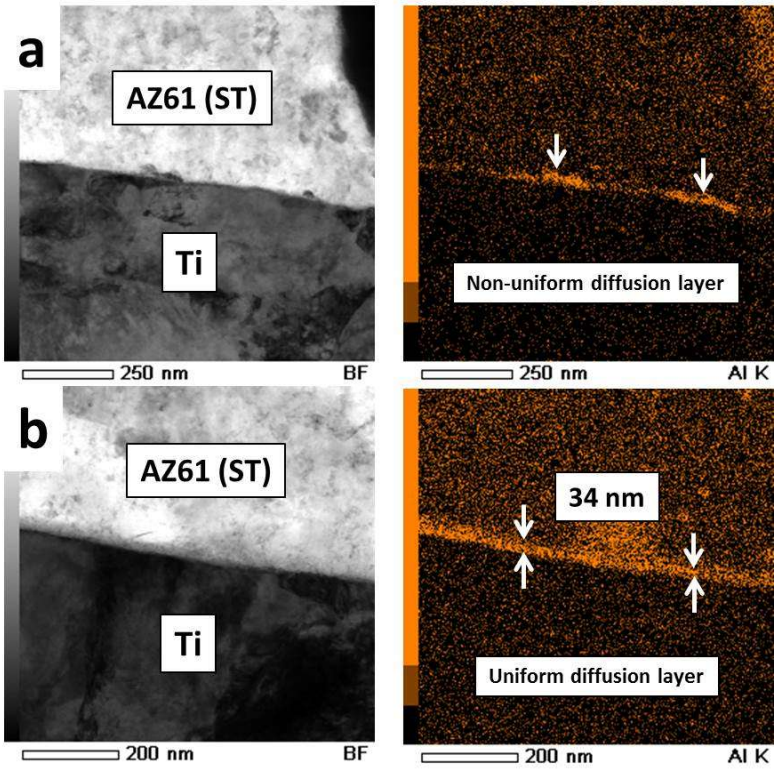

Fig. 4.33 Al mapping by TEM at the bonding interface of Ti/AZ61 (ST) bonded at 400 °C for a) 0.5 h and b) 1 h under an applied pressure of 40 MPa.

4.4.5 Effect of bonding pressure on bonding strength

Figure 4.34 shows the effect of various bonding pressures from 10 to 40 MPa on the bonding strength of Ti/Mg alloy (ST) materials bonded at 400 °C for 1 h. The bonding strengths obtained from these three bonding conditions are rather similar. This was explained by a sufficient deformability of Mg alloys that resulted in a perfect metallurgical contact between pure Ti and Mg alloys even at a low bonding pressure [94].

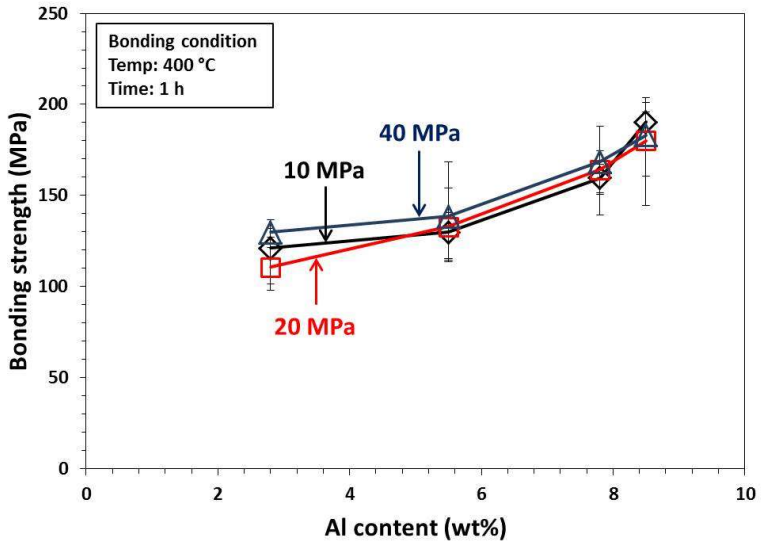

Fig. 4.34 Effect of Al content and bonding pressure on bonding strength of Ti/Mg alloys (ST) dissimilar materials bonded at 400 ºC for 1 h.

Figure 4.35 shows the bonding interface of Ti/AZ31B (ST) bonded at 400 ºC for 1 h under pressures of 10 and 40 MPa, respectively. At the low bonding pressure of 10 MPa, a fine bonding interface without crack, void or oxide layer was obtained similar to that bonded at 40 MPa. The difference in the characteristics at the bonding interface between the samples bonded at 10 and 40 MPa is the amount of high dislocation density areas. Mg alloys in the sample bonded at 40 MPa experienced a high deformation in the matrix and therefore the high dislocation density area was easily observed compared to the sample bonded at 10 MPa. This result suggests that a low bonding pressure of 10 MPa was sufficient to bond pure Ti to Mg alloys. The decrease in bonding pressure from 40 to 10 MPa has an advantage, since the graphite container could be broken more easily if a high pressure is applied for many times.

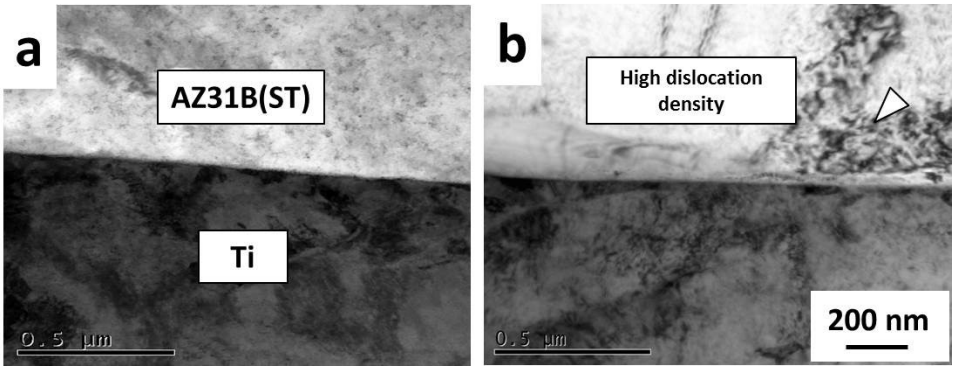

Fig. 4.35 High dislocation density area at the bonding interface of Ti/AZ31B (ST) bonded at 400 ºC for 1 h under an applied pressure of a) 10 MPa and b) 40 MPa

4.4.6 Effect of bonding temperature on bonding strength

Figure 4.36 shows the bonding strengths of Ti/Mg alloys (ST) dissimilar materials bonded at various temperatures such as 400, 420, 450 and 475 ºC for 1 h under an applied pressure of 10 MPa. The bonding strengths of Ti/AZ31B (ST) and Ti/AZ61 (ST) increase gradually with an increase on temperature from 400 to 475 ºC, which corresponds to a strength increase in about 15 and 27 MPa for Ti/AZ31B (ST) and Ti/AZ61 (ST), respectively. The bonding strengths of Ti/AZ80 (ST) and Ti/AZ91 (ST) also increase with the bonding temperature. Nevertheless, the increasing values are relatively low (about 10 MPa). This result suggests that bonding at 400 ºC was sufficient for Ti/AZ80 (ST) and Ti/AZ91 (ST) to obtain a good bonding strength but not for Ti/AZ31B (ST) and Ti/AZ61 (ST), for which higher bonding temperatures are required. The maximum bonding strength of 193.4 MPa was obtained for Ti/AZ91 (ST) bonded at 475 ºC. From the above, it is verified that increasing the bonding temperature can enhance the diffusion of Al element, as well as, the reaction between Ti and Al at the bonding interface.

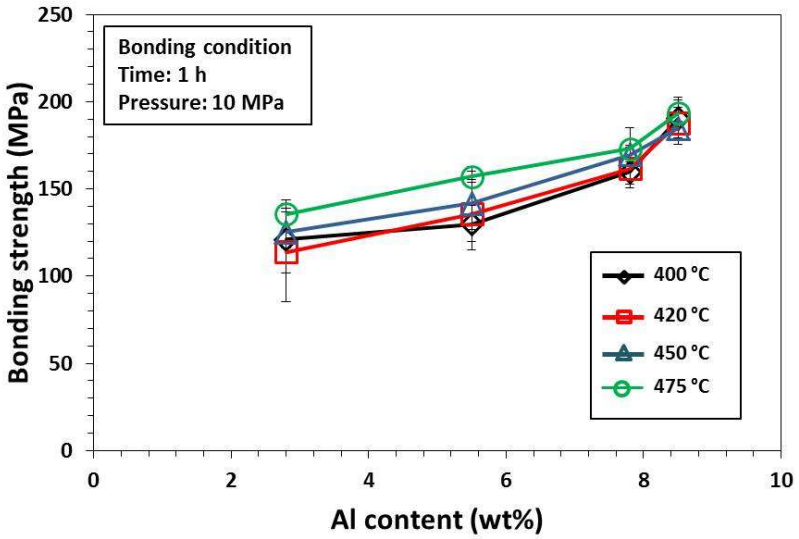

Fig. 4.36 Effect of Al content and bonding temperature on bonding strength of Ti/Mg alloys (ST) dissimilar materials bonded for 1 h under an applied pressure of 10 MPa.

Figure 4.37 shows the bonding efficiency of Ti/Mg alloys (ST) dissimilar materials bonded at 400, 420, 450 and 475 ºC for 1 h under an applied pressure of 10 MPa. The result shows that the bonding efficiency of the bonded materials gradually increases with the bonding temperature, which is in line with their bonding strengths. In the case of Ti/AZ31B (ST) and Ti/AZ61 (ST), the bonding efficiency was improved greatly by increasing the bonding temperature from 450 to 475 ºC. On the other hand, the bonding efficiency of Ti/AZ80 (ST) and Ti/AZ91 (ST) was also improved, but only with a lower amount than that for Ti/AZ31B (ST) and Ti/AZ61 (ST). The highest bonding efficiency of 96.3% was obtained for Ti/AZ91 (ST) bonded at 475 ºC, where the sample also shows an excellent bonding strength close to the UTS of parent Mg alloy.

The liquid phase appears at the Mg alloy side in AZ80 (ST) and AZ91 (ST) when the bonding temperature reaches 420 ºC, for AZ31B (ST) and AZ61 (ST), this occurs at a bonding temperature of 475 ºC. The droplet of Mg alloy was found on the graphite container after SPS, which can be a result of squeezing the metal liquid through the gap between the graphite container and the bonded sample by the applied pressure. The bonding strength of Ti/Mg alloys (ST) bonded at various temperatures for 1 h at 10

MPa is concluded in Table 4.3. This result emphasize the important effect of bonding temperature and Al content in Mg alloys on bonding strength of Ti/Mg alloys bonded materials.

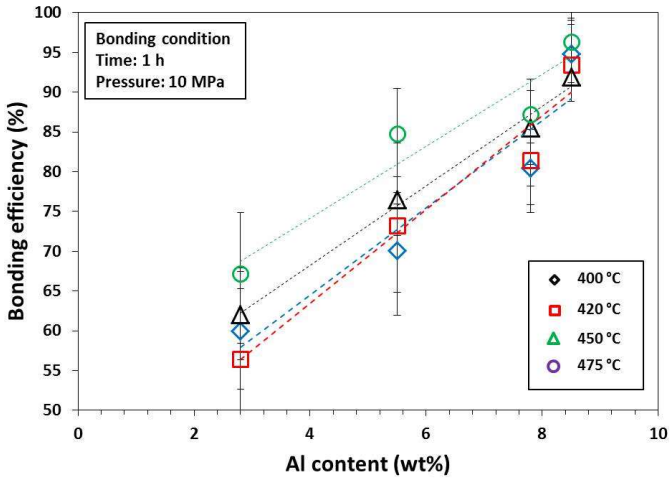

Fig. 4.37 Effect of Al content and bonding temperature on bonding efficiency of Ti/Mg alloys (ST) dissimilar materials bonded for 1 h under an applied pressure of 10 MPa.

Table 4.3 Average bonding strength of Ti/Mg alloys (ST) bonded for 1 h at 10 MPa from three specimens.

T_b / Materials	400°C	420°C	450°C	475°C
Ti/AZ31B(ST)	121 (137/102)	114 (142/86)	125 (139/116)	136 (144/127)
Ti/AZ61(ST)	130 (141/116)	136 (156/120)	142 (163/127)	157 (160/154)
Ti/AZ80(ST)	160 (168/151)	162 (174/153)	170 (176/166)	173 (185/168)
Ti/AZ91(ST)	190 (201/175)	188 (197/177)	185 (189/180)	193 (203/187)

T_b = Bonding temperature (°C)

Note: (maximum value/ minimum value)

Figure 4.38 shows the differential thermal analysis (DTA) profile for each Mg alloy (ST). The samples were heated up to 650 °C with a heating rate of 5 °C/min under vacuum atmosphere. The solidus temperature for AZ31B (ST) and AZ61 (ST) was measured to be approximately 460 °C. For AZ80 (ST) and AZ91 (ST), the solidus temperature was around 423 °C. This result corresponds to the temperature at which the liquid phase was found

in each bonding process with different applied Mg alloys. The measured solidus temperature of AZ80 (ST) and AZ91 (ST) are lower than that of AZ31B (ST) and AZ61 (ST) because of a higher amount of Al content.

Figure 4.39 shows the bonding interface of Ti/AZ31B (ST) bonded at 475 ºC for 1 h under a bonding pressure of 10 MPa. The bonding interface shows an existence of discontinuous Ti_3Al layer that was also confirmed by the diffraction pattern (Fig. 4.39a) and dark field image where the IMC layer shows bright (Fig. 4.39b). For Ti/AZ31B (ST) and Ti/AZ61 (ST), the intermetallic layer can be observed only when the bonding temperature reaches 475 ºC. The liquid phase formation seems to facilitate a formation of the intermetallic layer at the bonding interface of Ti/AZ31B (ST) and Ti/AZ61 (ST) due to the increased diffusion rate of Al element in liquid state [95]. This phenomenon resulted in an improvement in the bonding efficiency of Ti/AZ31B (ST) and Ti/AZ61 (ST) when the bonding temperature increased from 450 to 475 ºC.

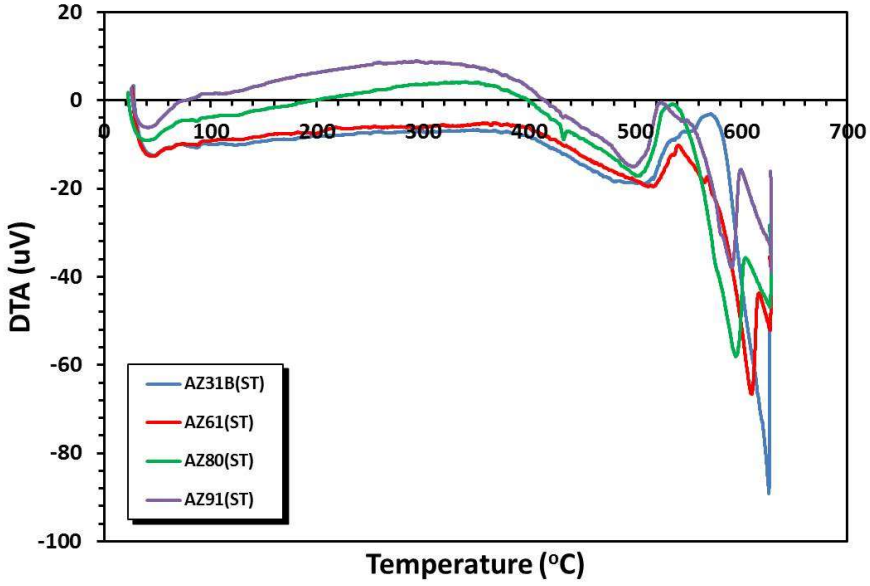

Fig. 4.38 DTA profiles of each Mg alloy (ST) heated up to 650 ºC with heating rate of 5 ºC/min under vacuum atmosphere.

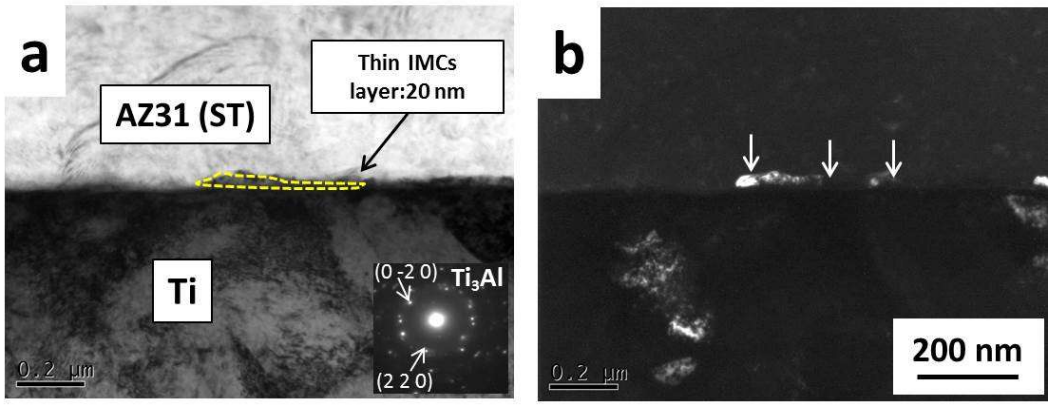

Fig. 4.39 TEM observation at the bonding interface of Ti/AZ31B (ST) bonded at 475 ºC for 1 h under an applied pressure of 10 MPa a) BF image and b) DF image.

Figure 4.40 shows the bonding interface of Ti/AZ91 (ST) dissimilar materials bonded at 475 ºC for 1 h under an applied pressure of 10 MPa. The TEM BF image also shows an existence of Ti_3Al layer at the bonding interface with a thickness of 50 nm (Fig 4.40a). This continuous intermetallic layer observed at the bonding interface, implies that the reaction between Al and Ti at the bonding interface was uniform. The TEM DF image associated with the diffraction pattern confirmed the existence of Ti_3Al layer at the bonding interface (Fig. 4.40 b).

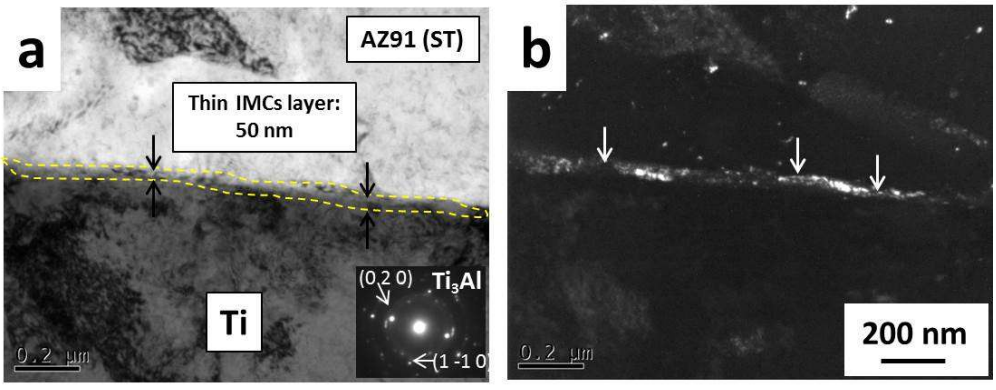

Fig 4.40 TEM observation at the bonding interface of Ti/AZ91 (ST) bonded at 475 ºC for 1 h under an applied pressure of 10 MPa a) BF image and b) DF image.

4.4.7 Fracture surface of Ti/Mg alloys (ST) bonded materials

Figure 4.41 shows the fracture surface of the Mg alloys (ST) side of Ti/AZ31B (ST) and Ti/AZ61 (ST), which were bonded at 400 and 475 ºC for 1 h under an applied pressure of 10 MPa, after tensile testing. Figure 4.41a shows the fracture surface of Ti/AZ31B (ST) bonded at 400 ºC. The fracture surface is rather smooth compared to the sample bonded at 475 ºC (Fig. 4.41b) where fracture damages were found in some areas. This is explained by the formation of Ti_3Al layer that improved the bonding strength. This also occurred in Ti/AZ61 (ST) that more severe fracture damages were found in the sample bonded at 475 ºC (Bonding strength: 157 MPa) than the sample bonded at 400 ºC (Bonding strength: 130 MPa).

Figure 4.42 shows the XRD analysis patterns for the fracture surface of Ti/AZ91 (ST) bonded at 475 ºC for 1 h under an applied pressure of 10 MPa. The pattern for the AZ91 (ST) fracture surface shows only Mg and $Mg_{17}Al_{12}$ peaks that are corresponding to the Mg matrix and TR $Mg_{17}Al_{12}$, respectively. There is no Ti peak appearing in the XRD pattern obtained for AZ91 (ST) fracture surface, which agrees with the SEM image that Ti debris is not observed on the fracture surface on the Mg alloy side. This is explained by that the bonding strength of Ti_3Al/Mg joints is weaker than that of Ti_3Al/Ti. For pure Ti side, the patterns of Ti, Mg and $Mg_{17}Al_{12}$ were detected, which agree with the SEM image that a large number of AZ91 (ST) debris were found on the Ti side of the fracture surface.

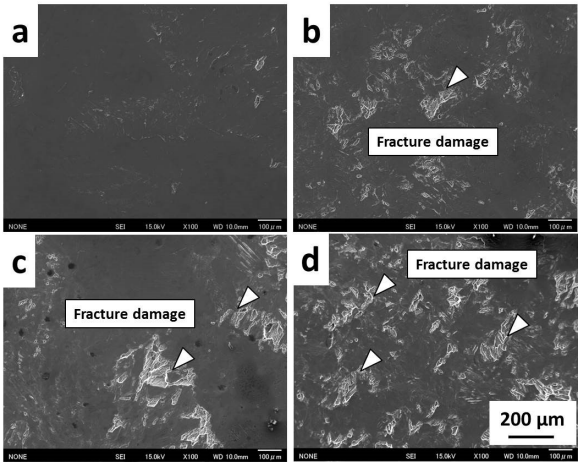

Fig. 4.41 Fracture surfaces observation on Mg alloys side of Ti/AZ31B (ST) bonded at a) 400 ºC, b) 475 ºC and Ti/AZ61 (ST) bonded at c) 400 ºC, d) 475 ºC for 1 h under an applied pressure of 10 MPa.

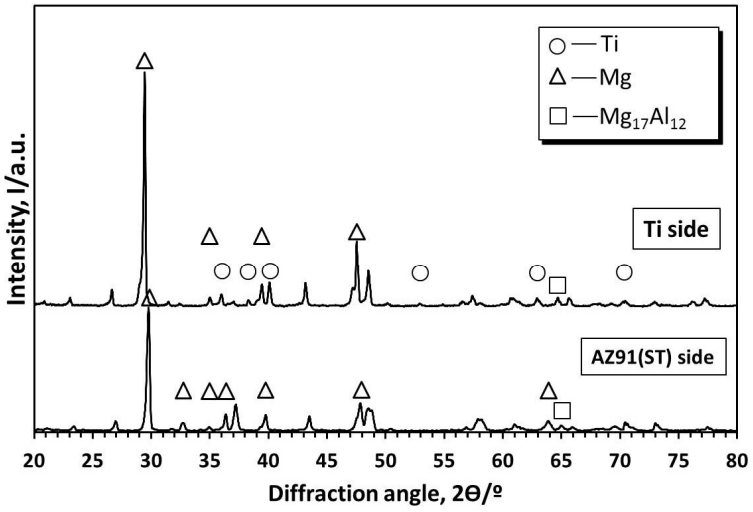

Fig. 4.42 XRD patterns obtained for fracture surfaces of Ti/AZ91 (ST) bonded at 475 ºC for 1 h under an applied pressure of 10 MPa.

4.5 Conclusion

Bonding between pure Ti and Mg alloys or Mg alloys (ST) has been achieved by applying SPS, where the high temperature and pressure can be simultaneously introduced to provide a perfect contact between pure Ti and Mg alloys so as to facilitate the reaction between Ti and Al in the Mg alloys. The high pressure applied in the bonding process resulted in a destruction of original oxide layer on both surfaces of pure Ti and Mg alloys. The bonding strength between the pure Ti and Mg alloys shows an increase with the Al content in the Mg alloys. This is attributed to the formation of Al diffusion layer and Ti_3Al intermetallic layer. The formation of Ti_3Al layer was found in Ti/AZ80 and Ti/AZ91 that exhibited a higher bonding strength than that of Ti/AZ31B and Ti/AZ61.

Bonding between Ti and Mg alloys (ST) shows much higher bonding strengths and efficiency than that between pure Ti and Mg alloys without solution treatment. It is because the solution treated Mg alloys show a highly uniform distribution of Al in the Mg matrix and all of the brittle RE $Mg_{17}Al_{12}$ particles are dissolved. On the other hand, a uniform Al diffusion layer was observed in all samples bonded at 400 ºC for 1 or 2 h.

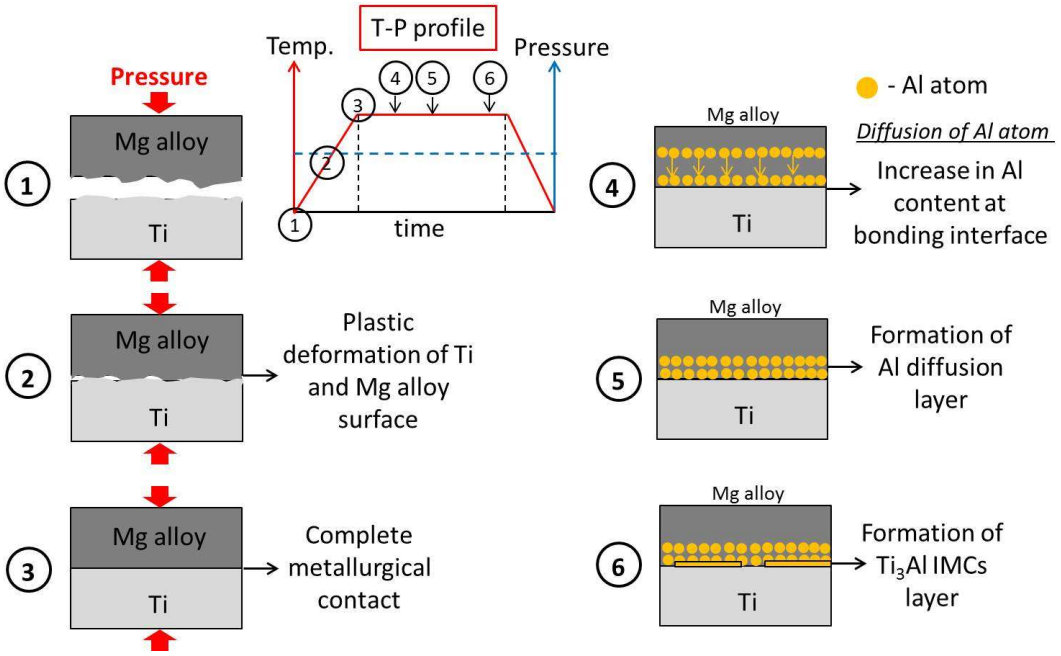

Fig. 4.43 Schematic illustration of bonding mechanism between pure Ti and Mg alloy.

Figure 4.43 shows the schematic illustration of bonding mechanism between pure Ti and Mg alloy. At first step, the pressure is introduced to sample since SPS is started. At second step, the temperature is gradually increases as shown in heating profile and two surfaces start to plastically deform. At third step, temperature reach at bonding temperature and the surface of Mg alloys become soft and easy to deform at high temperature that the complete metallurgical contact between pure Ti and Mg alloys is achieved. At fourth step, the temperature is held at bonding temperature and Al atom from Mg alloys side start to diffuse to Ti surface. At fifth step, Al atom form a segregated layer at the bonding interface result in the increase in Al content at the bonding interface. At sixth step, Al content reach over 8 wt% and Ti_3Al layer is formed at the bonding interface result in successful bonding between pure Ti and Mg alloys.

From the above experimental results, it is found that a bonding time of 1 h at 400 ºC is sufficient to bond pure Ti to Mg alloys with a satisfied bonding strength. However, a bonding time of 0.5 h can result in an incomplete diffusion of Al or the insufficient formation of discontinuous diffusion layer of Al, and thus gives rise to a poor bonding strength. In

addition, it is also found that the bonding pressure has no effect on the bonding strength. Namely, the samples bonded at 400 ºC using an applied pressure from 10 to 40 MPa exhibit a similar bonding strength. Nevertheless, the bonding temperature is an important factor for improving the bonding strength, where an increase of the temperature from 400 to 475 ºC results in an increase of both the bonding strength and efficiency for all the bonded materials. The bonding efficiency of Ti/AZ91 (ST) bonded at 475 ºC for 1 h under an applied pressure of 10 MPa reaches as high as 96.3%. This is the highest bonding strength obtained from the bonded materials between Ti and Mg alloys in this research. Liquidation of the Mg alloys at different temperatures was found for different Mg alloys. Specifically, Ti/AZ80 (ST) and Ti/AZ91 (ST) take place at 420 ºC, Ti/AZ31B (ST) and Ti/AZ61 (ST) occurs at 475 ºC. The liquidation process promotes the formation of Ti_3Al layer, resulting in improved bonding strength.

CHAPTER 5: CORROSION BEHAVIOR OF DISSIMILAR MATERIALS BETWEEN TITANIUM AND MAGNESIUM ALLOYS

5.1 Introduction

Galvanic corrosion is an inevitable problem in bonded materials. It occurs when two materials that possess different electrochemical potentials are contacted together [96]. All metals can be classified into a galvanic series by their electrochemical potentials developed in an electrolytic solution against a standard reference electrode [97]. The difference of the potentials between two metals in the galvanic series gives the information to determine the corroded metal when they are contacted together, as well as to evaluate the extent of corrosion. Insufficient attention to galvanic corrosion is one of the major obstacles to the structural application of Mg alloys. Improvements of the corrosion resistance of Mg alloys in salt water has been achieved through a strict limitation of the critical impurities such as nickel, iron and copper, as well as of the iron-to-manganese ratio [98]. However, these improvements have no significant effect on the galvanic corrosion, because the electromotive force for corrosion comes from an external source, the dissimilar metal coupled to magnesium. The prevention of galvanic corrosion damages thus requires a consideration of a combination of at least the following measures [99]:

- Design to prevent access and entrapment of salt water at the dissimilar metals joint.
- Selection of the most compatible dissimilar metals.
- Introduction of high resistance into a metallic portion of the circuit through insulator or into the electrolytic portion of the circuit by increasing the length of the path that electrolytic current must follow.
- Applying protective coating.

The formation of intermetallic layer by laser welding, soldering-brazing and solid state bonding procedure can effectively reduce the galvanic corrosion damage at the bonding interface. The formation of intermetallic layer can reduce the difference of surface potentials between pure Ti and Mg alloys [100, 101]. In this research, the galvanic corrosion resistance at the

bonding interface is improved by increasing Al content in the Mg alloys that bonded to Ti. The formation of Ti_3Al intermetallic compound and Al diffusion layer creates a potential gradient at the bonding interface where the surface potential gradually increases from Mg alloy to Ti side resulting in an improvement of the galvanic corrosion resistance. The corrosion resistance of Mg alloy matrix is also improved by increasing Al content in the Mg alloys due to the formation of stable Mg-Al-O film on the surface. The Mg-Al-O film possesses higher potential in corrosion protection than the $Mg(OH)_2$ film which is generally formed on Mg alloy surface when exposed to air [102, 103]. The improvement in galvanic and matrix corrosion resistance can increase the life span of bonded materials, and thus is as important as bonding strength.

5.2 Surface potential of parent metals and dissimilar materials

Figure 5.1 shows the bonding interface of Ti/Mg alloy (ST) bonded at 475 ºC for 1 h under an applied pressure of 10 MPa. The surface was ground and polished without etching, and kept under normal atmosphere for 1 day to form a stable surface oxide film. This resulted in a stable surface potential on both pure Ti and Mg alloy surfaces, which was measured later by a scanning kelvin probe force microscope (SKPFM) before corrosion test. The surface potential measured from SKPFM is an absolute value. The bonding interface of the sample bonded at 400 ºC for 1 h shows a similar character to the sample bonded at 475 ºC for 1 h. The surface show no second phase or IMC on both pure Ti and Mg alloy (ST) sides, and the intermetallic layer is not observed at the bonding interface.

Figure 5.2 shows the surface potential of the Mg alloys measured by SKPFM after solution treatment at 420 ºC for 12 h. This surface potential is an average value of those measured from three different positions. AZ31B (ST) and AZ61 (ST) show high surface potentials with values of 1.73 and 1.70 V, respectively. For SKPFM, The higher surface potential indicates that the material is more susceptible to corrosion than the lower surface potential one. On the other hand, AZ80 shows a lower surface potential than AZ31B (ST) and AZ61 (ST) with a value of 1.65 V. The increment in Al content in Mg alloys results in the decrease in surface potential, which can be attributed to the formation of stable Mg-Al-O film on the Mg alloy surface.

AZ91 (ST) shows the surface potential of 1.63 V, which is the lowest among all the Mg alloys used in this research due to its highest Al content. From the above results, AZ91 (ST) can possess the highest corrosion resistance among all the Mg alloys in line with their surface potential. The surface potential of pure Ti was also measured from three different positions, which give an average value of 0.78±0.03 V. This implies that pure Ti is much less susceptible to corrosion than Mg alloys. This is because the TiO_2 surface film is very effective for corrosion protection.

Figure 5.3 shows a mapping image of the surface potential difference (SPD) for Ti/Mg alloy measured by SKPFM. The left side of the mapping area (blue area) is a low surface potential area for pure Ti, while the right side (orange area) is a high surface potential area for Mg alloys. The surface was scanned from point A to B across the bonding interface with a distance of 10 μm.

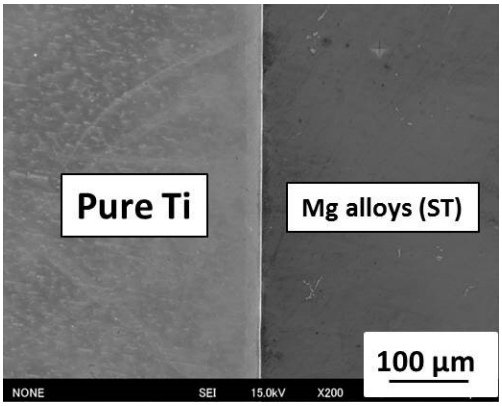

Fig 5.1 Bonding interface of Ti/Mg alloy (ST) bonded at 475 ºC for 1 h under an applied pressure of 10 MPa before corrosion test.

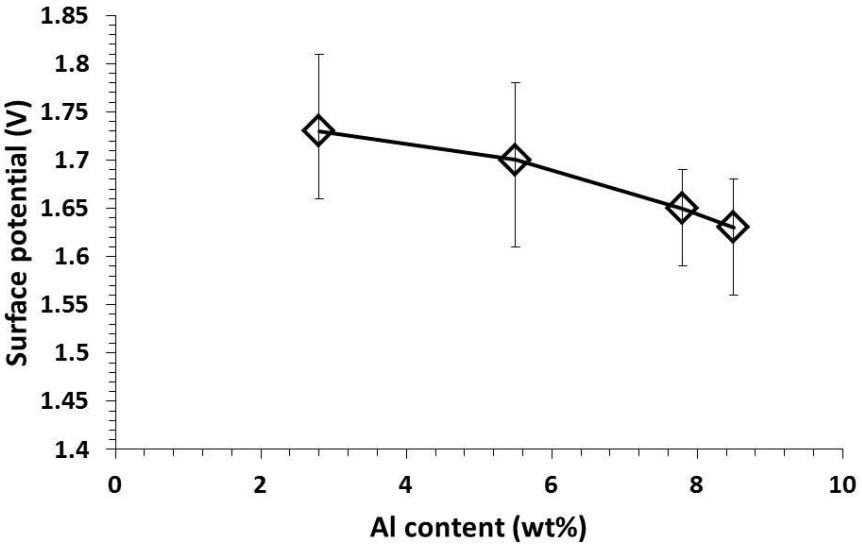

Fig 5.2 Effect of Al content on surface potential of Mg alloys after solution treatment at 420 ºC for 12 h.

Figure 5.4 shows the surface potential for Ti/Mg alloy bonded at 475 ºC for 1 h under an applied pressure of 10 MPa before corrosion test. The surface potential difference (SPD) between pure Ti and Mg alloys at the bonding interface was measured by SKPFM. The slope that represents a potential gradient (P.G.) was calculated from three different positions. From the surface potential profiles, the potential gradient is visible at the bonding interface (the dot line) of all the bonded materials. The gradient potentials indicate a surface potential change at the bonding interface because the presence of interaction or diffusion layer [104]. The existence of interaction or diffusion layer prevents a large and immediate surface potential change at the bonding interface, and reduces the galvanic corrosion damage. For Ti/AZ31B (ST) bonded materials, the surface potential difference (SPD) between Ti and AZ31B (ST) was measured to be 0.81 V. This SPD value is large, and can result in a severe galvanic corrosion at the bonding interface (Fig. 5.4a). The calculated slope that represents a potential gradient is 0.77 V/μm. The potential gradient of Ti/AZ31B (ST) is rather high that indicates an immediate change in surface potential at the bonding interface, and a poor galvanic corrosion resistance can be expected. The immediate change in surface potential at the bonding interface of Ti/AZ31B (ST) is attributed to a

poor reaction between Ti and Al that can form a thin Al diffusion layer of 30 nm and thin Ti_3Al layer, which have been observed in some areas (Fig. 4.39). AZ61 (ST) also shows a large SPD between the pure Ti and Mg alloy, and a high potential gradient at the bonding interface similar to Ti/AZ31B (ST) (Fig 5.4b). This is explained by the similar character observed in Ti/AZ31B (ST) and Ti/AZ61 (ST) at the bonding interface, where a thin Al diffusion layer and Ti_3Al intermetallic layer are observed. In the case of Ti/AZ80 (ST), the measured SPD value is 0.75 V (Fig. 5.3c). This indicates that the galvanic corrosion resistance of Ti/AZ80 (ST) is superior compared to Ti/AZ31B (ST) and Ti/AZ61 (ST), because SPD value obtained for Ti/AZ80 (ST) is lower than that for Ti/AZ31B (ST) and Ti/AZ61 (ST) [106]. Ti/AZ80 (ST) also exhibits a much lower potential gradient of 0.38 V/μm than Ti/AZ31B (ST) and Ti/AZ61 (ST). The gradual change in surface potential at the bonding interface of Ti/AZ80 (ST) suggests that this bonded material possesses a good galvanic corrosion resistance. The SPD and potential gradient of Ti/AZ91 (ST) is similar to that of Ti/AZ80 (ST) with the values of 0.77 V and 0.46 V/μm, respectively (Fig. 5.4d). This result suggests that Ti/AZ80 (ST) and Ti/AZ91 (ST) possess an equal galvanic corrosion resistance, while Ti/AZ31B (ST) and Ti/AZ61 (ST) possess a poor galvanic corrosion resistance due to the large SPD between pure Ti and Mg alloys, and high potential gradient.

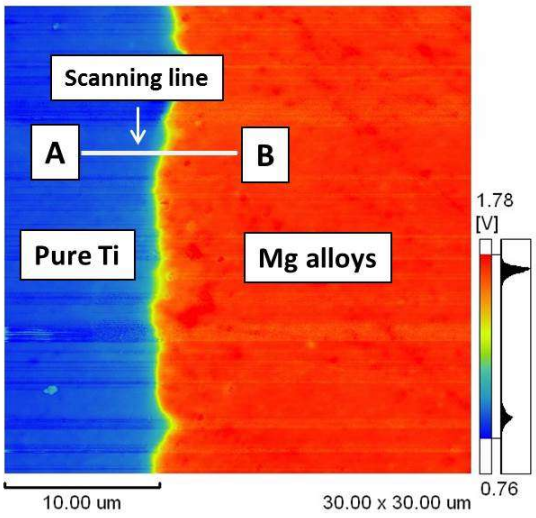

Fig. 5.3 Mapping image for surface potential difference (SPD) measurement between pure Ti and Mg alloys by SKPFM.

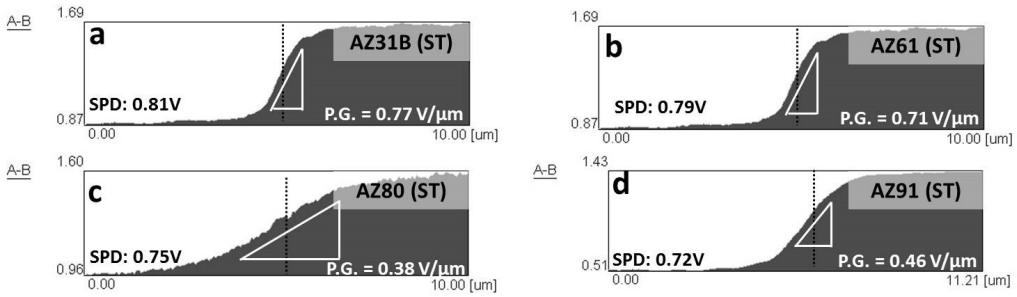

Fig. 5.4 Changes in surface potential measured across the bonding interface of a) Ti/AZ31B (ST), b) Ti/AZ61 (ST), c) Ti/AZ80 (ST), and d) Ti/AZ91 (ST) bonded at 475 ºC for 1 h under an applied pressure of 10 MPa.

Figure 5.5 shows the surface potential measured for the Ti/Mg alloy dissimilar materials bonded at 400 ºC for 1 h under an applied pressure of 10 MPa before corrosion test. The surface potential difference (SPD) between pure Ti and Mg alloys at the bonding interface was measured, and the potential gradient was calculated from three different positions similar to sample bonded at 475 ºC. For Ti/AZ31B (ST), the SPD between pure Ti and a Mg alloys and the calculated potential gradient are with value of 0.89 V and 0.82 V/µm, which are higher than the sample bonded at 475 ºC. The increased SPD and potential gradient compared to the sample bonded at 475 ºC is explained by the characteristics at the bonding interface, where the thin and non-uniform Al diffusion layer of 25 nm without formation of Ti_3Al (Fig. 4.12a) was observed in the Ti/AZ31B (ST) sample bonded at a low temperature of 400 ºC (Fig. 5.5a). Similar to the sample bonded at 475 ºC, the SPD and potential gradient of Ti/AZ61 (ST) bonded at 400 ºC are similar to Ti/AZ31B (ST) bonded at 400 ºC that both of them usually show high SPD and potential gradient (Fig. 5.5b). This is explained by the similar characteristics at the bonding interface of Ti/AZ31B (ST) and Ti/AZ61 (ST), where Al diffusion layer with a thickness of 27 nm without the formation of Ti_3Al. For Ti/AZ80 (ST), the SPD of 0.79 V was measured on the bonding interface and this value was slightly higher compared to the sample bonded at 475 ºC (Fig. 5.5c). The potential gradient of this material was 0.66 V/µm, that was considerably higher compared to the sample bonded at 475 ºC (0.38 V/µm). This is because of the different characteristics of Ti_3Al that was formed at different bonding temperatures. Ti_3Al intermetallic is only a thin layer when bonded at 400 ºC (Fig. 4.9), and it becomes a layer when the

temperature increases to 475 ºC. For Ti/AZ91 (ST), the SPD and potential gradient were measured to be 0.75 V and 0.65 V/μm (Fig 5.5d), respectively. These values are similar to the values obtained from Ti/AZ80 (ST) bonded at the same temperature. Compared to the samples bonded at 475 ºC, these values were higher due to the formation of uniform Ti_3Al IMC layer when bonded at a high temperature of 475 ºC.

From the results shown in Fig. 5.4 and 5.5, it is concluded that an increase in Al content in Mg alloy decreases the SPD between pure Ti and Mg alloys. This is due to the formation of thick Al diffusion layer and continuous Ti_3Al intermetallic layer at the bonding interface.

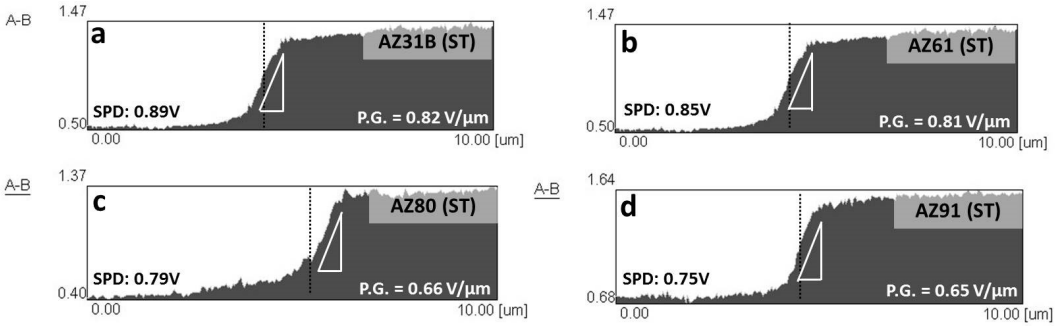

Fig. 5.5 Changes in surface potential measured across the bonding interface of a) Ti/AZ31B (ST), b) Ti/AZ61 (ST), c) Ti/AZ80 (ST), and d) Ti/AZ91 (ST) bonded at 400 ºC for 1 h under an applied pressure of 10 MPa.

5.3 Corrosion test of dissimilar materials in 5 wt% NaCl solution

5.3.1 Corroded surface of dissimilar materials

Figure 5.6 shows the bonding interface for Ti/Mg alloy (ST) bonded at 475 ºC for 1 h under an applied pressure of 10 MPa after corrosion test in 5 wt% NaCl solution. The corroded surface of Ti/AZ31B (ST) showed corrosion damage only on AZ31B (ST) side, and the surface of Ti was not corroded after corrosion test (Fig. 5.6a). The continuous layer of $Mg(OH)_2$ corrosion product was observed at the bonding interface of Ti/AZ31B (ST) after corrosion test. This corrosion product was a result from a galvanic corrosion between pure Ti and AZ31B (ST) which had surface potentials of 0.78 and 1.73 V, respectively. Figure 5.6b shows the corroded surface of Ti/AZ61 (ST) after corrosion test, where the damage on AZ61 (ST) side is less severe

compared to AZ31B (ST). This is attributed to the lower surface potential of AZ61 (ST) than that of AZ31B (ST). Their measured values are 1.70 and 1.73 V, respectively. The layer of corrosion product was observed in some areas at the bonding interface of Ti/AZ61 (ST). The Al content in Mg alloy plays an important role in the corrosion resistance of Mg alloys. The high Al content contributed to the formation of stable Mg-Al-O film. The Mg-Al-O film on the Mg alloy surface had higher potential in corrosion protection than $Mg(OH)_2$ film, which was generally formed on the Mg or Mg alloy surface. The corrosion damage (formation of $Mg(OH)_2$ layer) at the bonding interface of Ti/AZ61 (ST) was less severe compared to that of Ti/AZ31B (ST). This is explained by the lower SPD at the bonding interface of Ti/AZ61 (ST) than that of Ti/AZ31B (ST). The values for Ti/AZ31B (ST) are 0.78 and 0.81 V, respectively.

The corroded surface of Ti/AZ80 (ST) and Ti/AZ91 (ST) demonstrates corrosion damage in some areas on the Mg alloy side and at the bonding interface. These two bonding materials exhibit very good corrosion resistance compared to Ti/AZ31B (ST) and Ti/AZ61 (ST). The matrixes of AZ80 (ST) and AZ91 (ST) show a better corrosion resistance, because they possess lower surface potentials of 1.65 and 1.63 V, respectively. Moreover, the galvanic corrosion resistance of Ti/AZ80 (ST) and Ti/AZ91 (ST) are also superior compared to Ti/AZ31B (ST) and Ti/AZ61 (ST) because they possess low SPD of 0.75 and 0.72 V, respectively. These results also correspond well to their potential gradient (slope at the bonding interface) that the sample exhibited high potential gradient such as Ti/AZ31B (ST) and Ti/AZ61 (ST) with values of 0.77 and 0.71 V/μm show inferior galvanic corrosion resistance compared to Ti/AZ80 (ST) and Ti/AZ91 (ST) which possess relatively low potential gradient of 0.38 and 0.46 V/μm, respectively.

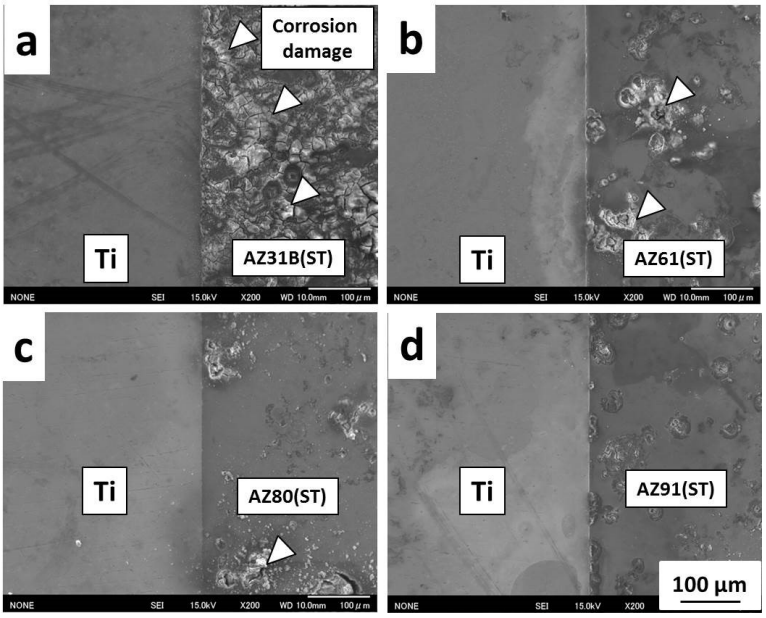

Fig. 5.6 Corroded surfaces of Ti/Mg alloys bonded at 475 ºC for 1 h after corrosion test in 5 wt% NaCl solution a) Ti/AZ31B (ST), b) Ti/AZ61B (ST), c) Ti/AZ80 (ST), and d) Ti/AZ91 (ST).

The formation of corrosion product during the corrosion test can be explained by the eq. 5.1-5.3 [105]. The anodic reaction is the rapid dissolution of the Mg when it is immersed in NaCl solution (eq. 5.1). The resulted Mg cations (Mg^{2+}) react with the hydroxyl group from cathodic reaction (eq. 5.2) and form the corrosion product of $Mg(OH)_2$ (eq. 5.3). This series of reactions is well-known for corrosion test of Mg alloys in NaCl solution. The amount of corrosion product appears after the corrosion test is considered to an indicator of the degree of corrosion.

$$Mg(s) \rightarrow Mg^{2+} + 2e^- \quad \text{(anodic reaction)} \qquad \text{(eq. 5.1)}$$

$$\tfrac{1}{2}O_2 + H_2O + 2e^- \rightarrow 2OH^-(aq) \quad \text{(cathodic reaction)} \qquad \text{(eq. 5.2)}$$

$$Mg^{2+}(aq) + 2OH^-(aq) \rightarrow Mg(OH)_2\,(s) \quad \text{(corrosion product)} \qquad \text{(eq. 5.3)}$$

Figure 5.7 shows the corroded surfaces of Ti/Mg alloys (ST) bonded at 400 ºC for 1 h. For Ti/AZ31B (ST), a severe corrosion damage was observed

on the matrix of the Mg alloy side, and a $Mg(OH)_2$ layer was observed at the bonding interface similar to Ti/AZ31B (ST) bonded at 475 ºC (Fig. 5.6a). The formation of Ti_3Al thin layer in Ti/AZ31B (ST) bonded at 475 ºC (Fig. 4.39) was not effective to improve the galvanic corrosion resistance, because the corroded surface of the samples bonded at 400 and 475 ºC are similar. This corresponds well to the SPD, where Ti/AZ31B (ST) bonded at 400 and 475 ºC shows similar values of 0.89 and 0.81 V, respectively. The surface potential gradient of Ti/AZ31B (ST) bonded at 400 ºC (0.82 V) is slightly higher than the sample bonded at 475 ºC (0.77 V), thus resulting in the similar corrosion characteristics at the bonding interface. The surface of Ti/AZ61 (ST) after the corrosion test shows a corrosion damage only on the Mg alloy side similar to the sample bonded at 475 ºC (Fig. 5.6b). However, a $Mg(OH)_2$ layer can be observed more easily in the sample bonded at 400 ºC in comparison with that bonded at 475 ºC. This is explained by the formation of Ti_3Al layer at the bonding interface. Namely, no Ti_3Al layer can be observed at the bonding interface of the sample bonded at 400 ºC, whereas a thin layer of Ti_3Al is observed in the sample bonded at 475 ºC. This is also confirmed by the SPD, where Ti/AZ61 (ST) that bonded at 400 ºC shows a higher SPD than that bonded at 475 ºC, corresponding to the values of 0.88 and 0.78 V, respectively.

For Ti/AZ80 (ST), the corrosion damage that appears on the Mg alloy side of the sample bonded at 475 ºC is similar to the sample bonded at 400 ºC. This is because the surface potential of both pure Ti and Mg alloy did not change with the bonding temperature changing from 400 to 475 ºC. However, a corrosion product layer that formed at the bonding interface of the sample bonded at 400 ºC in some areas can be barely observed in sample bonded at 475 ºC. The liquidation process taking place during SPS might facilitate the formation of Ti_3Al layer, and the existence of this layer thereafter improves the galvanic corrosion resistance of the sample bonded at 475 ºC (Fig. 5.6c). This is confirmed by the SPD measurement, where the potential gradient of Ti/AZ80 (ST) bonded at 475 ºC is found much lower than the sample bonded at 400 ºC, corresponding to the values of 0.38 and 0.66 V/μm, respectively.
The corroded surface of Ti/AZ91 (ST) bonded at 400 ºC shows a small corrosion damage on the Mg matrix, which is similar to the sample bonded at 475 ºC (Fig. 5.7d). In fact, Ti/AZ91 (ST) exhibits the best corrosion resistance among all the Mg alloys on the Mg matrix, as well as at the

bonding interface. This is because of its highest Al content. The uniform and continuous Ti_3Al layer formed at the bonding interface of Ti/AZ91 (ST) bonded at 475 ºC (Fig. 4.40) resulted in a superior galvanic corrosion resistance compared to the sample bonded at 400 ºC, in which $Mg(OH)_2$ layer was barely observed (Fig. 5.7d). The galvanic corrosion resistance of Ti/AZ91 (ST) bonded at 475 ºC was confirmed by SPD that it shows the lowest SPD among the bonded materials of 0.72 V with low potential gradient of 0.46 V/μm. This result indicates that Ti/AZ91 (ST) bonded at 475 ºC possesses the best corrosion resistance on the Mg matrix and at the bonding interface compared to other bonded materials. From these results, it can be concluded that the formation of a uniform Al diffusion and Ti_3Al layer at the bonding interface is effective to improve the galvanic corrosion resistance of bonded materials [106]. This Al diffusion layer and Ti_3Al formation could lower the SPD and potential gradient at the bonding interface, resulted in an improvement of galvanic corrosion resistance.

Figure 5.8 shows the SEM-EDS analysis of the corroded surface for Ti/AZ91 (ST) bonded at 400 and 475 ºC for 1 h. The sample bonded at 400 ºC showed a $Mg(OH)_2$ layer at the bonding interface in secondary electron (SE) image (Fig. 5.8a). The mapping of oxygen on the right side shows a high oxygen content layer at the same area as the corrosion product layer. The high oxygen content areas (white area) were also observed on the Mg alloy matrix at the corroded area in which $Mg(OH)_2$ exists. Ti/AZ91 (ST) bonded at 475 ºC showed some corroded areas at the bonding interface and on the Mg alloy matrix (Fig. 5.8b) in the SE image. The mapping image of oxygen shows the high oxygen content area at the bonding interface and on the Mg alloy matrix that was corroded similar to the sample bonded at 400 ºC. This result confirms the location of corrosion product or $Mg(OH)_2$ at the bonding interface after corrosion test. Ti/AZ91 (ST) bonded at 475 ºC showed high oxygen content in a few areas at the bonding interface which implies that it possesses higher galvanic corrosion resistance than the sample bonded at 400 ºC due to the formation of the continuous and uniform Ti_3Al layer. The corrosion characteristics on the Mg alloy matrix between samples bonded at 400 and 475 ºC are similar because the surface potential of Mg alloy was not changed after SPS.

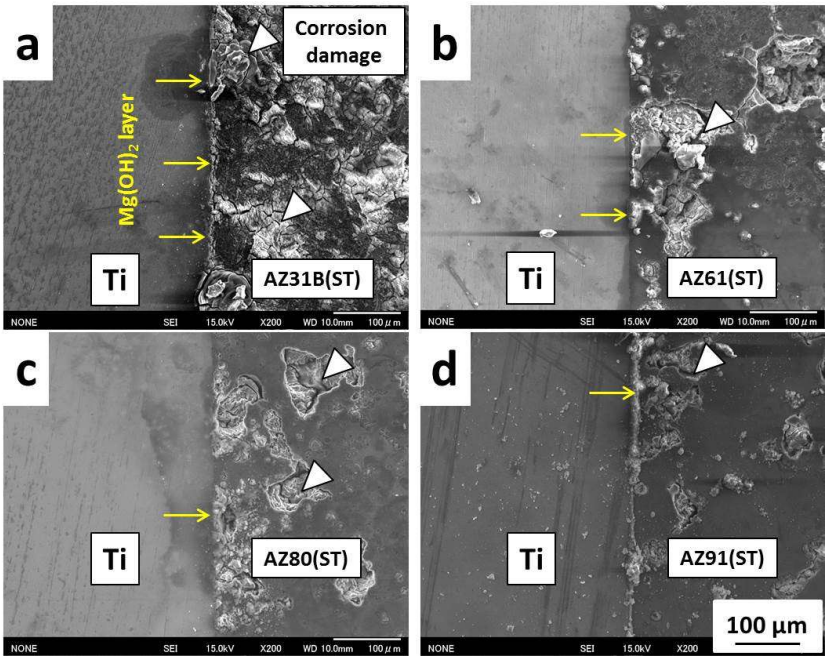

Fig. 5.7 Corroded surfaces of Ti/Mg alloys bonded at 400 ºC for 1 h after corrosion test in 5 wt% NaCl solution a) Ti/AZ31B (ST), b) Ti/AZ61 (ST), c) Ti/AZ80 (ST), and d) Ti/AZ91 (ST).

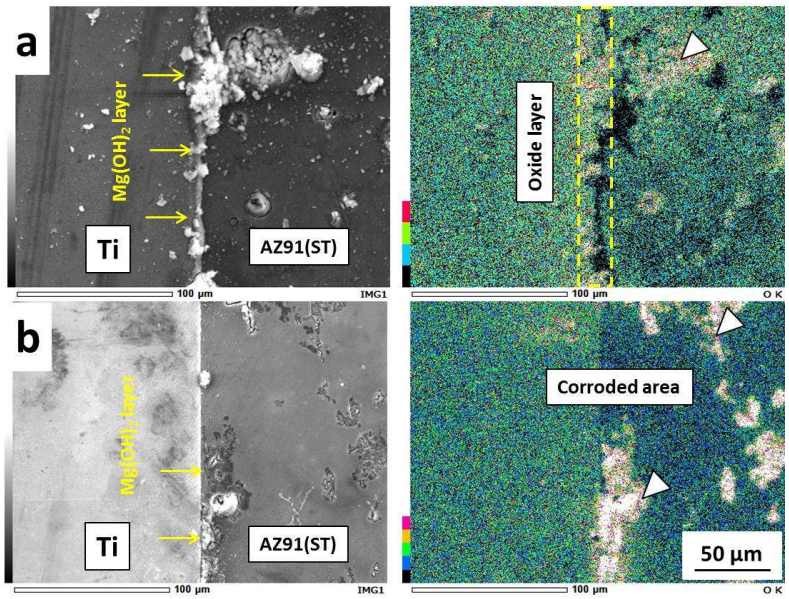

Fig. 5.8 SEM-EDS analysis of Ti/AZ91 (ST) bonded at a) 400 ºC and b) 475 ºC for 1 h after corrosion test in 5 wt% NaCl solution.

Figure 5.9 shows the corroded surfaces on the Mg alloy (ST) side of the samples bonded at 400 ºC for 1 h after immersed in 5 wt% NaCl solution. The surface of AZ31B (ST) that possesses the highest surface potential (1.73 V) shows a severe corroded damage by NaCl solution. The corrosion product or $Mg(OH)_2$ can be observed in a white area that spreads throughout the Mg alloy matrix (Fig. 5.9a). It is shown that only sporadic areas were not damaged after the corrosion test. Cracks can also be observed near an agglomeration area of $Mg(OH)_2$ due to corrosion damage.

For Ti/AZ61 (ST), the surface on the Mg alloy side was suffered from smaller corrosion damage with a smaller $Mg(OH)_2$ agglomeration area than that for AZ31B (ST) (Fig. 5.9b). However, many white particles on the corroded surface of AZ61 (ST) easily observed and represented active areas for corrosion. These areas having the small $Mg(OH)_2$ particles can enlarge if the immersion time in NaCl solution increases. The crack holes indicated by red arrows can be observed on the corroded surface. These crack holes were caused by the detachment of the corrosion product from Mg alloy matrix. The corrosion damage on AZ61 (ST) surface is smaller than that on AZ31B (ST) surface and corresponds well to the surface potential, where the surface potential of AZ61 (ST) is lower than that of AZ31B (ST) with the values of 1.70 and 1.73 V, respectively.

The corroded surface of AZ80 (ST) shows a smaller corrosion damage than that of AZ61 (ST) with a decrease in agglomeration areas of $Mg(OH)_2$ (Fig. 5.9c). Furthermore, the small $Mg(OH)_2$ particles observed in AZ61 (ST) cannot be observed in AZ80 (ST). This implies that the corrosion resistance of AZ80 (ST) is superior compared to AZ61 (ST). The improvement in corrosion resistance in AZ80 matrix is explained by the surface potential of AZ80 (ST) which is lower than that of AZ61 (ST).

The surface of AZ91 (ST) exhibits the best corrosion resistance on the matrix among all the Mg alloys (ST), where it showed only a few areas of $Mg(OH)_2$ agglomeration. A large amount of small crack holes were observed on the AZ91 (ST) surface, which were caused by the detachment of the small $Mg(OH)_2$ particles at the agglomeration area. The detachment of the $Mg(OH)_2$ particles in a small corrosion area on the AZ80 (ST) and AZ91 (ST) surface occurred easier than in the large corrosion area on the AZ31B (ST) and AZ61 (ST) surface. This high corrosion resistance property of AZ91 (ST) corresponds well to its surface potential, where AZ91 (ST) showed the lowest

surface potential (least susceptible to corrosion) among all the applied Mg alloys to be a value of 1.63 V.

It can be concluded from these results that increasing the Al content in Mg alloys can improved not only the galvanic corrosion resistance at the bonding interface but also the corrosion resistance of the Mg alloy matrix by lowering the surface potential.

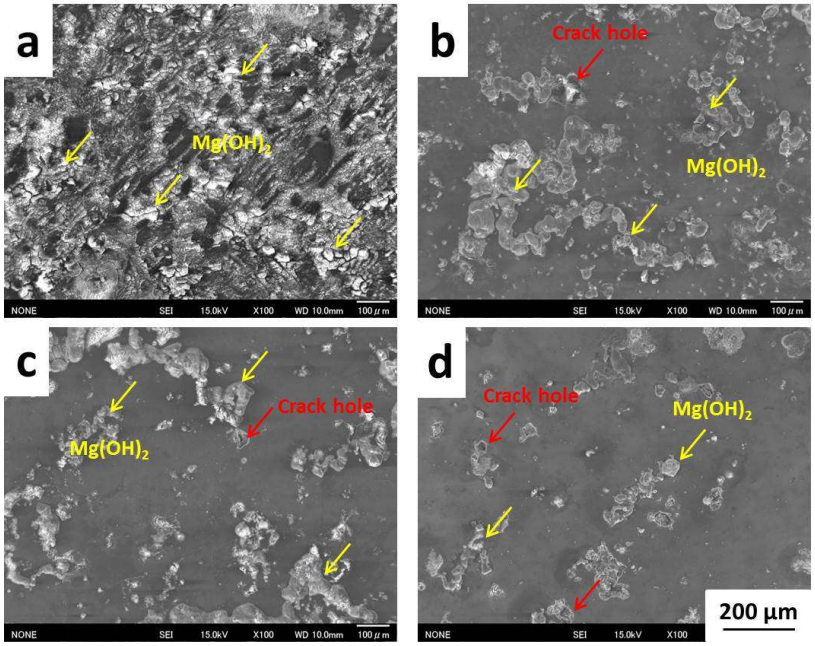

Fig. 5.9 Corroded surfaces on Mg alloys side of sample bonded at 400 ºC for 1 h a) Ti/AZ31B (ST), b) Ti/AZ61 (ST), c) Ti/AZ80 (ST), and d) Ti/AZ91 (ST).

As shown in Fig 5.10**,** the corroded surfaces on Mg alloy side of Ti/Mg alloy (ST) bonded at 475 ºC for 1 h also confirmed that the surface potential of each Mg alloy did not change with the bonding temperature. For Ti/AZ31B (ST) bonded at 475 ºC, its corroded surface was similar to the sample bonded at 400 ºC, where the large $Mg(OH)_2$ agglomeration areas were observed throughout the matrix with only few non-corroded areas left (Fig 5.10a). This $Mg(OH)_2$ agglomeration areas were decreased when the Al content in the Mg alloy was increased to 5.5 wt% (Fig. 5.10b). However, small $Mg(OH)_2$ particles on susceptible areas were still observed throughout the AZ61 (ST) surface agree with that of the sample bonded at 400 ºC (Fig. 5.9b). For Ti/AZ80 (ST), the $Mg(OH)_2$ agglomeration area on its surface was

smaller than that of AZ61 (ST), agreeing with the sample bonded at 475 ºC (Fig. 5.10c). Small particles of $Mg(OH)_2$ were found disappeared from the matrix when the Al content in the Mg alloy reached 7.8 wt%. For the sample bonded at 475 ºC, the best corrosion resistance on the matrix was also obtained for AZ91 (ST) in agreement with the sample bonded at 400 ºC due to the similar corroded characteristics (Fig. 5.10d). Nevertheless, many small crack holes were still observed in this sample due to the detachment of the $Mg(OH)_2$ corrosion product. This result indicates that a change of the bonding temperature has no effect on the surface potential of Mg alloys because their corroded surfaces show the same characteristics.

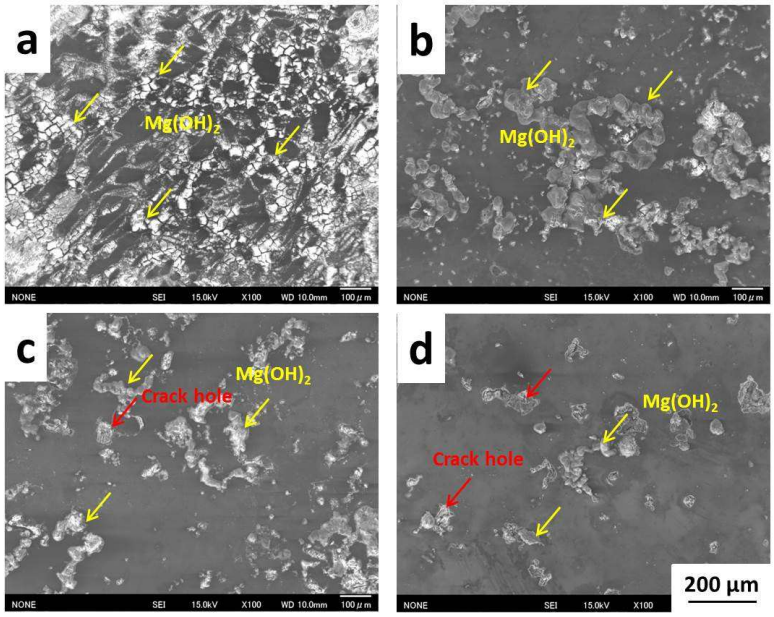

Fig. 5.10 Corroded surfaces on Mg alloys side of sample bonded at 475 ºC for 1 h a) Ti/AZ31B (ST), b) Ti/AZ61 (ST), c) Ti/AZ80 (ST), and d) Ti/AZ91 (ST).

The formation of intermetallic Ti_3Al layer plays a key role not only in the bonding strength of Ti/Mg alloy (ST) dissimilar materials, but also in the galvanic corrosion resistance of the bonding interface in NaCl solution. It is found that this intermetallic layer can improve the life span of the bonded materials between pure Ti and Mg alloys (ST). The existence of the Ti_3Al layer prevents a large and immediate change in surface potential at the bonding interface by creating a potential gradient. This has been confirmed

to play a significant role in reducing the galvanic corrosion damage at the bonding interface, where the disappearance of $Mg(OH)_2$ agglomeration layer was observed.

5.4 Corrosion test of dissimilar materials in Kroll's etchant

In order to further study the corrosion behavior of Ti/Mg alloy (ST) dissimilar materials, the bonded samples were also tested in Kroll's etchant ($HF:HNO_3:H_2O$ = 1:5:100 in volume ratio). The samples were immersed in Kroll's etchant for 2 min at room temperature without applying magnetic stirrer, and then the surface profile of the bonded samples was studied. This method was used to evaluate the galvanic corrosion at the bonding interface and corrosion in Mg alloy (ST) matrix. The surface of the bonded samples was prepared by the same process used for the samples immersed in 5 wt% NaCl solution, and the prepared surface is shown in Fig. 5.1.

Figure 5.11 shows the surface profiles of the bonded samples before corrosion test which were observed by surface analysis microscope. Both pure Ti and Mg alloys (ST) showed smooth surface after polishing, and the surface level of Mg alloy (ST) was slightly lower than the surface of Ti with a value of 5.7 μm (Fig. 5.12a). This is because the hardness or wear resistance of Mg alloy (ST) is lower than that of Ti, hence resulting in an easy loss in material during grinding or polishing. The surface of Ti and Mg alloys was rather uniform that Ti side showed a green color and Mg alloy (ST) side showed a purple color (Fig. 5.11b). These surface profiles were observed in all bonded materials that bonded at 400 and 475 ºC.

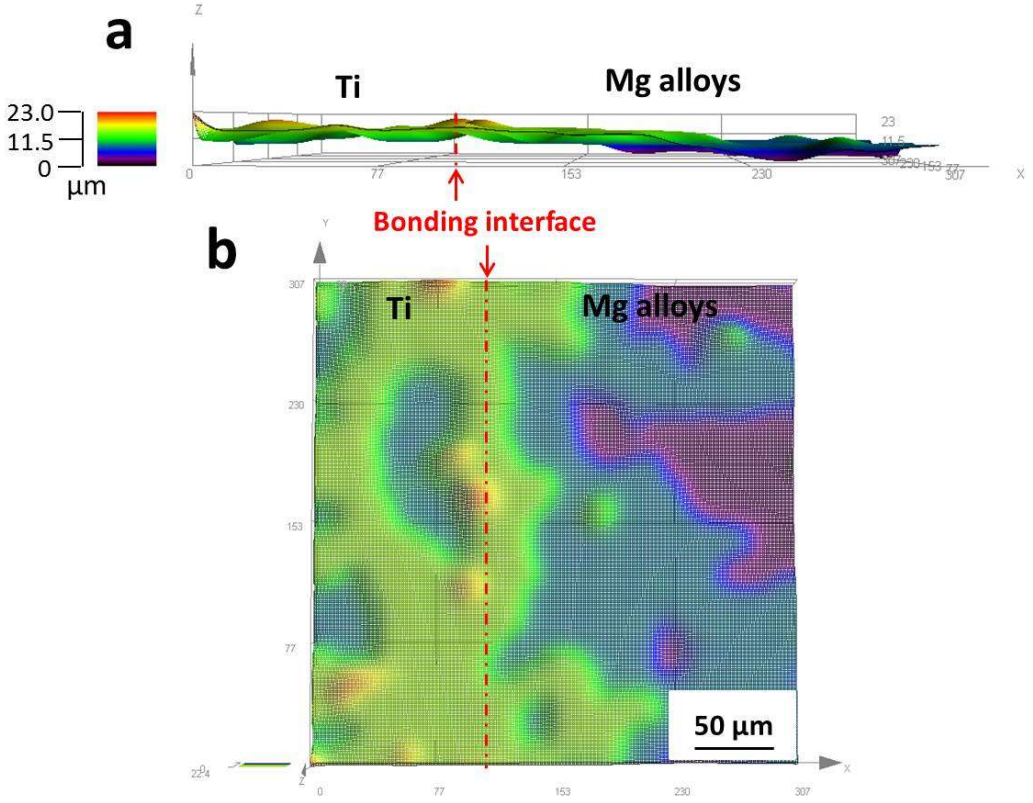

Fig. 5.11 Surface profiles of Ti/Mg alloy (ST) dissimilar material after polishing a) Side view and b) Top view.

5.4.1 Corroded surface of dissimilar materials

Figure 5.12 demonstrates the bonding interface of the samples after corrosion in Kroll's etchant for 2 min. The corrosion product or $Mg(OH)_2$ agglomeration layer was not observed on the sample that was immersed in this solution, which is different from the sample immersed in 5 wt% NaCl solution. This may be caused by a strong corrosion reaction in Kroll's etchant where a large amount of hydrogen bubbles were emitted from the sample surface. As a consequence, the corrosion product was detached instantly from the corroded surface during the corrosion test, which therefore resulted in a clean surface after the corrosion test. This occurred in all of the samples that were bonded at 400 and 475 ºC. The corroded interface observed by SEM was similar for all bonded materials, but the surface profile after corrosion test was different for them. This will be discussed later in next section.

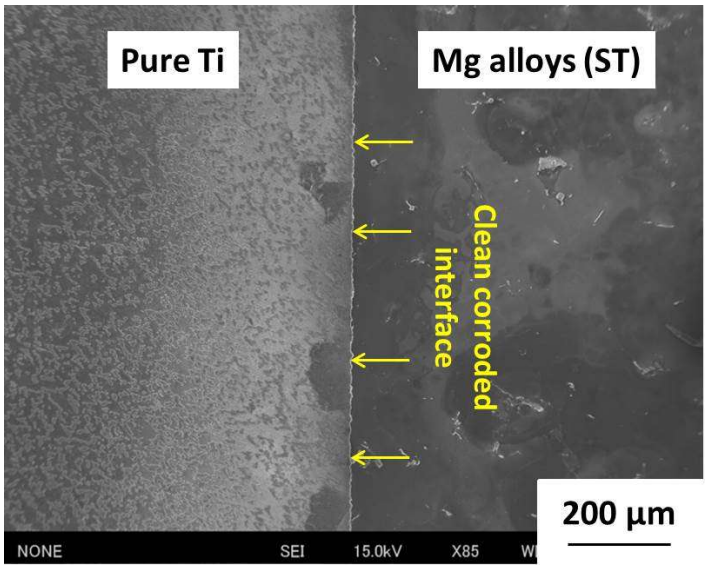

Fig. 5.12 Corroded surface of Ti/Mg alloy (ST) dissimilar material after immersed in Kroll's etchant for 2 min.

Figure 5.13 shows the corroded surfaces on the Mg alloy (ST) side of Ti/Mg alloy (ST) bonded materials bonded at 475 ºC for 1 h. AZ31B (ST) which possessed the highest surface potential of 1.73 V showed much more severe corrosion damage than the other bonded materials, in agreement with the bonded samples tested in 5 wt% NaCl solution (Fig. 5.13a). The black area near the pitting corrosion damage was an area that suffered more corrosion, and had a lower surface level than the adjacent area (grey area). Many large pitting corrosion areas were observed throughout the corroded surface. AZ61 (ST) which possessed a lower surface potential than AZ31B (ST) showed less severe damage than AZ31B (ST), and the pitting corrosion area was also smaller (Fig. 5.13b). This indicates that corrosion resistance of AZ61 (ST) is superior compared to AZ31B (ST), and the results correspond to those tested in 5 wt% NaCl solution. For AZ80 (ST), the amount of small pitting corrosion area decreased compared to AZ61 (ST) because the surface potential of AZ80 (ST) is lower than that of AZ61 (ST). The black or deeply corroded area was barely observed in AZ80 (ST) (Fig. 5.13c), which indicated that the corrosion resistance of the sample was improved compared to AZ61 (ST). AZ91 (ST) showed superior corrosion resistance compared to the other Mg alloys, and therefore the pitting corrosion damage was barely observed on its corroded surface. However, the

deeply corroded areas were still observed in many locations because of the strong acidic characteristics of the Kroll's etchant. Similar to the sample bonded at 475 ºC, the same corroded characteristics was observed in the sample bonded at 400 ºC for all the Mg alloys. This result agrees with the samples tested in 5 wt% NaCl solution, where the corroded characteristics of Mg alloy (ST) surface did not change with the bonding temperature.

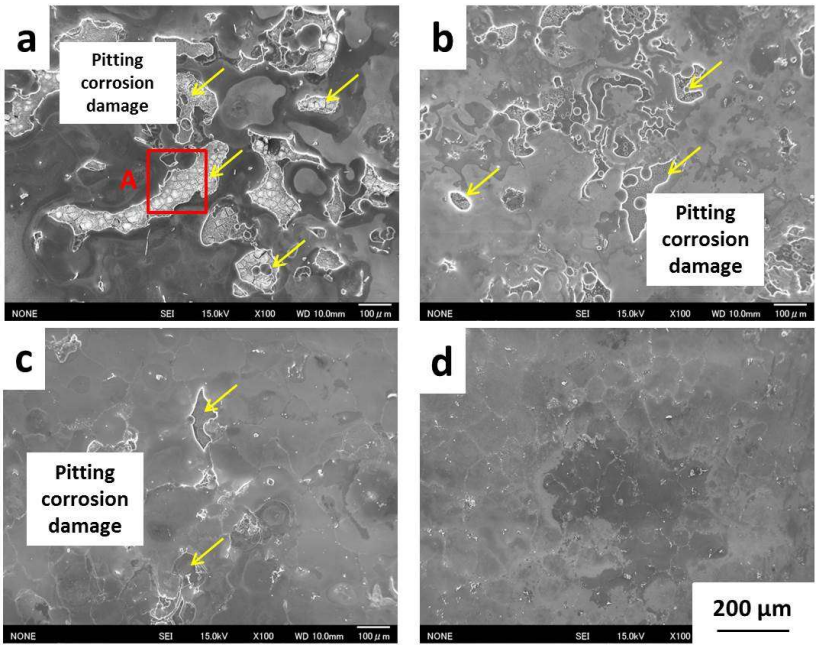

Fig. 5.13 Corroded surfaces on Mg alloys (ST) side of Ti/Mg alloy (ST) dissimilar materials bonded at 475 ºC for 1 h a) AZ31B (ST) b) AZ61 (ST) c) AZ80 (ST) and d) AZ91 (ST).

Figure 5.14 shows the result of SEM-EDS analysis of area A in Fig. 5.13a, where the pitting corrosion was observed. The formation of $Mg(OH)_2$ was observed at the pitting corrosion area, but an agglomeration of $Mg(OH)_2$ was not observed due to the detachment from the corroded surface, which was caused by the formation and emission of a large amount of hydrogen bubbles from the surface during corrosion test. The existence of $Mg(OH)_2$ was also confirmed by the oxygen and magnesium mapping images (Fig. 5.14b and 5.14c), where shows high oxygen and low magnesium contents at the pitting corrosion area.

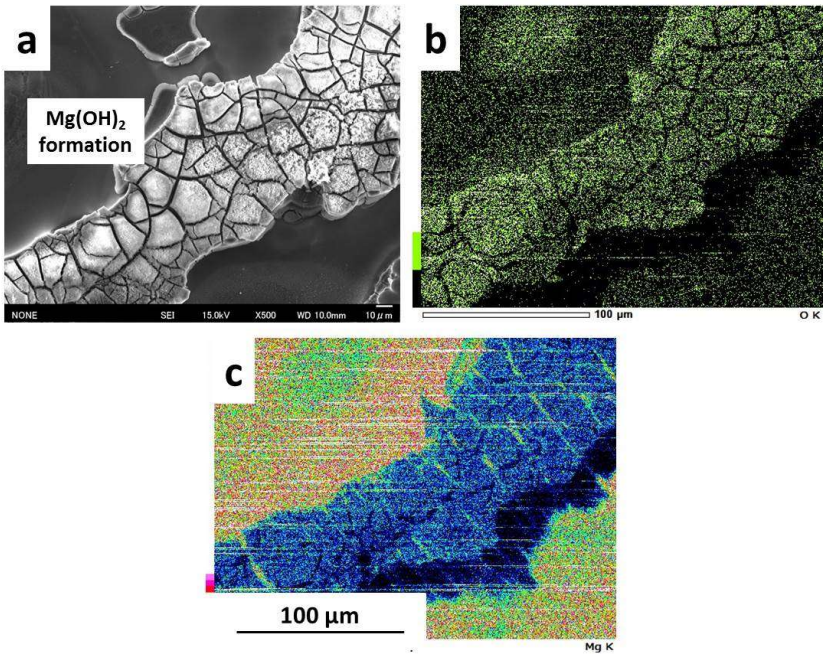

Fig. 5.14 SEM-EDS analysis of area A in Fig. 5.14a a) SE image, b) Oxygen mapping, and c) Magnesium mapping.

5.4.2 Surface profile of dissimilar materials after corrosion test

Figure 5.15 shows the surface profiles of the Ti/Mg alloy (ST) materials bonded at 400 ºC for 1 h after corrosion tests. The position of the bonding interface (B.I.) was indicated by a red line in the figure. The surface profile of Ti/AZ31B (ST) after corrosion test showed a smooth surface on the pure Ti side because it had only smaller corroded damage as observed in Fig. 5.12. Besides, the surface level of Ti after corrosion test was similar to that before corrosion test. However, the surface level was suddenly changed at the bonding interface with a height of 42 µm by the galvanic corrosion between the Ti and AZ31B (ST). The corroded surface on the AZ31B (ST) side was uniform with a large corrosion depth (Fig. 5.15a). From the microstructure at the bonding interface of Ti/AZ31B (ST), there was no formation of Ti_3Al layer except a thin Al diffusion layer, and this resulted in a poor galvanic corrosion between Ti and AZ31B (ST) with a high SPD value of 0.89 V. Figure 5.15b shows the surface profile of Ti/AZ61 (ST) after corrosion test, where a corrosion depth of 28 µm was measured at the bonding interface. It was a smaller value than that observed in Ti/AZ31B (ST), which showed a corrosion depth of 42 µm at the bonding interface.

This indicates that the galvanic corrosion of Ti/AZ61 (ST) was superior compared to Ti/AZ31B (ST) due to a decrease in SPD value from 0.89 to 0.85 V. Ti/AZ80 (ST) exhibited a comparable corrosion depth to Ti/AZ61 (ST) with a very different characteristics (Fig. 5.15c). The corroded surface level was gradually decreased from the Ti to AZ80 (ST) side, instead of an abrupt decrease shown in Ti/AZ61 (ST). This can be explained by the formation of Ti_3Al and the thick Al diffusion layer at the bonding interface, which resulted in a low SPD value of 0.79 V. The corrosion depth at the bonding interface was further decreased to 21.5 μm for Ti/AZ91 (ST), and a surface slope at the bonding interface was lower than that for Ti/AZ80 (ST) (Fig. 5.15d). This corresponds well to the decrease of SPD value and potential gradient of Ti/AZ91 (ST) compared to Ti/AZ80 (ST) with values of 0.75 V and 0.65 V/μm, respectively. From these results, it can be concluded that Ti/AZ91 (ST) exhibits the best galvanic corrosion resistance among all of the bonded materials bonded at 400 ºC for 1 h.

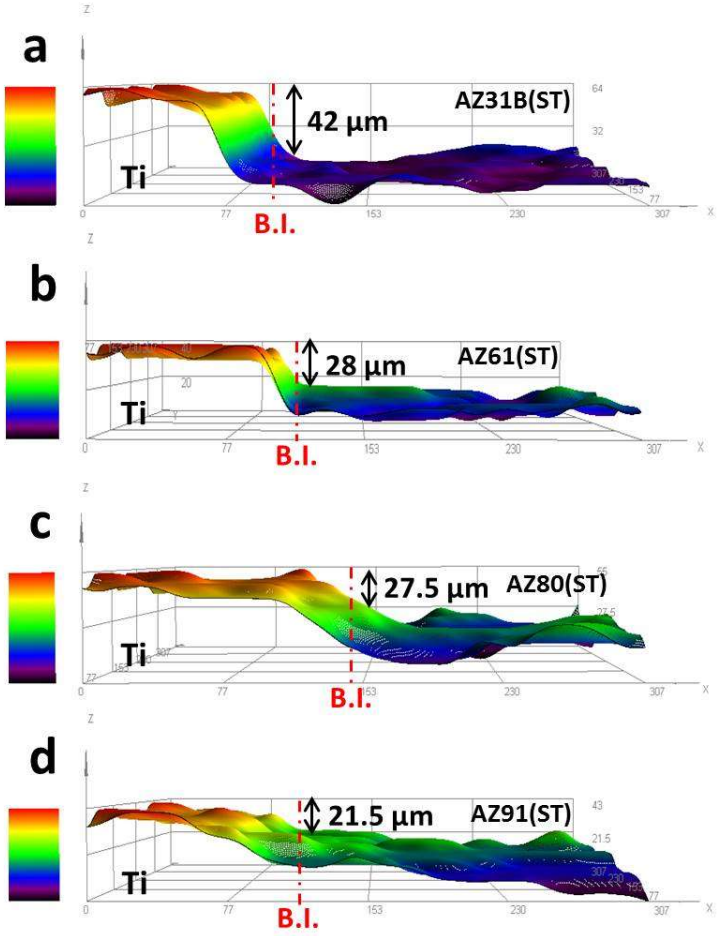

Fig. 5.15 Surface profiles of sample bonded at 400 ºC for 1 h after corrosion tests a) Ti/AZ31B (ST), b) Ti/AZ61 (ST), c) Ti/AZ80 (ST), and d) Ti/AZ91 (ST).

Figure 5.16 shows the surface profiles of the Ti/Mg alloy (ST) bonded materials bonded at 475 ºC for 1 h after corrosion tests. The corrosion depth at the bonding interface of Ti/AZ31B (ST) was 37 µm (Fig. 5.16a), which is lower than the sample bonded at 400 ºC. Yet, their corrosion characteristics were similar, where the surface level was suddenly decreased from pure Ti to the AZ31B (ST) side. This implies that the galvanic corrosion resistance of Ti/AZ31B (ST) was inferior compared to the other bonded materials because the Ti_3Al layer was barely observed at the bonding interface even while applying the high bonding temperature of 475 ºC. This resulted in a high SPD value of 0.81 V. For Ti/AZ61 (ST), the corrosion depth at the bonding interface was similar to the sample bonded at 400 ºC, but the characteristics

of corrosion was changed, where a slope appeared at the bonding interface (Fig. 5.16b). This indicates that the galvanic corrosion resistance of Ti/AZ61 (ST) bonded at 475 ºC was superior compared to the sample bonded at 400 ºC due to the formation of Ti_3Al layer in many areas at the bonding interface when applying the bonding temperature at 475 ºC, resulted in a decrease in SPD value. For Ti/AZ80 (ST), the corrosion depth at the bonding interface has a value of 25 μm, which is lower than to the sample bonded at 400 ºC. However, the characteristics of corrosion was similar where a surface level was gradually decreased from pure Ti to the AZ80 (ST) side (Fig. 5.16c). This implies that the galvanic corrosion resistance of Ti/AZ80 (ST) bonded at 475 ºC was superior compared to the sample bonded at 400 ºC with a decrease in the SPD value from 0.79 to 0.75 V.

Similar to Ti/AZ80 (ST), Ti/AZ91 (ST) bonded at 475 ºC shows a decrease of the corrosion depth at the bonding interface from 21.5 to 19 μm compared to the sample bonded at 400 ºC with the same charecteristic of corrosion (Fig. 5.16d). It also showed the lowest corrosion depth at the bonding interface among all the bonded materials due to the lowest SPD value of 0.72 V, which represented the best galvanic corrosion resistance among the bonded materials. These results were similar to the samples tested in 5 wt% NaCl solution, where Ti/AZ91 (ST) also showed the best galvanic corrosion resistance. The corroded surface level of pure Ti did not changed very much after the corrosion test as shown in Fig 5.16 and 5.17, while most of the corrosion occurred on the Mg alloy (ST) side.

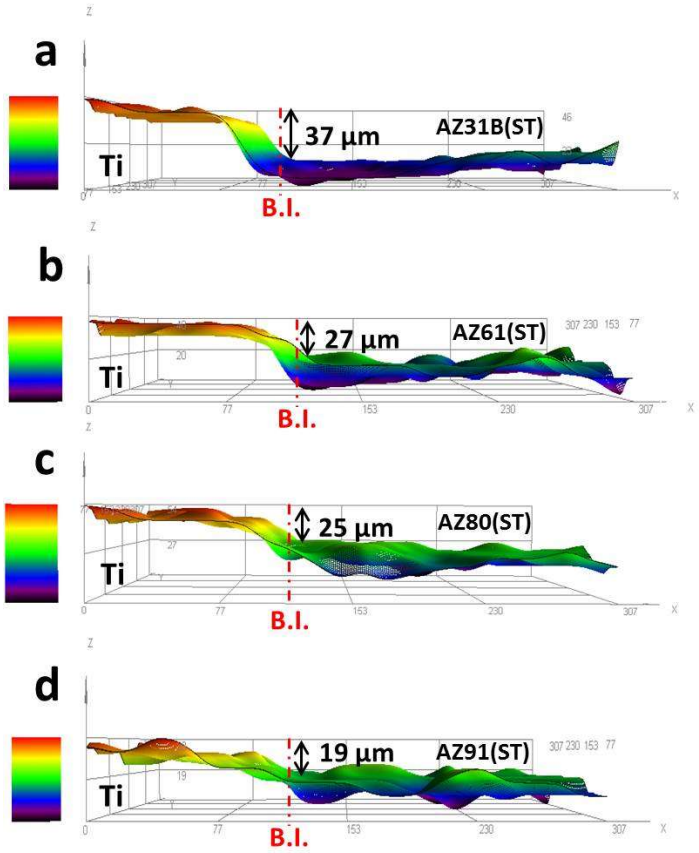

Fig. 5.16 Surface profiles of sample bonded at 475 ºC for 1 h after corrosion tests a) Ti/AZ31B (ST), b) Ti/AZ61 (ST), c) Ti/AZ80 (ST), and d) Ti/AZ91 (ST).

Figure 5.17 shows the line profiles of the surface after corrosion for all the Ti/Mg alloy (ST) materials bonded at 475 ºC for 1 h. From this result, the galvanic corrosion between pure Ti and Mg alloys (ST) was confirmed by the characteristics of the plot line, where a surface level of Mg alloy (ST) near the bonding interface was much lower than the other areas far from it. The galvanic depth (G.D.) and galvanic width (G.W.) were measured to evaluate the extent of galvanic corrosion in each sample. For Ti/AZ31B (ST), the high G.W. and G.D. values up to 510.1 and 29.8 µm were measured, respectively. The large gap between Ti and AZ31B (ST) caused by galvanic corrosion was clearly observed (Fig. 5.17a). The surface of Ti was still uniform after corrosion test, and thus confirmed that the corrosion mostly occurred on the Mg alloy (ST) surface. These results also correspond to the SPD value between Ti and AZ31B (ST) which was the highest among all the

bonded materials. The G.D. and G.W. values were decreased for Ti/AZ61 (ST) compared to Ti/AZ31B (ST) with values of 30.7 and 457.4 μm, respectively (Fig. 5.17b). The gap between pure Ti and Mg alloy (ST) surface was considerably decreased compared to Ti/AZ31B (ST). This is explained by the formation of uniform Ti_3Al and thick Al diffusion layer at the bonding interface, resulting in a reduction in SPD value between the pure Ti and Mg alloy (ST). The thickness of Ti_3Al and Al diffusion layer was in a nano-level but they were able to inhibit a progress of galvanic corrosion from bonding interface to the distant area [108]. The G.D. and G.W. were further decreased in Ti/AZ80 (ST) with values of 26.5 and 346.1 μm, respectively (Fig. 5.17c). This referred to an improvement of galvanic corrosion resistance in Ti/AZ80 (ST) compared to Ti/AZ61 (ST) with the decrease of SPD. Ti/AZ91 (ST) exhibited the lowest G.D. and G.W. values of 19.1 and 281.5 μm, respectively. The gap between the pure Ti and Mg alloy (ST) was much smaller than the other bonded materials. The formation of thick and continuous Ti_3Al layer plays an impotant role in the improvement of galvanic corrosion resistance in this sample. These results also correspond well to the surface profiles of Ti/Mg alloy (ST) bonded at 475 ºC after corrosion (Fig. 5.16).

Figure 5.18 shows the line profiles of the Ti/Mg alloy (ST) surface bonded at 400 ºC for 1 h after corrosion. Ti/AZ31B (ST) bonded at 400 ºC showed G.D. and G.W. values of 44 and 633.3 μm (Fig. 5.18a), respectively. These values were larger than those for Ti/AZ31B (ST) that bonded 475 ºC. This implies that the galvanic corrosion occurred at the bonding interface of the sample bonded at 400 ºC was more severe than that of the sample bonded at 475 ºC. This is explained by the increase of the thickness of Al diffusion layer and the formation of Ti_3Al intermetallic layer in the sample bonded at 475 ºC, which resulted in a decrease in the potential gradient (P.G.) from 0.82 to 0.77 V/μm. Ti/AZ61 (ST) also showed decreased G.D. and G.W. when the bonding temperature was increased to 475 ºC (Fig. 5.18b). The decrease of these values is due to the same reason as that explained for Ti/AZ31B (ST). Great improvement in galvanic corrosion resistance was obtained for Ti/AZ80 (ST) when increasing bonding temperature to 475 ºC, where G.D. and G.W. values decreased from 36.4 and 539.5 μm to 26.5 and 346.1 μm, respectively (5.18c). This is explained by the formation of continuous Ti_3Al layer at 475 ºC, and the decrease of P.G. from 0.66 to 0.38

V/μm. For Ti/AZ91 (ST), the decrease of G.D. and G.W. values was small in comparison with the other dissimilar materials due to the slight difference in the characteristics of the bonding interface between the samples bonded at 400 and 475 ºC (5.18d). These bonded samples showed the best galvanic corrosion resistance among dissimilar materials.

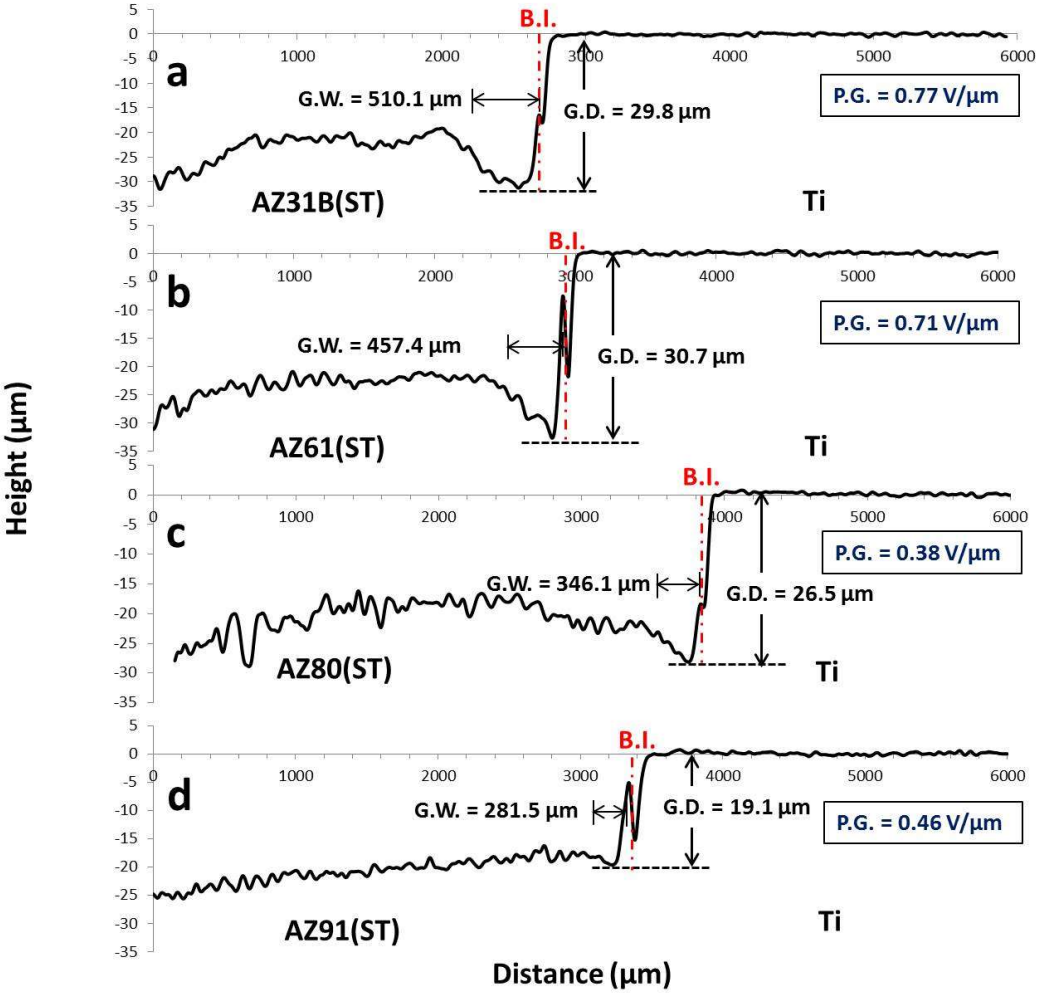

Fig. 5.17 Line profiles of dissimilar materials bonded at 475 ºC for 1 h after corrosion test a) Ti/AZ31B (ST), b) Ti/AZ61 (ST), c) Ti/AZ80 (ST), and d) Ti/AZ91 (ST).

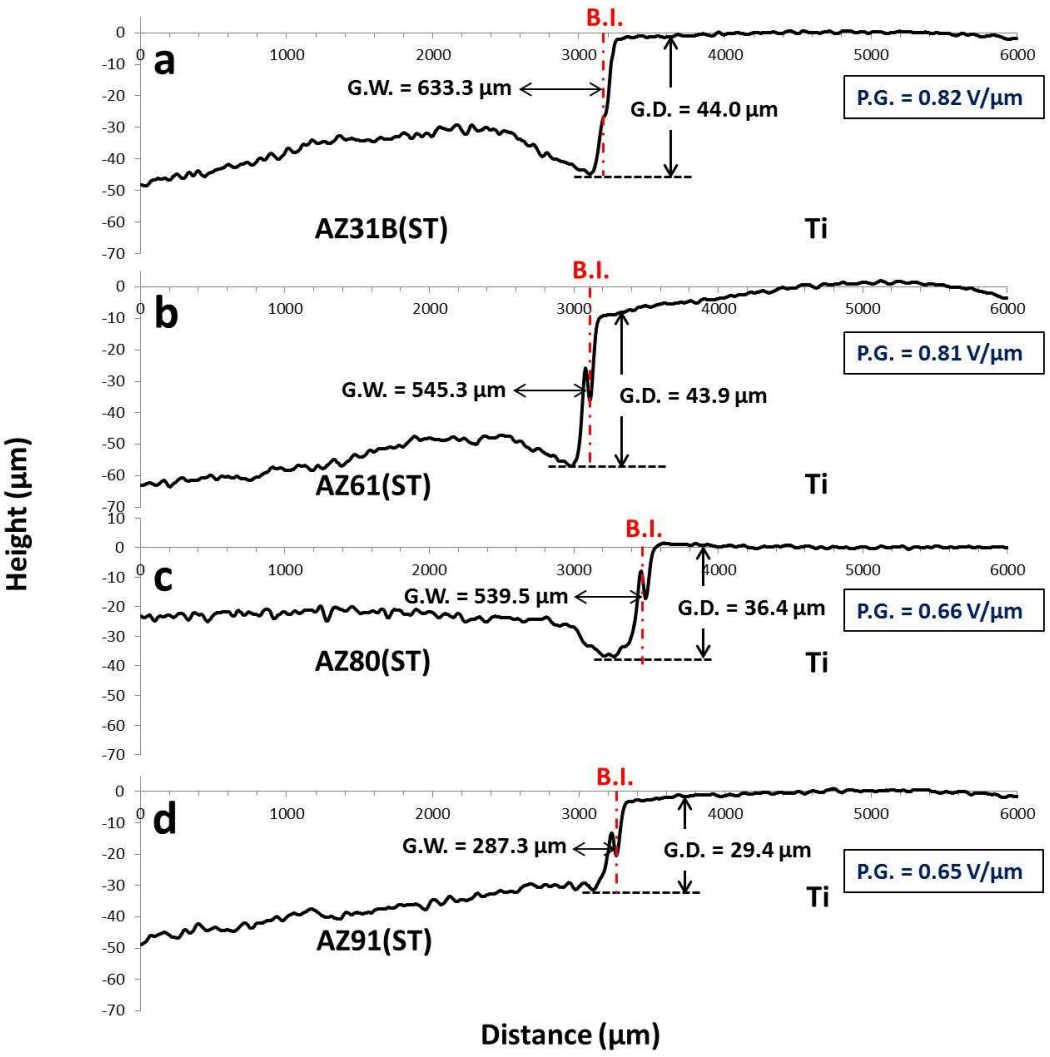

Fig. 5.18 Line profiles of dissimilar materials bonded at 400 ºC for 1 h after corrosion test a) Ti/AZ31B (ST), b) Ti/AZ61 (ST), c) Ti/AZ80 (ST), and d) Ti/AZ91 (ST).

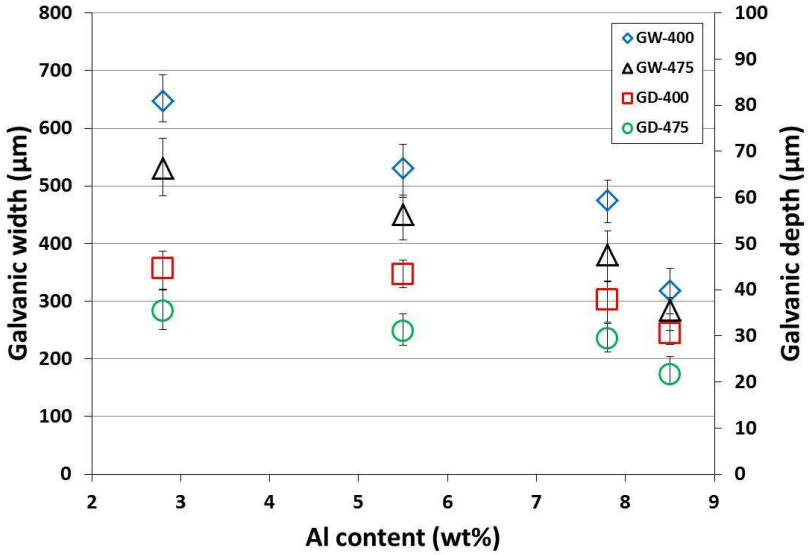

Fig. 5.19 Relationship between galvanic width (G.W.), galvanic depth (G.D.) and Al content in Mg alloys (ST).

Fig. 5.19 shows the relationship between galvanic parameters and Al content in Mg alloys (ST) of sample bonded at 400 and 475 ºC. For Ti/Mg alloys (ST) bonded at 400 ºC, both G.W. and G.D. are decrease when Al content in Mg alloys (ST) is increase which represent an improvement of galvanic corrosion resistance. Ti/Mg alloys (ST) bonded at 475 ºC shows the similar characteristic to sample bonded at 400 ºC. However, G.W. and G.D. of sample bonded at 475 ºC are lower than 400 ºC because a formation of continuous and thick Ti_3Al layer which greatly decrease P.G. at the bonding interface.

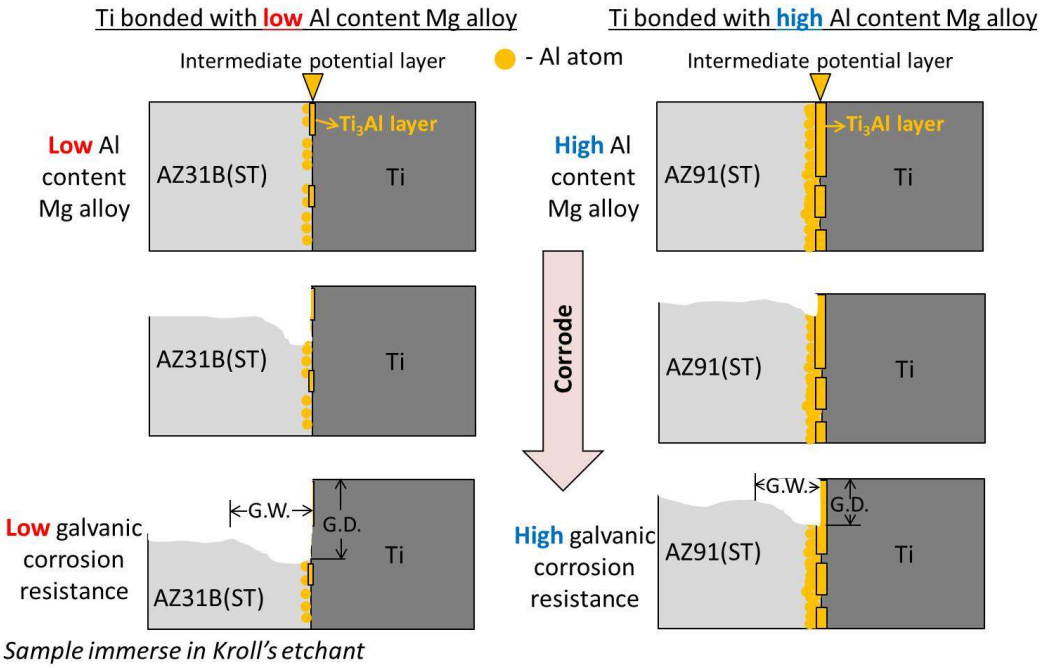

Fig. 5.20 Schematic illustration of corrosion mechanism in Kroll's etchant.

Figure 5.20 shows schematic illustration of corrosion mechanism in Kroll's etchant comparing between pure Ti bonded to low and high Al content Mg alloys (ST). For pure Ti bonded to low Al content Mg alloys (ST) such as AZ31B (ST), thin diffusion layer is usually formed at the bonding interface because low Al content and result in formation of thin and short Ti_3Al layer. This characteristic at the bonding interface results in a small decrease in P.G. at the bonding interface which is not effective in improvement of galvanic corrosion resistance. On the other hand, pure Ti bonded to high Al content Mg alloys (ST) such as AZ91 (ST), the thick diffusion layer of Al and continuous Ti_3Al layer can be formed at the bonding interface. The Al atom can decreases a surface potential in a small value as the surface potential of Mg alloys decreases when Al content is increases. Moreover, a large decrease in surface potential can be obtained by a formation of Ti_3Al layer which possesses a much lower surface potential than Mg alloys of 1.02 V. This characteristic at the bonding interface results in a large decrease in P.G. and results in a great improvement in galvanic corrosion resistance.

5.5 Conclusion

In this research, the corrosion resistance has been found increasing with the Al content in Mg alloy (ST) matrix. This is because an increase of Al content decreases the surface potential of the Mg alloys due to the formation of stable Mg-Al-O film, which is more effective in preventing from corrosion than $Mg(OH)_2$ film. The improvement in corrosion resistance of the Mg alloy matrix was confirmed by corroded surface observation in the bonded samples immersed in 5 wt% NaCl solution and Kroll's etchant, respectively. The corrosion damage gradually disappeared from the Mg alloy matrix with an increase of the Al content (Fig. 5.10 and 5.13).

The galvanic corrosion resistance of the Ti/Mg alloy (ST) bonded materials was improved by increasing the Al content in Mg alloy (ST), or by increasing the bonding temperature to enhanced the formation of the Al diffusion layer and the Ti_3Al layer. This formation caused a decrease in SPD and potential gradient which resulted in the improvement of galvanic corrosion resistance. The improvement of galvanic corrosion resistance was supported by the disappearance of $Mg(OH)_2$ layer at the bonding interface. This was achieved by increasing the Al content and bonding temperature (Fig. 5.6 and 5.7). For samples tested in Kroll's etchant, an increase of the Al content affects the surface profile of the sample after corrosion, where a surface slope appeared at the bonding interface of the bonded samples containing a high Al content. On the other hand, the surface level was suddenly changed at the bonding interface in the bonded samples that contained a low Al content such as Ti/AZ31B (ST) and Ti/AZ61 (ST), due to the low galvanic corrosion resistance. The line profiles of the bonded samples after corrosion are also measured to verify the improvement of galvanic corrosion resistance. The galvanic depth and width (G.D. and G.W.) gradually decreased with the Al content in Mg alloy (ST) was increased (Fig. 5.18). The increase in bonding temperature also has an effect on the galvanic corrosion resistance. Namely, the corrosion depth at the bonding interface decreases with an increase of the bonding temperature from 400 to 475 ^{o}C for all bonded materials (Fig. 5.19). The summarized results for the corrosion tests in and Kroll's etchant is listed in Table 5.3. It is concluded that the improvement in the galvanic corrosion resistance and corrosion resistance of Mg alloys (ST) can increase the life span of light weight bonded

materials fabricated by SPS.

Table 5.3 Summary of results from corrosion test of Ti/Mg-Al alloy in Kroll's etchant.

Materials	Bonding temperature (°C)	Ti_3Al layer	SPD (V)	P.G. (V/μm)	G.D. (μm)	G.W. (μm)
Ti/AZ31B (ST)	400	No	0.89	0.82	44.0	633.3
	475	Yes	0.81	0.77	29.8	510.1
Ti/AZ61 (ST)	400	No	0.85	0.81	43.9	545.3
	475	Yes	0.79	0.71	30.7	457.4
Ti/AZ80 (ST)	400	Yes	0.79	0.66	36.4	539.5
	475	Yes	0.75	0.38	26.5	346.1
Ti/AZ91 (ST)	400	Yes	0.75	0.65	29.4	287.3
	475	Yes	0.72	0.46	19.1	281.5

※ SPD = Surface potential difference

P.G. = Potential gradient

G.D. = Galvanic depth

G.W. = Galvanic width

CHAPTER 6: SUMMARY AND FUTURE WORK

In this research, pure Ti was bonded together with Mg alloys with or without solution treatment by solid state bonding. Spark plasma sintering (SPS) was applied to bond these two materials due to, its natural advantage, where the high temperature and pressure can be simultaneously introduced to the sample. SPS also provides a high heating rate, resulting in a short processing time for bonding. The bonding interfaces of Ti/Mg alloy and Ti/Mg alloy (ST) dissimilar materials were observed to investigate the effect of solution treatment for Mg alloys on the bonding strength. The effect of Al content in Mg alloys on the bonding strength and corrosion behavior was also studied. Bonding parameters such as temperature, time and pressure were varied to investigate the effect of each parameter on the bonding strength and corrosion behavior. The characteristics of bonding interface was mainly observed by transmission electron microscope (TEM) in order to clearly understand the formation of Ti_3Al intermetallic layer and the diffusion of Al from Mg alloys to Ti.

6.1 Dissimilar materials between pure Ti and non-solution treated Mg alloys

Non-solution treated Mg alloys show an existence of brittle $Mg_{17}Al_{12}$ particles in the Mg matrix. After SPS, these particles were dissolved into the Mg matrix but some of them still remained. The fine bonding interface was achieved without any crack, void or oxide layer. The perfect contact between pure Ti and Mg alloys was obtained due to the plastic deformation of the Mg alloy. The dislocation piled-up or high dislocation density area at the bonding interface on the Mg alloy side was a good evidence for the plastic deformation of the Mg alloy. The Ti_3Al interaction layer was observed at the bonding interface of Ti/AZ80 and Ti/AZ91 bonded at 400 ^oC for 1 or 2 h. These two bonded materials also showed a higher bonding strength than Ti/AZ31B and Ti/AZ61. This implies that the formation of Ti_3Al layer resulted in an improvement in the bonding strength. The formation of Al diffusion layer was also important since it was observed in Ti/AZ31B and Ti/AZ61, where the Ti_3Al layer was not formed. This is due to the formation of very thin and non-uniform Al diffusion layer, but these bonded materials

still exhibited a satisfied bonding strength. High Al content in Mg alloy will promote the formation of this layer. The effect of Al content on the bonding strength of dissimilar materials was confirmed by an in-situ tensile test, where the high Al content area (a matrix around TR $Mg_{17}Al_{12}$) was elongated after the tensile specimen failed. The highest bonding strength among all the dissimilar materials bonded at 400 ºC for 1 h was obtained for the Ti/AZ80 dissimilar material with a value of 183.2 MPa. This corresponds to the formation of Ti_3Al intermetallic layer and the uniform Al diffusion layer at the bonding interface. Therefore, the Ti_3Al intermetallic and Al diffusion layer is very important to the fabrication of high bonding strength Ti/Mg alloy dissimilar materials. The observation of fracture surfaces showed a large amount of Mg alloy debris attached on the Ti surface, for which a high bonding strength is obtained. The bonding was thought to occur in all areas even on a smooth fracture surface, because very small Mg alloy particles were observed in the corresponding areas on the Ti fracture surface. The experimental results suggested that applying bonding time for 1 h is sufficient to form a uniform Al diffusion layer in all Mg alloys, and a satisfied bonding strength can be obtained.

6.2 Dissimilar materials between pure Ti and solution treated Mg alloys

Solution treated Mg alloys or Mg alloys (ST) showed no brittle $Mg_{17}Al_{12}$ particles in the Mg alloy matrix. Moreover, the Al distribution in Mg alloys was more uniform than that in non-solution treated Mg alloys, especially in AZ31B (ST) and AZ61 (ST). Solution treatment also resulted in an increase of the Al content on Mg matrix due to the dissolving of $Mg_{17}Al_{12}$ particles, as well as the diffusion of Al from high concentration area (grain boundary) to low concentration areas (inside grain). It showed a significant improvement in bonding strength and bonding efficiency between pure Ti and Mg alloys (ST) compared to that between pure Ti and non-solution treated Mg alloys. The uniform diffusion layer of Al was observed in all samples bonded at 400 ºC for 1 h, which resulted in an improvement in the bonding strength. The uniform bonding strength with similar stress-strain curve was obtained from three tensile specimens due to the solution treatment for Mg alloys. From the experimental results, bonding for 0.5 h is not sufficient to obtain a satisfied bonding strength for Ti/Mg alloy (ST)

dissimilar materials. This is due to the thin and non-uniform Al diffusion layer. The bonding strength was not improved when increasing bonding time from 1 to 2 h, which is similar to for all the Ti/Mg alloy dissimilar materials. It is found that the bonding pressure does not affect the bonding strength since a pressure of 10 MPa is already enough to deform the Mg alloys plastically and form a perfect contact between pure Ti and a Mg alloy. However, the bonding strength can be further improved by increasing the bonding temperature that promotes the reaction between Ti and Al elements. The small amount of liquid phase was formed in Ti/AZ80 (ST) and Ti/AZ91 (ST) at a bonding temperature of 420 ºC, which is corresponding to the DTA results. However, the bonding strength improvement was not significant as the characteristics of bonding interfaces are similar for the samples bonded at 400 and 475 ºC, respectively. The bonding strengths of Ti/AZ80 (ST) and Ti/AZ91 (ST) were gradually increased with an increase of the bonding temperature from 400 to 475 ºC, owing to the formation of continuous Ti_3Al layer. The liquid phase formation was found in Ti/AZ31B (ST) and Ti/AZ61 (ST) at 475 ºC. This improved a bonding strength of Ti/AZ31B (ST) and Ti/AZ61 (ST) because of the formation of a thin Ti_3Al layer.

6.3 Corrosion behavior of dissimilar materials

The Ti/Mg alloy (ST) dissimilar materials bonded at 475 ºC showed a superior galvanic corrosion resistance compared to the samples bonded at 400 ºC. The formation of Ti_3Al intermetallic layer at the bonding interface in the samples bonded at 475 ºC plays a major contribution to the improvement. This was confirmed by microstructure observation at the bonding interface after corrosion in 5 wt% NaCl solution, where a $Mg(OH)_2$ layer was observed in all samples bonded at 400 ºC. On the other hand, this corrosion product layer was only observed in Ti/AZ31B (ST) and Ti/AZ61 (ST) of the samples bonded at 475 ºC. For corrosion in Kroll's etchant, the galvanic width (G.W.) and galvanic depth (G.D) decreased with the Al content in Mg alloys due to the formation of a uniform and continuous Ti_3Al intermetallic layer, which inhibited a progress of galvanic corrosion.

The scanning results from SKPFM showed the potential gradient at the bonding interfaces of the samples bonded at 475 ºC. The potential gradient confirmed an existence of the Ti_3Al layer, which prevents the large

and abrupt potential change at the bonding interface, thus resulting in the reduction of galvanic corrosion damage. The Mg alloys contained a high Al content such as AZ80 and AZ91 showed good corrosion resistance because they can form the Mg-Al-O film on their surfaces, which is more effective to prevent corrosion than the conventional $Mg(OH)_2$ film. The increase in an Al content in Mg alloys, on the other hand, makes this film became more stable and decreases the corrosion damage area after corrosion test.

6.4 Recommendation and future work

This research is aimed to study the microstructure evolution at the bonding interface, the bonding strength of Ti/Mg alloy and Ti/Mg alloy (ST) dissimilar materials, and the corrosion behavior of these bonded materials. The improvement in bonding strength is attributed to the formation of a uniform Al diffusion layer and a Ti_3Al intermetallic layer. Additional experiments may be performed to increase the thickness of the Al diffusion and Ti_3Al intermetallic layers. Interesting ways include using an inserted sheet of pure Al, and using different bonding methods such as transient liquid phase (TLP) bonding. The relationship between the thickness of Ti_3Al layer and the bonding strength of dissimilar materials can be investigated. A change of the thickness of the Ti_3Al layer may affect the galvanic corrosion resistance of Ti/Mg alloy dissimilar materials as well. Mechanical evaluation techniques such as shear or fatigues test may also be performed to provide fully understanding of the reliability of the bonded materials for a variety of engineering applications.

The results of this work can be extended to evaluate the solid state bonding of other dissimilar materials systems. There are many places in the industry requiring bonded materials, where the other methods can hardly be used. Spark plasma sintering can provide a high temperature and pressure simultaneously, and is capable of bonding many dissimilar materials.

PUBLICATIONS

1. Patchara Pripanapong, Junko Umeda, Hisashi Imai, Makoto Takahashi, Katsuyoshi Kondoh (2016), "Bonding mechanism of Ti/AZ80 (Mg alloy) dissimilar materials fabricated by spark plasma sintering", Journal of Multidisciplinary Engineering Science Studies, Science and Technology, Volume 2, Issue 10, pp. 1009-1013.
2. Patchara Pripanapong, Junko Umeda, Hisashi Imai, Makoto Takahashi, Katsuyoshi Kondoh (2016), "Tensile strength of Ti/Mg alloys dissimilar bonding material fabricated by spark plasma sintering", International Journal of Engineering Innovation & Research, Timeline publication, Volume 5, Issue 4, pp 253-259.
3. Patchara Pripanapong, Shota Kariya, Tachai Luangvaranunt, Junko Umeda, Seiichiro Tsutsumi, Makoto Takahashi, Katsuyoshi Kondoh (2016), "Corrosion behavior and strength of dissimilar bonding material between Ti and Mg alloys fabricated by spark plasma sintering", Materials, Multidisciplinary Digital Publishing Institute, Volume 9, Issue 8, Article number 665, DOI:10.3390/ma9080665.

ACKNOWLEDGEMENTS

I would like to express my deepest gratitude and thanks for my supervisor, Professor Katsuyoshi Kondoh for his endless support throughout my Ph.D. program. His valuable guidance will always be remembered. I would like to thank my supervisory committee members, Professor Kohji Minoshima, Professor Kazuhiro Ito and Associate professor Yousuke Kawahito for their valuable suggestion to my dissertation. I would like to thank to Assistant professor Junko Umeda and Mrs Hiroko Takeda for supporting in document paper. I would also like to thank my former advisor in Thailand, Associate professor Tachai Luangvaranunt for his support and encouragement during study.

I would like to thank Dr. Makoto Takahashi and Mr. Shota Kariya, Joining and Welding Research Institute, Osaka University for their assistance in the TEM and SKPFM, respectively. I would also like to thank Dr. Jianghua Shen and Dr. Biao Chen for their support before my dissertation defense. Special thanks to Mr. Yoshinori Muraki and Mr Kyugo Inui for their assistance in the helping with the equipment in the institute and set up for mechanical test.

References

[1] R.R. Boyer, An overview on the use of titanium in the aerospace industry, Mater. Sci. Eng. A. 213 (1996) 103-114.
[2] E. Schubert, M. Klassen, I. Zerner, C. Wals, G. Sepold, Light-weight structures produced by laser beam joining for future applications in automobile and aerospace industry, J. Mater. Process. Tech. 115 (2001) 2-8.
[3] Y. Wang, H. Yu, C. Chen, Z. Zhao, Review of the biocompatibility of micro-arc oxidation coated titanium alloys, Mater. Design. 85 (2015) 640-652.
[4] P. Naddeo, L. Laino, M.L. Noce, A. Piattelli, A.D. Rosa, G. Iezzi, G. Laino, F. Paino, G. Papaccio, V. Tirino, Surface biocompatibility of differently textured titanium implants with mesenchymal stem cells, Dent. Mater. 31 (2015) 235-243.
[5] C.M. Tilmaciu, M. Mathieu, J.P. Lavigne, K. Toupet, G. Guerrero, A. Ponche, J. Amalric, D. Noel, P.H. Mutin, In vitro and in vivo characterization of antibacterial activity and biocompatibility: A study on silver-containing phosphonate monolayers on titanium, Acta. Biomater. 15 (2015) 266-277.
[6] J. Du, W. Han, Y. Peng, Life cycle greenhouse gases, energy and cost assessment of automobiles using magnesium from Chinese Pidgeon process, J. Clean. Prod. 18 (2010) 112-119.
[7] S.F. Hassan, O.O. Nasirudeen, N.A. Aqeeli, N. Saheb, F. Patel, M.M.A. Baig, Magnesiume-nickel composite: Preparation, microstructure and mechanical properties, J. Alloy. Compd. 646 (2015) 333-338.
[8] Q. Zhao, W. Mahmood, Y. Zhu, Synthesis of dittmarite/$Mg(OH)_2$ composite coating on AZ31 using hydrothermal treatment, Appl. Surf. Sci. 367 (2016) 249-258.
[9] H.C. Chen, A.J. Pinkerton, L. Li, Fibre laser welding of dissimilar alloys of Ti-6Al-4V and Inconel 718 for aerospace applications, Int. J. Adv. Manuf. Technol. 52 (2011) 977-987.
[10] W. Yao, A. Wu, G. Zou, J. Ren, Formation process of the bonding joint in Ti/Al diffusion bonding, Mater. Sci. Eng. A. 480 (2008) 456-463.
[11] A. Miriyev, A. Levy, S. Kalabukhov, N. Frage, Interface evolution and shear strength of Al/Ti bi-metals processed by a spark plasma sintering (SPS) apparatus, J. Alloy. Compd. 678 (2016) 329-336.

[12] H. Chen, J. Liu, W. Huang, Corrosion behavior of silicon nitride bonding silicon carbide in molten magnesium and AZ91 magnesium alloy, Mater. Sci. Eng. A. 415 (2006) 291-296.
[13] S.K. Shaha, F. Czerwinski, W. Kasprzak, J. Friedman, D.L. Chen, Ageing characteristics and high-temperature tensile properties of Al-Si-Cu-Mg alloys with micro-additions of Cr, Ti, V and Zr, Mater. Sci. Eng. A. 652 (2016) 353-364.
[14] P. D. Motevalli, B. Eghbali, Microstructure and mechanical properties of Tri-metal Al/Ti/Mg laminated composite processed by accumulative roll bonding, Mater. Sci. Eng. A. 628 (2015) 135-142.
[15] C. Machio, D. Nyabadza, V. Sibanda, H.K. Chikwanda, Characterization of mechanically alloyed f.c.c. Ti-Mg-based powders, Powder. Technol. 207 (2011) 387-395.
[16] J.L. Murray, Bulletin of Alloy Phase Diagrams, 7 (1986) 245.
[17] K.S. Weil, Y. Hovanski, C.A. Lavender, Effects of $TiCl_4$ purity on the sinterability of Armstrong-processed Ti powder, J. Alloy. Compd. 473 (2009) 39-43.
[18] V. Venkateswarlu, D. Tripathy, K. Rajagopal, K.T. Tharian, P.V. Venkitakrishnan, Failure analysis and optimization of thermo-mechanical process parameters of titanium alloy (Ti-6Al-4V) fasteners for aerospace applications, J. Csefa. 1 (2013) 49-60.
[19] C.Q. Zhang, J.D. Robson, P.B. Prangnell, Dissimilar ultrasonic spot welding of aerospace aluminum alloy AA2139 to titanium alloy TiAl6V4, J. Mater. Process. Tech. 231 (2016) 382-388.
[20] O.E. Nelson, The Product Life Cycle of Titanium, paper presented at the Annual Conference of the Titanium Development Association, Tucson, AZ, 13 Oct 1989.
[21] H. Schwab, F. Palm, U. Kuhn, J. Eckert, Microstructure and mechanical properties of the near-beta titanium alloy Ti-5553 processed by selective laser melting, Mater. Design. In Press, Accepted Manuscript, 2016.
[22] H.B. Bomberger, F.H. Froes, P.H. Morton, Titanium-A Historical Perspective, in Titanium technology: Present status and Future Trends, F.H. Froes, D. Eylon, H.B. Bomberger, Ed., Titanium Development Association, 1985, pp. 3-17.
[23] M.J. Donachie, Titanium: A Technical Guide, ASM INTERNATIONAL,

1988.
[24] Y.Z. Liu, X.T. Zu, C. Li, X.Y. Qiu, W.J. Li, X.Q. Huang, Hydrogen embrittlement of a Ti-Al-Zr alloy evaluated by impact test method, Scripta. Mater. 52 (2005) 821-825.
[25] S. Xu, X. Xu, Y. Xu, Y. Liang, J. Lin, Phase transformations and phase equilibria of a Ti-46.5Al-16.5Nb alloy, Mater. Design. 101 (2016) 88-94.
[26] J. Yang, J. Peng, E.A. Nyberg, F. Pan, Effect of Ca addition on the corrosion behavior of Mg-Al-Mn alloy, Appl. Surf. Sci. 369 (2016) 92-100.
[27] M. Rejaeien, M. Karamouz, M. Emamy, M. Hajizamani, Effects of Be additions on microstructure, hardness and tensile properties of A380 aluminum alloy, T. Nonferr. Metal. Soc. 25 (2015) 3539-3545.
[28] R.S. Busk, Magnesium Products Design, Vol. 1, Marcel Dekker, 1987, p 180.
[29] S. Housh, B. Mikucki, Selection and Application of Magnesium and Magnesium Alloys, ASM INTERNATIONAL, 1992.
[30] V. Anes, R.S. Pedro, E. Henriques, M. Freitas, L. Reis, Galvanic corrosion of aircraft bonded joints as a result of adhesive microcracks, J. Prostr. 1 (2016) 218-225.
[31] H. Du, J. Liu, A. Guo, High-temperature bonding performance of modified heat-resistant adhesive for ceramic connection, J. Alloy. Compd. 663 (2016) 82-85.
[32] D. Brandon, W.D. Kaplan, Joining Processes: An Introduction, John Wiley and Sons, Chichester, England, 1997.
[33] R. Cao, T. Wang, C. Wang, Z. Feng, Q. Lin, J.H. Chen, Cold metal transfer welding-brazing of pure titanium TA2 to magnesium alloy AZ31B, J. Alloy. Compd. 605 (2014) 12-20.
[34] S. Chen, L. Li, Y. Chen, J. Huang, Joining mechanism of Ti/Al dissimilar alloys during laser welding-brazing process, J. Alloy. Compd. 509 (2011) 891-898.
[35] M. Esmaily, S.N. Mortasavi, P. Todehfalah, M. Rashidi, Joining mechanism of Ti/Al dissimilar alloys during laser welding-brazing process, Mater. Design. 47 (2013) 143-150.
[36] S. Takhti, M. Reihanian, A. Ashrafi, Microstructure characterization and mechanical properties of gas tungsten arc welded cast A356 alloy, T. Nonferr. Metal. Soc. 25 (2015) 2137-2146.
[37] G. Casalino, M. Mortello, P. Peyre, Yb-YAG laser offset welding of

AA5754 and T40 butt joint, J. Mater. Process. Tech. 223 (2015) 139-149.
[38] O. Dezellus, J. Andrieux, F. Bosselet, M. Sacerdote-Peronnet, T. Baffie, F. Hodaj, N. Eustathopoulos, J.C. Viala, Transient liquid phase bonding of titanium to aluminium nitride, Mater. Sci. Eng. A. 495 (2008) 254-258.
[39] G. Cam, U. Ozdemir, V. Ventzke, M. Kocak, Microstructural and mechanical characterization of diffusion bonded hybrid joints, J. Mater. Sci. 43 (2008) 3491–3499.
[40] W. Gale, Applying TLP bonding to the joining of structural intermetallic compounds, J. Miner. Met. Mater. Soc. 51 (1999) 49-52.
[41] A. AlHazaa, T.I. Khan, I. Haq, Transient liquid phase (TLP) bonding of Al7075 to Ti-6Al-4V alloy, Mater. Charact. 61 (2010) 312-317.
[42] A. AlHazaa, T.I. Khan, Diffusion bonding of Al7075 to Ti-6Al-4V using Cu coatings and Sn-3.6Ag-1Cu interlayers, J. Alloys Compd. 494 (2010) 351-358.
[43] A. AlHazaa, Diffusion bonding of Al7075 alloy to Ti-6Al-4V alloy, University of Calgary, 2009.
[44] M.S. Kenevisi, S.M. Mousavi, An investigation on microstructure and mechanical properties of Al7075 to Ti-6Al-4V Transient Liquid Phase (TLP) bonded joint, Mater. Design. 38 (2012) 19–25.
[45] Z. Jamili-Shirvan, M. Haddad-Subzevar, J. Vadati-Khaki, N. Chen, Q. Shi, K.F. Yao, Microstructure characterization and mechanical properties of Ti-based bulk metallic glass joints prepared with friction stir spot welding process, Mater. Design. 100 (2016) 120-131.
[46] R.S. Mishra, Z.Y. Ma, Friction stir welding and processing, Mater. Sci. Eng. R. 50 (2005) 1-78.
[47] B. Li, Y. Chen, L. Liu, W. Hu, Effects of processing variables and heat treatments on Al/Ti-6Al-4V interface microstructure of bimetal clad-plate fabricated via a novel route employing friction stir lap welding, J. Alloy. Compd. 658 (2016) 904-903.
[48] A. Dorbane, B. Mansoor, G. Ayoub, V.C. Shunmugasamy, A. Imad, Mechanical, microstructural and fracture properties of dissimilar welds produced by friction stir welding of AZ31B and Al6061, Mater. Sci. Eng. A. 651 (2016) 720-733.
[49] C. Zhang, H. Li, M. Li, Detailed evolution mechanism of interfacial void morphology in diffusion bonding, J. Mater. Sci. Technol. 32 (2016) 259-264.
[50] X. Shao, X. Guo, Y. Han, W. Lu, J. Qin, D. Zhang, Characterization of

the diffusion bonding behavior of pure Ti and Ni with different surface roughness during hot pressing, Mater. Design. 65 (2015) 1001-1010.
[51] X. Liu, H. Nishikawa, Low-pressure Cu-Cu bonding using in-situ surface-modified microscale Cu particles for power device packaging, Scripta. Mater. 120 (2016) 80-84.
[52] C. Nouveau, C. Labidi, R. Collet, Y. Benlatreche, M.A. Djouadi, Effect of surface finishing such as sand-blasting and CrAlN hard coatings on the cutting edge's peeling tools' wear resistance, Wear. 267 (2009) 1062-1067.
[53] J. Wang, T. Wang, G. Pan, X. Lu, Effects of catalyst concentration and ultraviolet intensity on chemical mechanical polishing of GaN, Appl. Surf. Sci. 378 (2016) 130-135.
[54] M. Sowa, K. Gren, A.I. Kukharenko, D.M. Korotin, J. Michalska, L. Szyk-Warszynska, M. Mosialek, J. Zak, E. Pamula, E.Z. Kurmaev, S.O. Cholakh, W. Simka, Influence of electropolishing and anodic oxidation on morphology, chemical composition and corrosion resistance of niobium, Mater. Sci. Eng. C. 42 (2014) 529-537.
[55] Z. Du, S. Jiang, K. Zhang, Z. Lu, B. Li, D. Zhang, The structural design and superplastic forming/diffusion bonding of Ti2AlNb based alloy for four-layer structure, Mater. Design. In Press, Corrected Proof, 2016.
[56] R.A. Antunes, M. Oliveira, Materials selection for hot stamped automotive body parts: An application of the Ashby approach based on the strain hardening exponent and stacking fault energy of materials, Mater. Design. 63 (2014) 247-256.
[57] C. Zhang, H. Li, M.Q. Li, Detailed analysis of surface asperity deformation mechanism in diffusion bonding of steel hollow structural components, Appl. Surf. Sci. 371 (2016) 407-414.
[58] C.Y. Sun, L. Li, M.W. Fu, Q.J. Zhou, Element diffusion model of bimetallic hot deformation in metallurgical bonding process, Mater. Design. 94 (2016) 433-443.
[59] P. Perriat, B. Gillot, A model for coupled diffusion reactions in Mn-Zn ferrites: Generalization of the Ficks's first law, Solid. State. Ionics. 67 (1993) 35-43.
[60] S.R. Hosseini, Simulation of case depth of cementation steel according to Ficks's law, J. Iron. Steel. Res. Int. 19 (2012) 71-78.
[61] P. Shewmon, Diffusion in solid, 2nd Ed., TMS, Warrendale, Pennsylvania, 1989.

[62] H.S. Lee, J.H. Yoon, C.H. Park, Y.G. Ko, D.H. Shin, C.S. Lee, A study on diffusion bonding of superplastic Ti-6Al-4V ELI grade, J. Mater. Process. Tech. 187-188 (2007) 526-529.
[63] A. Elrefaey, W. Tillmann, Solid state diffusion bonding of titanium to steel using a copper base alloy as interlayer, J. Mater. Process. Tech. 209 (2009) 2746-2752.
[64] T. Vigraman, D. Ravindran, R. Narayanasamy, Effect of phase transformation and intermetallic compounds on the microstructure and tensile strength properties of diffusion-bonded joints between Ti-6Al-4V and AISI 304L, Mater. Design. 36 (2012) 714-727.
[65] R. Baboian, W.D. France, L.C. Rowe, J.F. Rynewicz, Galvanic and Pitting Corrosion--Field and Laboratory Studies, STP 576, American Society for Testing and Materials, 1974.
[66] C.P. Larrabee, Corrosion resistance of high strength low-alloy steels as influenced by composition and environment, Corrosion. 9 (1953) 259-271.
[67] Standard Guide for Development and Use of a Galvanic Series for Predicting Galvanic Corrosion Performance, G 82, Annual Book of ASTM Standards, American Society for Testing and Materials.
[68] Z. Shi, J.X. Jia, A. Atrens, Galvanostatic anodic polarisation curves and galvanic corrosion of high purity Mg in 3.5% NaCl saturated with $Mg(OH)_2$, Corros. Sci. 60 (2012) 296-308.
[69] H.P. Godard, Galvanic corrosion behavior of aluminum in the atmosphere, Mater. Prot. 2 (1963) 38.
[70] K.G. Compton, A. Mendizza, W.W. Bradley, Atmospheric galvanic couple corrosion, Corrosion. 2 (1995) 383.
[71] S. Candan, M. Celik, E. Candan, Effectiveness of Ti-micro alloying in relation to cooling rate on corrosion of AZ91 Mg alloy, J. Alloy. Compd. 672 (2016) 197-193.
[72] J.D. Hanawalt, C.E. Nelson, J.A. Peloubet, Trans. AIME. 147 (1942) 273.
[73] M.R. Bothwell, The Corrosion of Light Metals, John Wiley & Sons, 1967, p 269.
[74] F.L. Laque, Corrosion Testing, in Proceedings of the American Society for Testing and Materials, 51 (1951) 557.
[75] M. Samavatian, A. Halvaee, A.A. Amadeh, A. Khodabandeh, Transient liquid phase bonding of Al 2024 to Ti-6Al-4V alloy using Cu-Zn interlayer, T.

Nonferr. Metal. Soc. 25 (2015) 770-775.
[76] E. Norouzi, M. Atapour, M. Shamanian, A. Allafchian, Effect of bonding temperature on the microstructure and mechanical properties of Ti-6Al-4V to AISI 304 transient liquid phase bonded joint, Mater. Design. 99 (2016) 543-551.
[77] A.M. Atieh, T.I. Khan, Investigating the process parameters on the joint formation of semi-solid TLP bonding of Ti-6Al-4V to Mg-AZ31, J. Mater. Sci. 48 (2013) 6737-6745.
[78] F. Bu, Q. Yang, X. Qiu, T. Zheng, D. Zhang, X. Niu, Y. Li, X. Liu, J. Meng, Study on the assemblage of Y and Gd on microstructure and mechanical properties of hot extruded Mg-Al-Zn alloy, Mater. Sci. Eng. A. 639 (2015) 198-207.
[79] N. Birks, G.H. Meier, High Temperature Oxidation of Metals, Edward Arnold, London, 1983.
[80] V.Y. Mehr, M.R. Toroghinejad, A. Rezaeian, The effects of oxide film and annealing treatment on the bond strength of Al-Cu strips in cold roll bonding process, Mater Design. 53 (2014) 174-181.
[81] A. Miriyev, A. Stern, E. Tuval, S. Kalabukhov, Z. Hooper, N. Frage, Titanium to steel joining by spark plasma sintering (SPS) technology, J. Mater. Process. Tech. 213 (2013) 161-166.
[82] P.J. Goodhew, J. Humphreys, R. Beanland, Electron Microscopy and Analysis, Taylor & Francis, London, 2001.
[83] G. Wu, S. Zaefferer, Advances in TEM orientation microscopy by combination of dark-field conical, scanning and improved image matching, Ultramicroscopy. 109 (2009) 1317-1325.
[84] Y. Lou, L. Li, J. Zhou, L. Na, Deformation behavior of Mg-8Al magnesium alloy compressed at medium and high temperatures, Mater. Charact. 62 (2011) 346-353.
[85] C. Tan, X. Song, B. Chen, L. Li, J. Feng, Enhanced interfacial reaction and mechanical properties of laser welded-brazed Mg/Ti joints with Al element fromfiller, Mater. Lett. 167 (2016) 38-42.
[86] H.R. Akramifard, H. Mirzadeh, M.H. Parzsa, Estimating interface bonding strength in clad sheets based on tensile test results, Mater. Design. 64 (2014) 307-309.
[87] H. Yu, C. Lu, A.K. Tieu, H. Li. A. Godbole, C. Kong, Annealing effect on microstructure and mechanical properties of Al/Ti/Al laminate sheets, Mater.

Sci. Eng. A. 660 (2016) 195-204.
[88] Z. Huang, J. Yanagimoto, Dissimilar joining of aluminum alloy and stainless steel thin sheets by thermally assisted plastic deformation, J. Mater. Process. Tech. 225 (2015) 393-404.
[89] J. Cao, J. Liu, X. Song, X. Lin, J. Feng, Diffusion bonding of TiAl intermetallic and Ti_3AlC_2 ceramic: Interfacial microstructure and joining properties, Mater. Design. 56 (2014) 115-121.
[90] P. Fei, Z. Qu, R. Wu, Microstructure and hardness of Mg-9Li-6Al-xLa (x = 0, 2, 5) alloys during solid solution treatment, Mater. Sci. Eng. A. 625 (2015) 169-176.
[91] A. Stevenson, Heat Treating of Mg Alloys, ASM handbook, Vol. 4, 1991.
[92] R. Abedi, A. Akbarzadeh, Bond strength and mechanical properties of three-layered St/AZ31/St composite fabricated by roll bonding, Mater. Design. 88 (2015) 880-888.
[93] A. Miriyev, D. Barlam, R. Shneck, A. Stern, N. Frage, Steel to titanium solid state joining displaying superior mechanical properties, J. Mater. Process. Tech. 214 (2014) 2884-2890.
[94] F. Guo, D. Zhang, X. Fan, J. Li, L. Jiang, F. Pan, Microstructure, texture and mechanical properties evolution of pre-twinning Mg alloys sheets during large strain hot rolling, Mater. Sci. Eng. A. 655 (2016) 92-99.
[95] J.D. Verhoven, Fundamentals of Physical Metallurgy, John Wiley & Sons, Canada, 1975.
[96] C.A. Huang, T.H. Wang, W.C. Han, C.H. Lee, A study of the galvanic corrosion behavior of Inconel 718 after electron beam welding, Mater. Chem. Phys. 104 (2007) 293-300.
[97] Y. Wang, H. Liu, C. Zeng, Galvanic corrosion of pure metals in molten fluorides, J. Fluorine. Chem. 165 (2014) 1-6.
[98] S. Candan, M. Celik, E. Candan, Effectiveness of Ti-micro alloying in relation to cooling rate on corrosion of AZ91 Mg alloy, J. Alloy. Compd. 672 (2016) 197-203.
[99] E.F. Emley, Principles of Magnesium Technology, Pergamon Press, 1966, p 685.
[100] K. Funutsu, H. Fukuda, R. Takai, J. Umeda, K. Kondoh, Quantitative evaluation of initial galvanic corrosion behavior of CNTs reinforced Mg-Al alloy, Adv. Powder. Technol. 24 (2013) 833-837.
[101] H.P. Hack, Galvanic corrosion, Reference Module in Materials Science

and Materials Engineering, 2016.
[102] Q. Jiang, X. Ma, K. Zhang, Y. Li, X. Li, Y. Li, M. Ma, B. Hou, Anisotropy of the crystallographic orientation and corrosion performance of high-strength AZ80 Mg alloy, Journal of Magnesium and Alloys. 3 (2015) 309-314.
[103] B.M. Wilke, L. Zhang, W. Li. C. Ning, C. Chen, Y. Gu, Corrosion performance of MAO coatings on AZ31 Mg alloy in simulated body fluid vs. Earle's Balance Salt Solution, Appl. Surf. Sci. 363 (2016) 328-337.
[104] F.N. Afshar, A.M. Glenn, J.H.W. de Wit, H. Terryn, J.M.C. Mol, A combined electron probe micro analysis and scanning Kelvin probe force microscopy study of a modified AA4xxx/AA3xxx aluminium brazing sheet, Electrochim. Acta. 104 (2013) 48-63.
[105] Y. Liu, D. Bian, Y. Wu, N. Li, K. Qiu, Y. Zheng, Y. Han, Influence of biocompatible metal ions (Ag, Fe, Y) on the surface chemistry, corrosion behavior and cytocompatibility of Mg-1Ca alloy treated with MEVVA, Colloid. Surface. B. 133 (2015) 99-107.
[106] G.S. Cole, Magnesium (Mg) corrosion protection techniques in the automotive industry, Corrosion prevention of Mg alloys, Woodhead publishing, 2013, pp 489-508.
[107] D.A. Shifler, Understanding material interactions in marine environments to promote extended structural life, Corros. Sci. 47 (2005) 2335-2352.
[108] C.W. Chan, H.C. Man, C.M. Yue, Effect of post-weld heat-treatment on the oxide film and corrosion behavior of laser-welded shape memory NiTi wires, Corros. Sci. 56 (2012) 158-167.
[109] W. Liu, L. Long, Y. Ma, L. Wu, Microstructure evolution and mechanical properties of Mg/Al diffusion bonded joints, J. Alloy. Compd. 643 (2015) 34-39.
[110] M. Jafarian, M. Rizi, M. Jafarian, M. Honarmand, H. Javadinejad, A. Ghaheri, M. Bharamipour, M. Ebrahimian, Effect of thermal tempering on microstructure and mechanical properties of Mg-AZ31/Al-6061 diffusion bonding, Mater. Sci. Eng. A. 666 (2016) 372-379.
[111] B. Zhou, S. Shang, Y. Wang, Z. Liu, Diffusion coefficients of alloying elements in dilute Mg alloys: A comprehensive first-principles studies, Acta. Mater. 103 (2016) 573-586.
[112] K.M. Kerimov, S.F. Dunaev, E.M. Sljusarenko, Investigation of the

structure of ternary phases in Al-Mg-Ti, Al-Mg-V and Al-Mg-Cr systems, J. Less-common. Met. 133 (1987) 297-302.